ONSET, PROPAGATION, AND EVOLUTION OF STRAIN LOCALIZATION IN UNDRAINED PLANE STRAIN EXPERIMENTS ON CLAY

by

XINGDONG WU

B.S., Kansas State University, 2014

A THESIS

submitted in partial fulfillment of the requirements for the degree

MASTER OF SCIENCE

Department of Civil Engineering
College of Engineering

KANSAS STATE UNIVERSITY
Manhattan, Kansas

2016

Approved by:

Major Professor
Dunja Perić

Copyright

Abstract

The conventional triaxial test is the primary laboratory test for determining the shear strength of soils. Geotechnical field conditions such as long earth dams, long embankments, long retaining walls, strip foundations, tunnels, and buried pipelines often experience plane strain states of stress. However, stress strain and load deformation responses in plane strain loading differ considerably from responses observed in the conventional triaxial test. Research has shown that soils loaded in a plane strain state are far more sensitive to imperfections than soils tested in a conventional triaxial device. Plane strain loading leads to material instability manifested as sudden localized failure, resulting in decreased load-carrying capacity of the soil and compromised geotechnical and civil infrastructures.

Although previous studies have mostly focused on granular materials, this research investigated the plane strain response of clay. An undrained plane strain compression test program was devised to investigate the effects of past stress history and strain rates on strain localization in kaolin clay. Experiments were carried out in a plane strain (or biaxial) device at Northwestern University, Evanston, Illinois. Because the device was heavily internally instrumented, strain localization progress was closely monitored throughout each biaxial test.

Clay response in the biaxial test demonstrated three phases: (1) a homogenous response, (2) the onset and propagation of strain localization, and (3) the evolution of strain localization as a shear band. The duration of each phase was determined for each test, and a Lagrange strain tensor was used to obtain the evolution of volumetric and shear strains at the level of a shear band for three tests. Results revealed the development of large strains in these mesoscale structures. Furthermore, evolution of Mohr-Coulomb effective shear strength parameters was traced throughout the propagation and evolution phases by using two different methods. It showed that in clay samples, unlike in granular materials, the post-peak plateau, which is reached by deviatoric stress, corresponds to friction values that are significantly lower than the critical state values. Other researchers who used scanning electron microscope and anisotropy of magnetic susceptibility detected a significant reorientation of clay particles inside shear bands. Their findings combined with findings in this study lead to the conclusion that the sub-meso scale mechanism responsible for large shear strains and a severe reduction in effective friction is a significant reorientation of clay particles inside shear band.

Table of Contents

List of Figures

List of Tables

Acknowledgements

I would like to extend my most sincere gratitude to the following people, without whose generous help, consistent support, and kind input this study would not be possible.

Firstly, this thesis could not have been possible without the support from **National Science Foundation** (grant # 9806052), which is gratefully acknowledged. Additionally, the support for this project provided by **Professor Richard Finno** from Northwestern University, Evanston, Illinois, is gratefully appreciated.

My gratitude goes to my most helpful advisor, **Professor Dunja Perić**, for her everlasting patience, remarkable inspiration, and insightful guidance, which led me through my academic challenges, explorations, and thesis writing. I feel more than lucky to have a mentor and role model like her whose knowledge and instructions will keep me motivated throughout my academic life and future career.

Besides my advisor **Dr. Perić**, I would like to thank all members of the College of Engineering, including staff, professors, and all those who lent me a hand with this research at Kansas State University. I am grateful for the kindness, encouragement, and support they shared with me four years of my study, which gave me many valuable and pleasant memories worth treasuring for life as well as a more positive, mature, and brave perspective from which to see the world.

My thanks also go to the **Robert I-Jen and Sophia Shui-kan Jung Graduate Scholarship** for their generous financial support, without which this research would be like a train without a track. I can only return their precious help by confidently presenting this research made with my utmost efforts as well as my ongoing endeavors and commitments in the days to come.

I would like to especially thank a friend, **Mr. Mohammed T. Albahttiti**. Without his sincere and constructive help, this pile of words would hardly count as a proper study.

With this opportunity, I would like to express my profound love and gratitude to my wife (**Qiuying Li**), to whom I often forget to say thanks. Her care and company made me a man with responsibilities and purpose.

Last but not least, I want to thank my parents (**Huazhen Wu & Aimei Li**) and parents-in-law (**Linshun Li & Feng Cai**) for their unfailing love and tolerance and the sacrifices they made throughout my life that have kept my heart warm, my life complete, and my path illuminated.

Chapter 1 - Introduction

1.1 Background

Axisymmetric conventional triaxial compression (CTC) experiments are widely used to determine stress-strain response and the shear strength of soil. Geotechnical field conditions such as long earth dams, long embankments, long retaining walls, strip foundations, tunnels, and buried pipelines experience plane strain state of stress. The research demonstrated that soil subjected to plane strain loading is more sensitive to imperfections than soil tested in a CTC experiment. Plane strain loading leads to material instability manifested as sudden localized failure, resulting in decreased load-bearing capacity of the soil and compromised geotechnical and civil infrastructures.

Strain localization is a ubiquitous phenomenon that occurs in well-defined zones in geomaterials (e.g., rocks, sand, and overconsolidated clay), necessitating a knowledge advancement accurate within the field of geotechnical engineering. Research has shown that local strain in shear bands is typically a higher order of magnitude than strain in surrounding materials. The plane strain test has become the most common method to investigate strain localization in sand, (e.g., Lee [1], Mühlhaus and Vardoulakis [2], Peters et al. [3], Drescher et al. [4], Han and Vardoulakis [5], Han and Drescher [6], Finno et al. [7], Saada et al. [8], Alshibli et al. [9], Rechenmacher [10] and Zhang et al. [11], but only limited investigations of strain localization have been carried out in clay soils using a biaxial test such as within the work of Finno and Rhee [12], Perić et al. [13], Alshibli and Akbas [14], Viggiani et al. [15], and Sengupta [16]. This research investigated the plane strain response of clay using an undrained plane strain compression test program to study the effects of stress history and strain rates on strain localization in Georgia kaolin clay. Experiments were carried out in a plane strain (or biaxial) device at Northwestern

University, Evanston, Illinois. Because the device was heavily internally instrumented, strain localization progress was closely monitored throughout each biaxial test.

1.2 Objectives

The primary objective of this research was to investigate the development of strain localization in overconsolidated clays using a modified plane strain apparatus. Plane strain response was chosen in this investigation because soil subjected to plane strain loading is highly susceptible to localized deformation modes, which are typical for progressive failure. In addition, a vast majority of geotechnical engineering prototypes exhibit plane strain state.

The primary research goal was to identify stages of stress-strain response, including a homogeneous reaction that is followed by the onset of strain localization in clay, indicating shear band propagation and evolution. This study also evaluated Mohr-Coulomb shear strength parameters throughout the biaxial experiments and investigated the effects of stress history and strain rates on the undrained plane strain behavior of kaolin clay.

1.3 Scope

Chapter 1 - presents background information about strain localization in soils and its role in geotechnical engineering practice, as well as the study objective and the scope of each chapter.

Chapter 2 - contains a brief literature review that emphasizes strain localization in laboratory shear strength testing of clays.

Chapter 3 - describes material properties of Georgia kaolin, the biaxial apparatus at Northwestern University, experimental procedures, and the biaxial test program.

Chapter 4 - presents results of the biaxial strain experiments, including discussion of the onset and development of strain localization and the identification of three phases, and eight accompanying events.

Chapter 5 - concludes the study and recommends future research.

Chapter 2 - Laboratory Shear Strength of Clay

Although soil mechanics occasionally still uses the term failure surface, the term shear or deformation band has become more prevalent. A deformation band denotes a narrow zone in which large strains become increasingly concentrated with continued loading while little or no strain occurs outside. The process of deformation band formation, propagation, and evolution is referred to as strain localization. This chapter discusses previous research related to laboratory shear strength testing of clays with an emphasis on strain localization. Laboratory tests for determining the shear strength of clays include direct shear (DS), conventional triaxial (CT), true triaxial (TT), hollow cylinder (HC), and biaxial or plane strain (PS) tests.

2.1 Direct Shear Test

Although the DS test is a simple laboratory test for determining shear strength, it lacks drainage control and is unable to measure pore water pressure (PWP). The DS test also exhibits non-uniform shear stress and strain distribution and a predefined orientation of the failure surface due to the construction of the apparatus. Consequently, a shear band always forms in DS tests.

Morgenstern and Tchalenko [17] used a rectangular shear box to study microstructure development in kaolin clay during shear. They used a polarizing microscope to observe deformation progress. Specimens were prepared from consolidated kaolin clay slurry in a 9 in. diameter oedometer. Two experimental sets, each consisting of seven specimens, were tested, and each specimen was trimmed to dimensions of 6 cm × 6 cm × 2.5 cm. The first set produced specimens that were parallel to the bedding, and the second set produced specimens that were perpendicular to the bedding. Each set was placed in the DS apparatus and sheared at a rate of 0.02921 mm/min, thereby creating a drained condition. The DS test was interrupted intermittently,

and thin sections were prepared after impregnation with Carbowax. The researchers used a polarizing microscope to observe a shear-induced fabric in the thin sections.

Both sets of specimens formed kink-bands between the lower and upper shear boxes. Thickness of kink-bands in specimens trimmed parallel to the bedding (a normal kink-band) was thinner than the thickness in specimens trimmed perpendicular to the bedding (a reverse kink-band). The sequence of observed microscopic shear structures showed that simple shear conditions prevailed at peak strength, while a continuous horizontal structure appeared only during the residual stage. Morgenstern and Tchalenko also found that residual strength was obtained as the shear boxes neared the end of travel. They determined that no significant difference occurred in the drained shear strength among shear box samples trimmed at various angles [17].

2.2 Conventional Triaxial Test

Unlike a DS apparatus, a CT device provides drainage control and PWP measurements, and apparatus construction does not predetermine failure plane orientation. However, specimens tested in a CT device are subjected to a cylindrical stress state.

Gylland et al. [18] used a modified CT device (Figure 2.1) to investigate the evolution of shear zones in sensitive Norwegian clay. The modification allowed the apparatus base to slide horizontally during the test in order to facilitate development of strain localization. High-quality 250 mm block clay specimens were collected from depths ranging from 8.5 m to 12.8 m at a site south of Trondheim, Norway. Four sets were tested, with each set containing four specimens. The specimens were trimmed to cylinders with diameters of 54 mm and heights of 100 mm. CT tests were conducted at four displacement rates ranging from 0.05 mm/min to 5 mm/min.

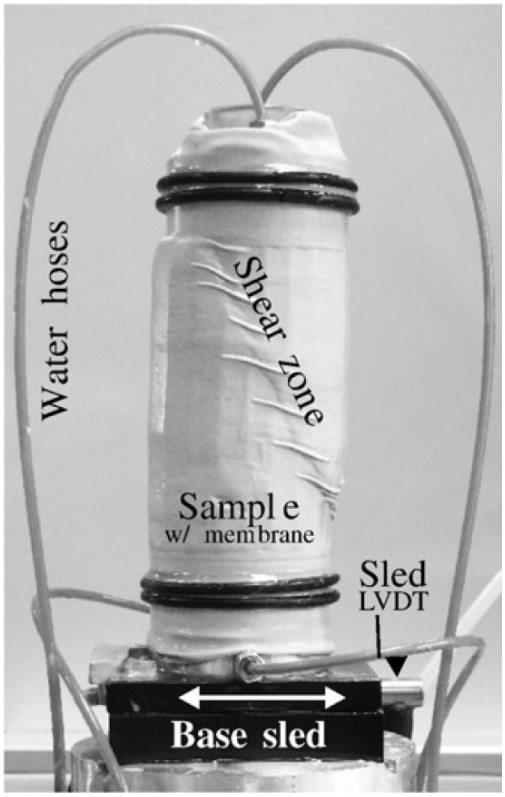

Figure 2.1 Modified conventional triaxial apparatus [18]

Figure 2.2 shows a clay specimen schematic with a visible shear band at the end of the CT test. Light microscopy, a scanning electron microscope (SEM), and a high-resolution X-ray tomography (micro-CT) were used to investigate the shear band structure. Gylland et al. found that the shear zone formed in millimeter-thick, continuous fields of displacement and sets of micron-sized minor shears developed within the main shear zone. These shears initiated, terminated, and merged in the plane and out of the plane directions. A distinct particle reorientation was observed within a minor shear in which flaky clay particles were parallel to the direction of the shear band (Figure 2.2 and Figure 2.3) [18]. In another study Gylland et al. found that strain localization began just before peak deviatoric stress and shear bands developed gradually from the onset of strain localization to fully developed forms (Figure 2.2), whereby shear band thickness gradually decreased [19].

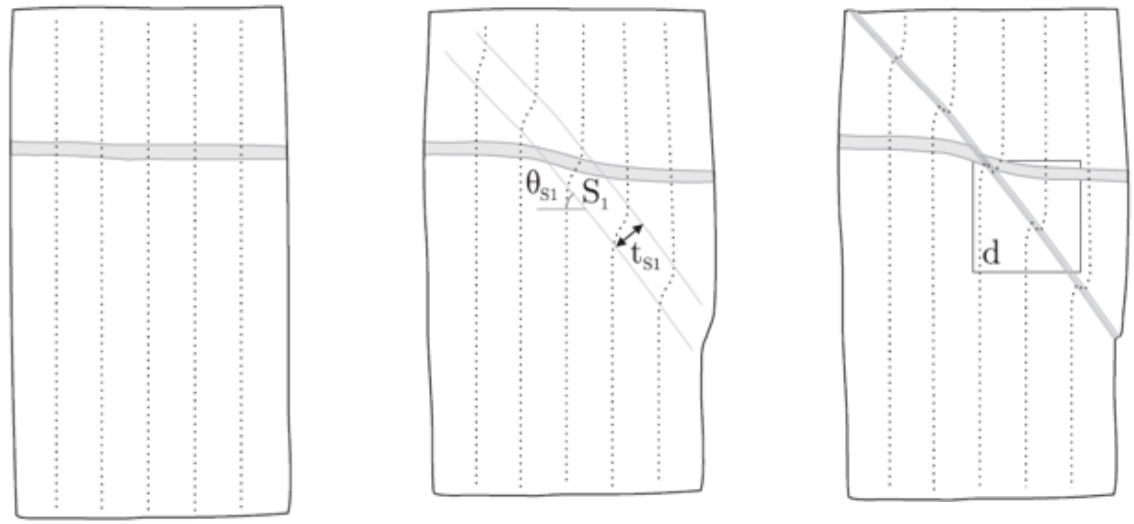

(a) **(b)** **(c)**

Figure 2.2 (a) Sample in pre-peak regime , (b) Sample after onset of strain localization and (c) Fully evolved shear zone [18]

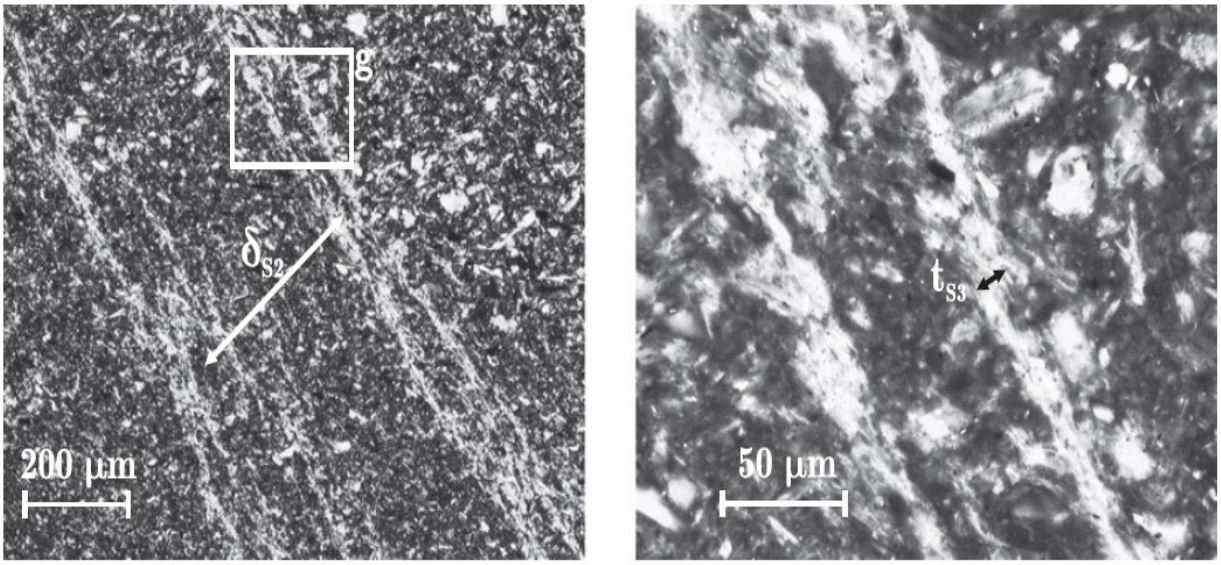

(a) **(b)**

Figure 2.3 (a) Microstructural shear zone under 200 μm and (b) Microstructural shear zone under 50 μm [18]

2.3 True Triaxial Test

Only a limited number of studies, which focused on strain localization of clay have used a TT device, and a majority of those studies tested only sands. Pongpipat et al. [20] studied the effects of intermediate principal stress on behavior of kaolin clay using a series of consolidated-drained TT tests on cross-anisotropic slurry-consolidated kaolin clay. The tests were performed at constant mean effective stress and constant Lode's angle. Clay specimens were tested at a constant back pressure of 100 kPa and a constant mean effective stress of 250 kPa. Vertical strain rate was set to 0.001% per minute, while the horizontal stress remained constant.

Results showed that initiation and development of shear bands caused failure in all tests except CTC (b = 0). In addition, the inception of strain localization occurred while the clay underwent volumetric contraction, and shear bands made angles between 56.1 and 58.1 degrees from the horizontal direction. These orientations remained approximately constant throughout tests and they were not significantly influenced by b-value or initial cross-anisotropy. Low ultimate strength was obtained due to realignment of platy clay particles.

2.4 Hollow Cylinder Test

Saada et al. [21] used an HC apparatus to investigate the effects of cracks on shear band propagation in saturated kaolinite clay specimens subjected to undrained loading. Radial notches were made in selected specimens using a thin, v-shaped brass sheet. Although stress-strain responses of specimens with and without cracks showed minimal differences, specimens with cracks did not exhibit smooth stress-strain curves. Results showed that isotropic consolidation caused more diffuse shear bands than K_o consolidation, which produced clearly defined shear bands. In addition, shear bands in overconsolidated clay samples were thinner and more pronounced than those that formed in normally consolidated samples.

2.5 Biaxial Test

Alshibli and Akbas [14] conducted two undrained plane strain compression tests in Louisiana plane strain apparatus (Figure 2.4). They compared plane strain test results to two undrained CTC experiments and found that undrained shear strength in plane strain experiments was larger than undrained shear strength in CTC experiments. Furthermore, plane strain test specimens failed through a well-defined shear band, while CTC specimens failed via a diffuse bulging mode.

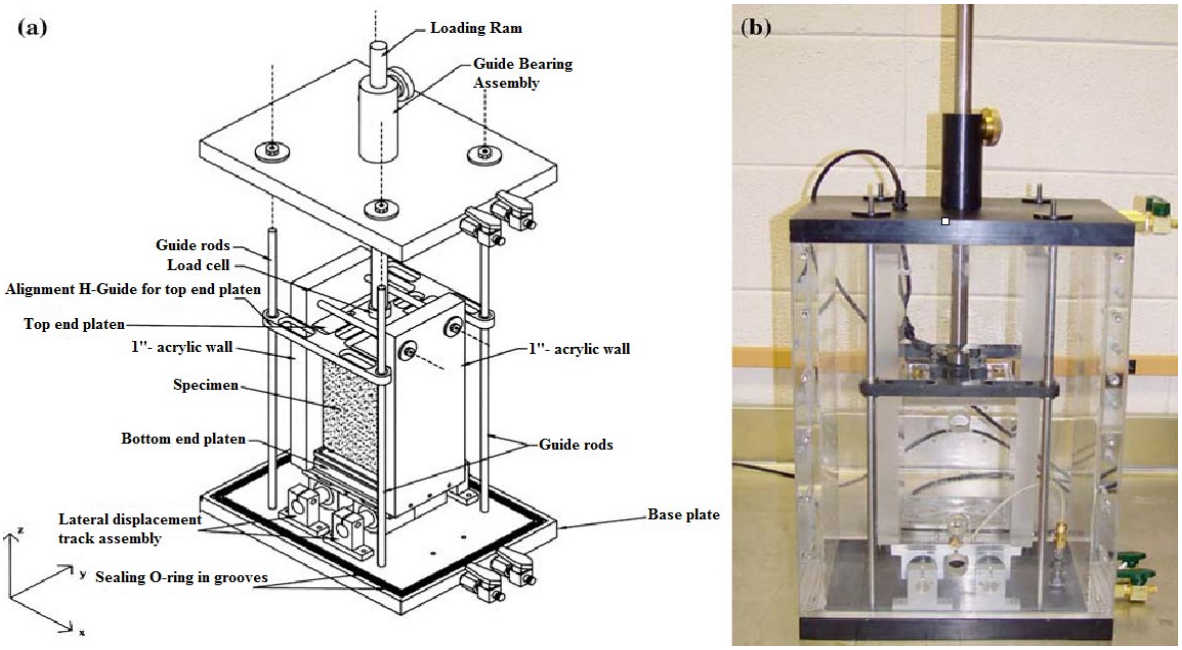

(a) **(b)**

Figure 2.4 (a) Schematic of a plane strain device and (b) Plane strain device [14]

Sengupta [22] conducted a plane strain test on kaolin clay to investigate strain anisotropy using anisotropy of magnetic susceptibility (AMS), which induces magnetism in a clay sample so that induced magnetization can be measured in various directions. Analyses were carried out on core samples taken from inside and outside of shear bands (Figure 2.5). Results showed that a degree of magnetic anisotropy, which gauges strain intensity, was greater in cores with shear bands

than in cores without shear bands. Sengupta [22] found that a threshold value of the degree of magnetic anisotropy was required for shear band formation. Orientation of the principal strain axis showed that reorientation of two principal axes occurred along the shear band.

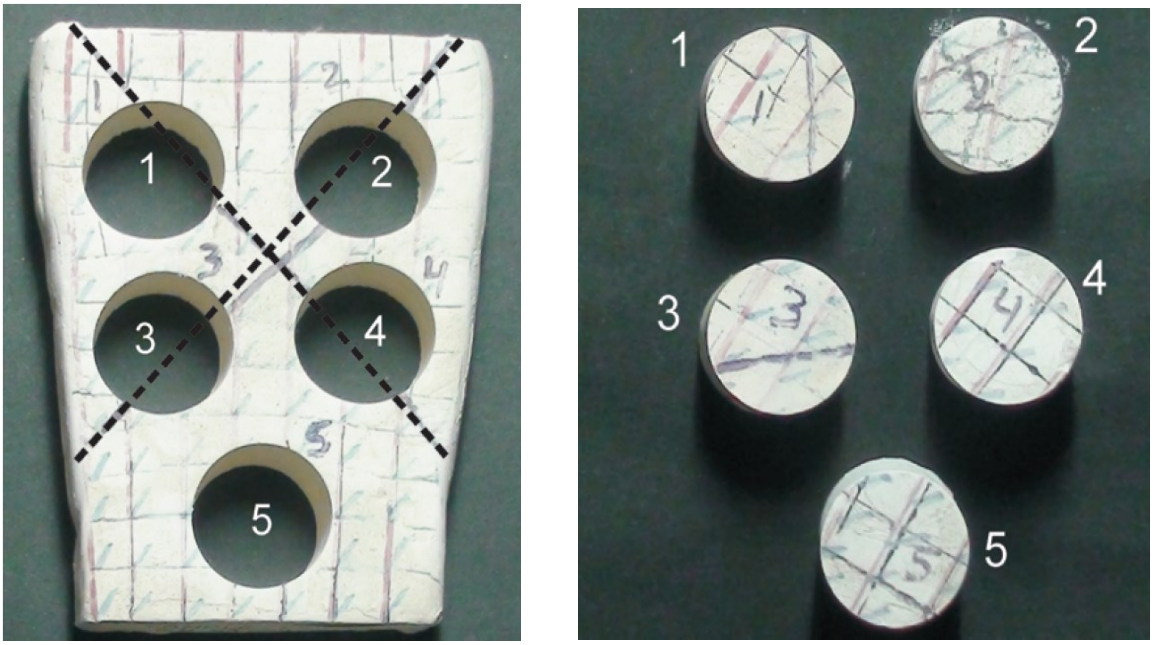

(a) **(b)**

Figure 2.5 (a) Plane strain shear sample and (b) Core samples [22]

It is because well-defined shear bands most often form in plane strain device that it was selected to conduct experimental investigation in this study.

Chapter 3 - Experimental Program

3.1 Introduction

The primary objective of the experimental program was to investigate development of strain localization in overconsolidated clays using a plane strain apparatus. The program investigated effects of stress history and strain rate on strain localization. This chapter describes material properties, a plane strain device, and experimental procedures.

3.2 Material Properties

Georgia kaolin clay was used in this investigation due to its low activity, and subsequently limited sensitivity to various loading rates. Results of the classification tests, including Atterberg's limits and grain size distribution, as well as specific gravity of Georgia kaolin clay are summarized in Table 3.1.

Table 3.1 Atterberg's limits, specific gravity, and grain size distribution tests

Liquid Limit （%）	53
Plastic Limit (%)	32
Plasticity Index (%)	21
Specific Gravity	2.66
Percent (by weight) finer than 0.075 mm	100
Percent (by weight) finer than 0.002 mm	60

3.3 Biaxial Apparatus

3.3.1 Background

Although the biaxial, or plane strain, device was designed to investigate strain localization in geomaterials, it is not a commonly used laboratory apparatus. The device used in this study was a slightly modified version of the apparatus originally designed by Vardoulakis and Goldscheider [23] at the University of Minnesota. Lee [1], Marachi et al. [24] , Peters et al. [3], and Perić et al.

[13] have shown that soil samples tested under plane strain conditions are much more susceptible to strain localization than samples tested in a conventional triaxial apparatus. Furthermore, a biaxial apparatus combines functions of a convectional triaxial apparatus, direct shear apparatus, and possibly a ring shear apparatus.

3.3.2 Biaxial Apparatus Control System

The biaxial apparatus at Northwestern University (NU) in Evanston, Illinois, was used to carry out the experiments for this study. The control system, shown in Figure 3.1, consisted of a back pressure control panel with accessories, a confining pressure controller filled with air and silicon oil, a plane strain compression cell, a series of transducers connected with a data acquisition and computer-controlled system, and a loading frame with a gear box to produce controllable rates of vertical displacement.

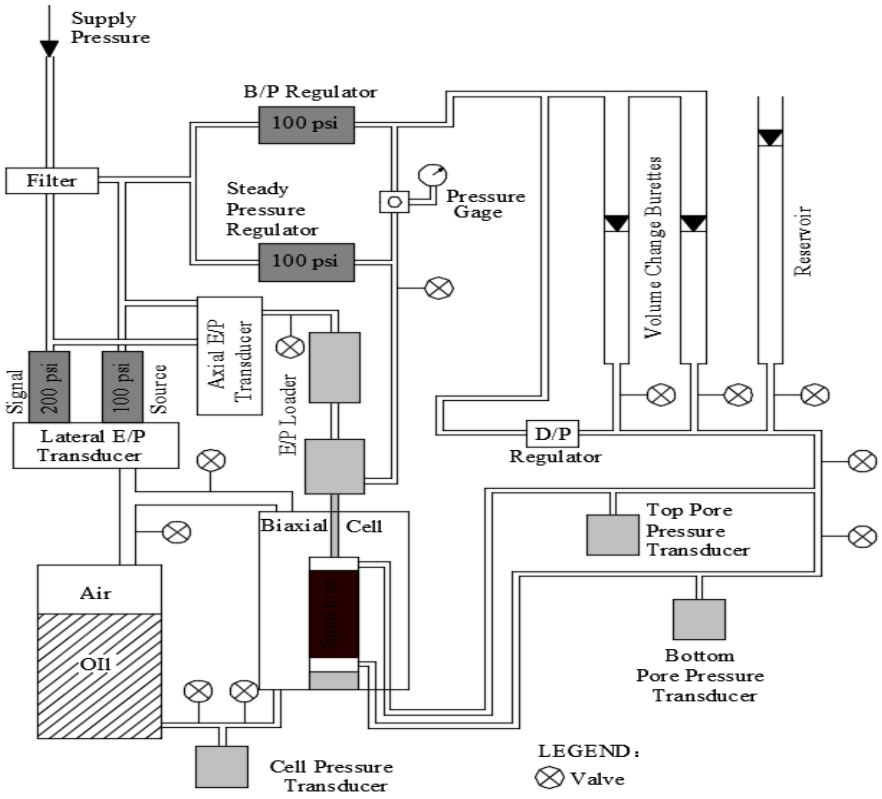

Figure 3.1 Schematic of a biaxial apparatus control system [25]

3.3.3 Biaxial Cell

Figure 3.2 shows a schematic and Figure 3.3 shows a photograph of the biaxial apparatus used in this study. The apparatus was placed inside a cylindrical pressure chamber filled with silicon oil in order to provide a confining pressure. The pressure chamber had an inner diameter of 40 cm, a height of 56.3 cm, and a wall thickness of 3.6 mm. As shown in Figure 3.2, a prismatic specimen (1) with nominal dimensions of 80 x 40 x 140 mm was enclosed within a latex membrane and placed on a lower platen (2) inside the pressure chamber. The specimen was laterally confined by side rigid walls (4) that had a separation distance of 80 mm. The side rigid walls were fixed at the base and attached to each other by tie rods (7), thereby enforcing a constant width of soil specimen equal to 80 mm for the entire experiment. A vertical load was applied through the enlarged upper loading platen (3), while the lower loading platen (2) was placed on a linear bearing sled (5). All surfaces in contact with a soil specimen were glass-lined and lubricated to reduce internal friction.

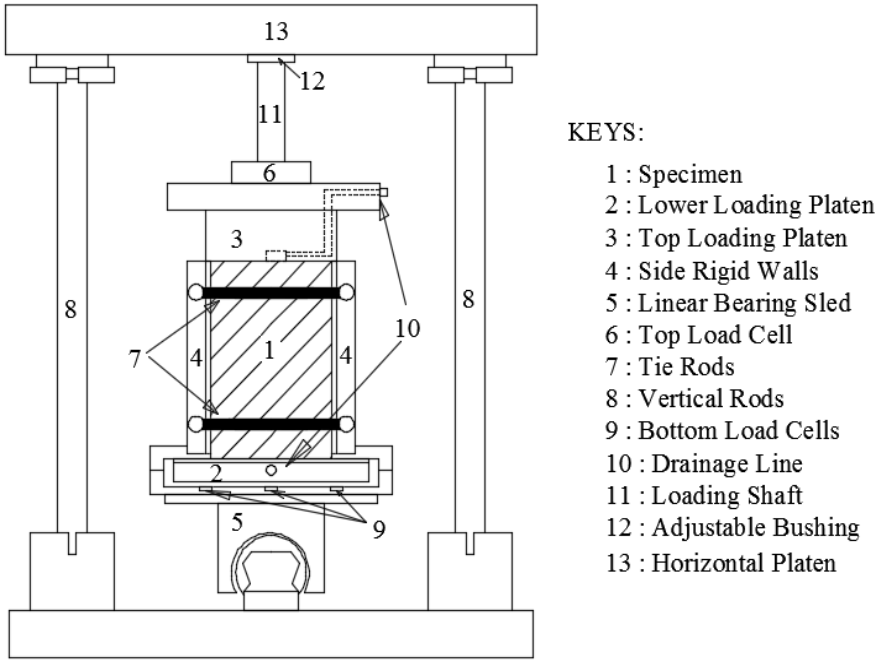

Figure 3.2 Schematic of a biaxial apparatus [25]

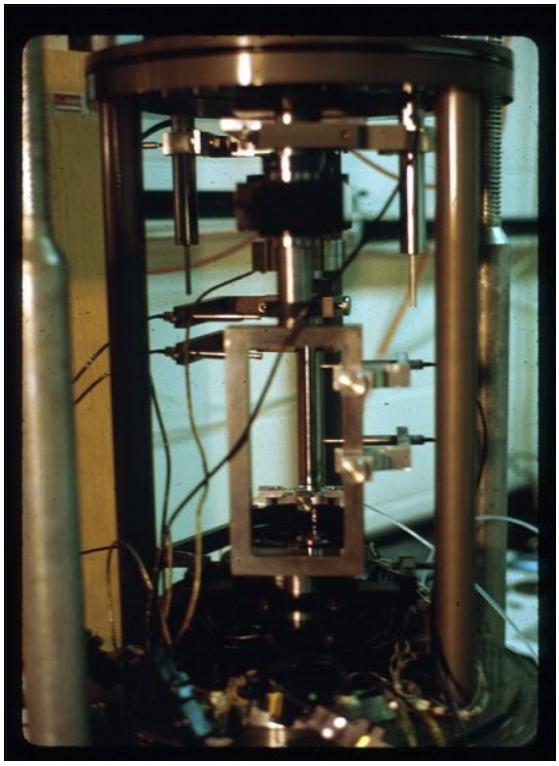

Figure 3.3 Biaxial apparatus [26]

The biaxial cell was internally instrumented to detect the onset and track development of strain localization. Figure 3.4 shows a soil specimen mounted inside the biaxial apparatus, which included 18 internal sensors. Inside the pressure chamber, two linear variable differential transformers (LVDTs) measured axial displacement at the top of a sample. Four additional LVDTs were installed on both sides of the specimen (two on the left side and two on the right side) to measure lateral displacements (Figure 3.4). The LVDT on the upper left side of specimen was denoted as the front top, and the lower left LVDT was denoted as the front bottom. Similarly, at the right side, the upper LVDT was denoted as the back top, and the lower LVDT was denoted as the back bottom. The remaining LVDT measured the sled displacement. Four load cells measured the axial force: one load cell was located at the top of the soil specimen, and three cells were embedded into the bottom platen. The remaining four load cells were embedded into the aluminum

side wall to measure the out-of-plane stress. Two PWP transducers were mounted outside the biaxial cell and connected to the top and bottom drainage lines in order to measure the PWP, as shown in Figure 3.1. Miniature porous stones were embedded into the top and bottom platens, and one cell pressure transducer was used to measure cell pressure. A detailed description of the experimental configuration is presented in Harris [25].

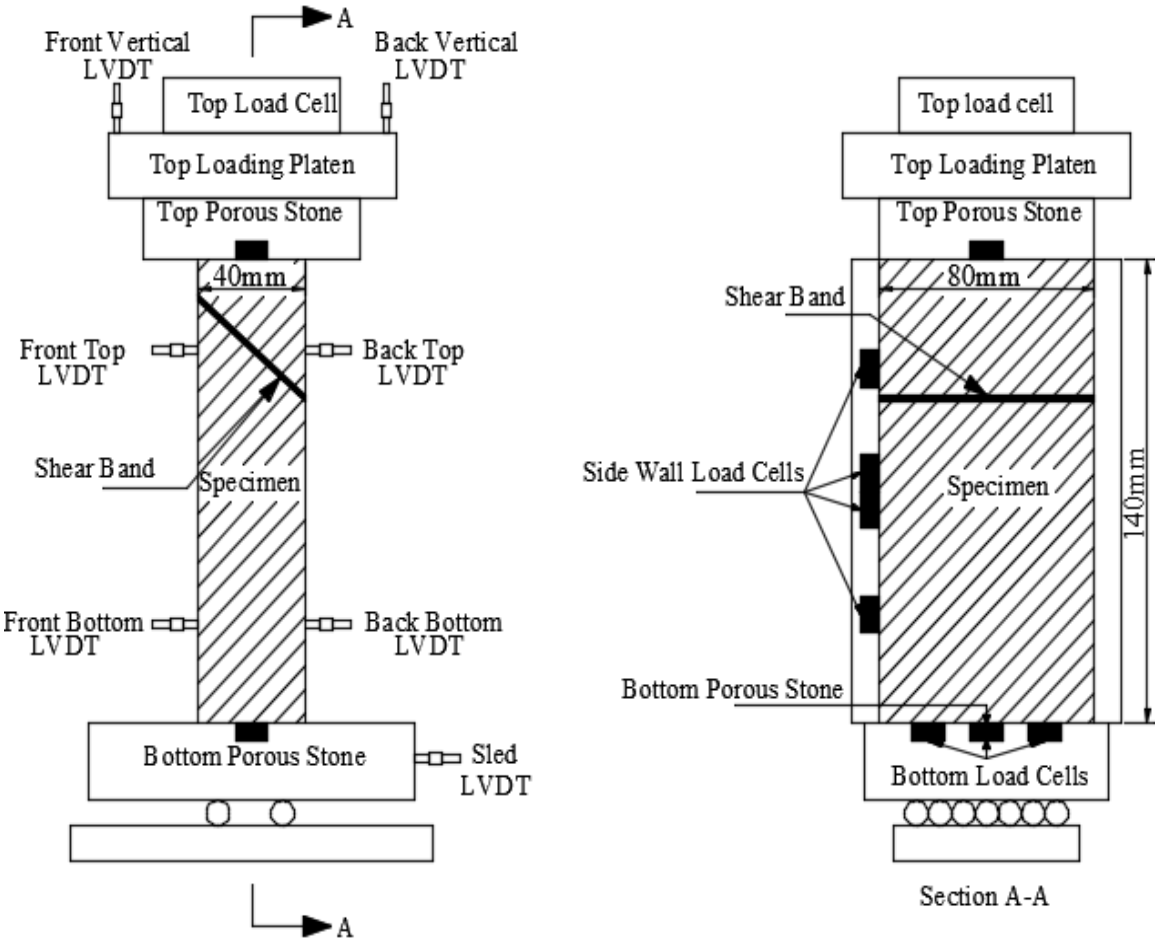

Figure 3.4 Schematic of a soil specimen mounted inside the biaxial device [25].

3.4 Experimental Procedures

This section presents the experimental procedures for this study, including slurry preparation, slurry consolidation, specimen trimming and mounting, and a biaxial test program.

3.4.1 Slurry Preparation

Clay specimens were prepared by thoroughly mixing the desired mass of Georgia kaolin clay powder with deaired water. Water content of the slurry was 2.5 times the liquid limit. A porous stone and filter paper were placed at the bottom of the Lexane cylinder, as shown in Figure 3.5, and thoroughly mixed slurry was carefully poured into the Lexane cylinder using a long-stem funnel.

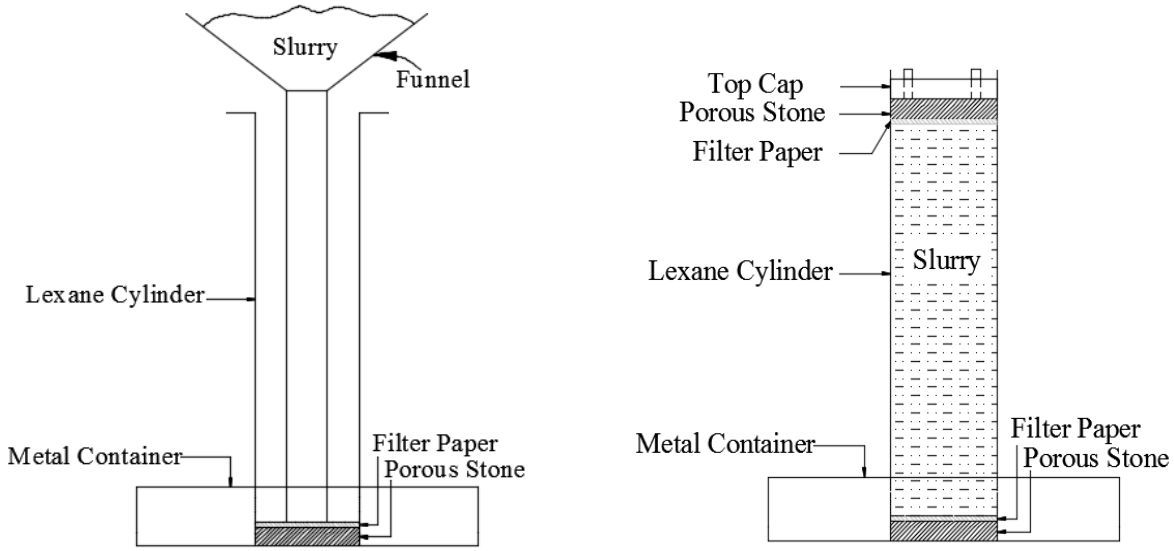

Figure 3.5 (a) Cylinder with funnel and (b) Cylinder filled with slurry

(a) (b)

(b) (d)

Figure 3.6 (a) Georgia kaolin clay powder , (b) De-aired water , (c) Mixing of slurry, and (d) Lexane cylinder filled with slurry [26]

After the Lexane cylinder was filled with the desired amount of slurry, as shown in Figure 3.6(d), a filter paper with porous stone and top cap were placed on the top of the slurry. To minimize air entry, the bottom of the funnel was slowly lifted while the cylinder was filled.

3.4.2 Slurry Consolidation

The process of slurry consolidation is depicted in Figure 3.7. The slurry was consolidated for approximately seven days by subjecting it to the constant rate of deformation corresponding to a vertical displacement rate of 0.0208 mm/min. This strain rate produced a sufficiently uniform excess PWP based on the finite strain theory of consolidation [27]. At the end of primary consolidation, the height of a specimen was equal to approximately 44% of the initial height of slurry.

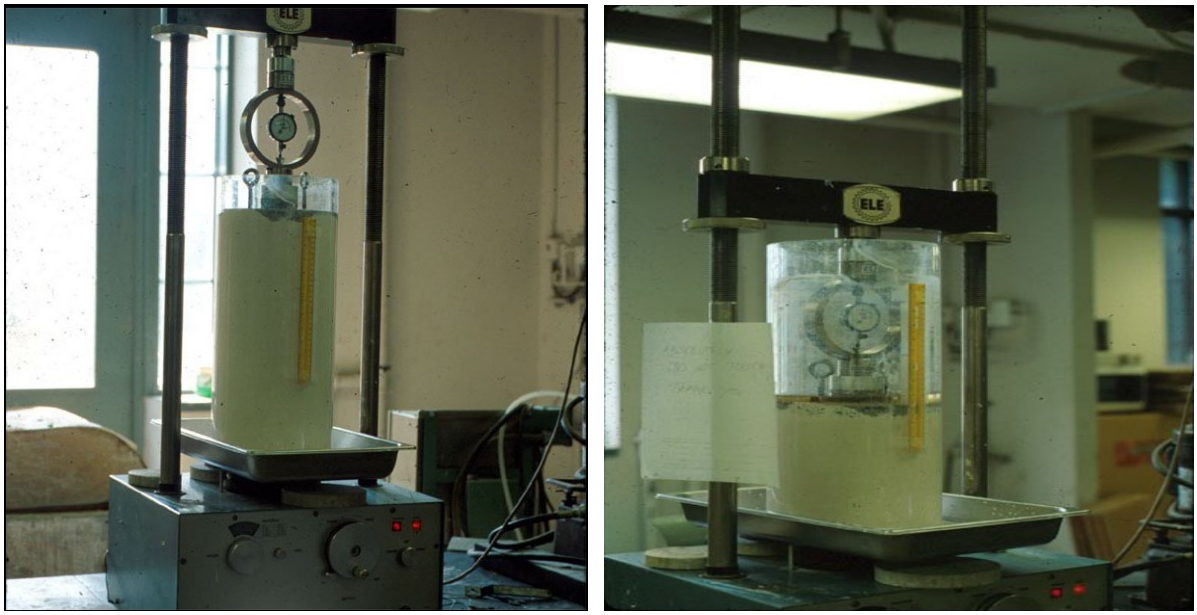

(a) **(b)**

Figure 3.7 (a) Beginning of consolidation and (b) End of consolidation [26]

3.4.3 Specimen Trimming and Mounting

After the primary consolidation was complete, the clay block was extracted from the Lexane cylinder and trimmed. Figure 3.8 shows large and small molds and a fine wire saw used to trim clay specimens. A prismatic specimen was trimmed to dimensions of 80 × 40 × 140 mm. Figure 3.9 shows the final shape of a trimmed clay specimen.

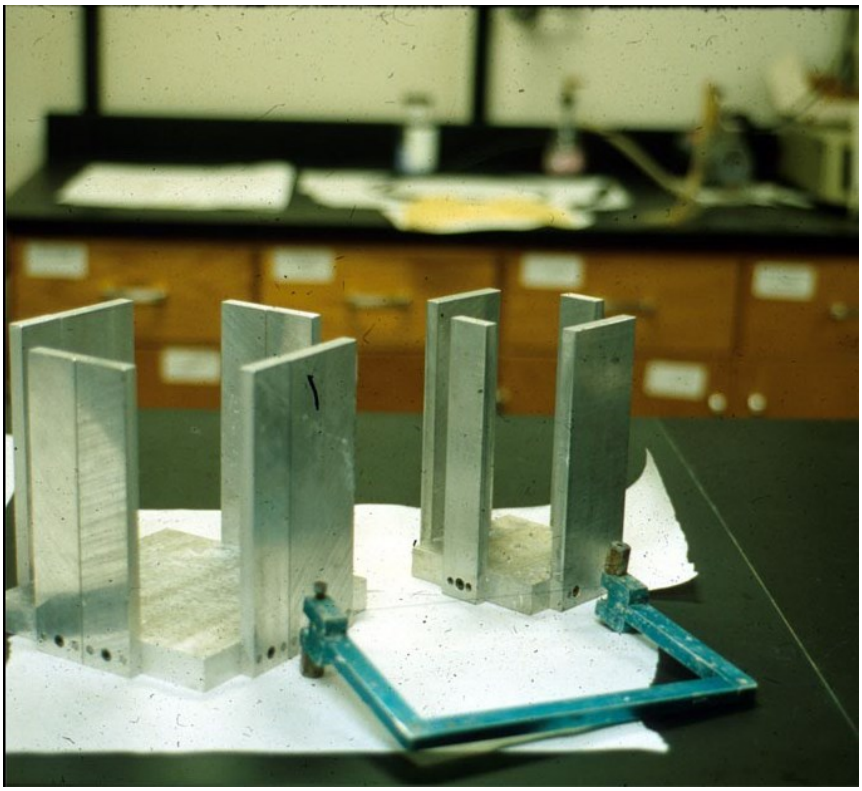

Figure 3.8 Large and small molds with trimmer [26]

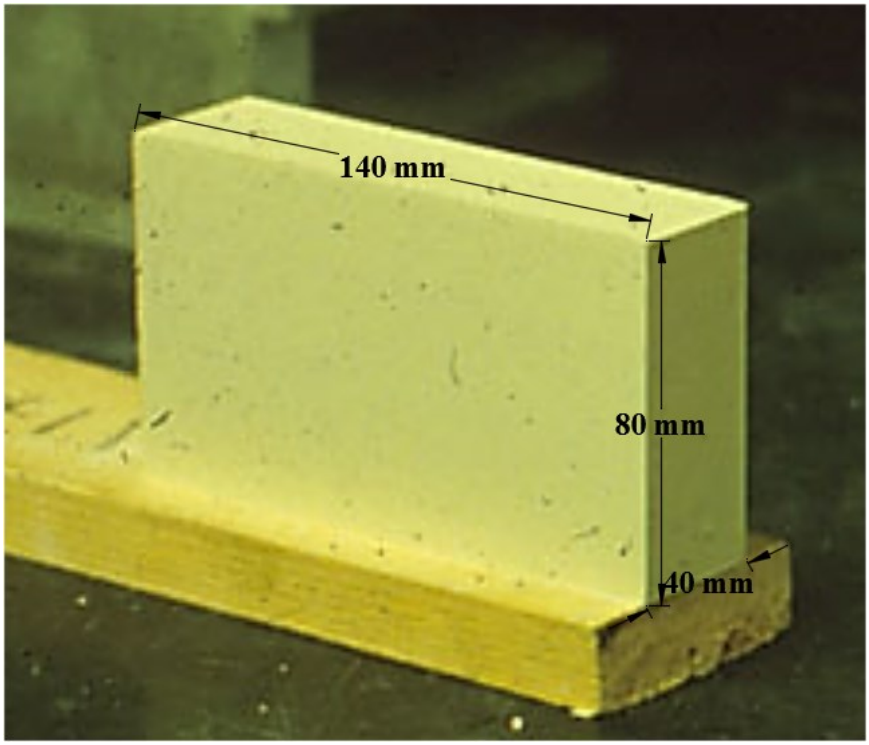

Figure 3.9 Trimmed clay specimen [26]

After trimming, specimens were measured and weighed prior to mounting into the biaxial cell. They were enclosed with a latex membrane on which a rectangular grid was printed with vertical and horizontal line spacings of 5 mm. The grid was used to identify the location of shear bands. Figure 3.10 shows the mounted clay specimen with a latex membrane.

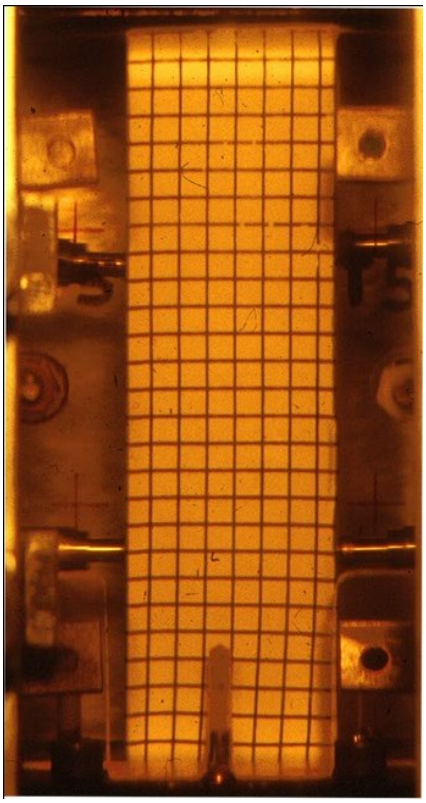

Figure 3.10 Mounted clay specimen with a latex membrane [26]

3.4.4 Biaxial Test Program

The biaxial test program was designed to investigate the effects of stress history and strain rate on undrained plane strain response of Georgia kaolin clay. Six undrained plane strain compression tests were completed; each test consisted of plane strain consolidation and undrained plane strain compression to failure. The test program is summarized in Table 3.2, where the subscript "c" denotes the values of different variables at the end of the primary consolidation stage.

Table 3.2 Summary of biaxial test program

Test Information / Test Name		p'_c	q_c	θ_c	$\dot{\varepsilon}_a$	e_c	OCR
		kPa	kPa	Degree	% / hour		
Test #1	**PS-57F**	57.37	11.54	49.00	3.26	1.05	2.82
Test #2[1]	-	-	-	-	-	-	-
Test #3	**PS-55F/S**	55.17	8.49	59.00	4.81/0.37	1.05	2.91
Test #6	**PS-61S**	60.58	0.67	34.00	0.36	1.05	2.66
Test #4	**PS-139F**	139.32	9.36	1.00	3.71	0.97	1.16
Test #5	**PS-139S**	139.10	7.58	1.00	0.32	0.94	1.16

[1] Due to a malfunction of the internal instrumentation, Test #2 was discarded.

A total mean stress (p) and a mean effective stress (p') are defined as

$$p = \frac{\sigma_x + \sigma_y + \sigma_z}{3} \quad \text{and} \quad p' = \frac{\sigma'_x + \sigma'_y + \sigma'_z}{3} \qquad \textbf{Equation 3.1}$$

where σ_x, σ_y, σ_z are total principal stresses as shown in Figure 3.11, while σ'_x, σ'_y, σ'_z are principal effective stresses in x, y, and z directions, respectively. Values of mean effective stress at the end of consolidation (p'_c) were obtained by replacing σ'_x, σ'_y and σ'_z with σ'_{xc}, σ'_{yc}, and σ'_{zc} in Equation 3.2, and p'_c for all tests are listed in Table 3.2.

A deviatoric stress (q) is defined as

$$q = \frac{1}{\sqrt{2}}\sqrt{(\sigma'_x - \sigma'_y)^2 + (\sigma'_x - \sigma'_z)^2 + (\sigma'_y - \sigma'_z)^2} \quad . \qquad \textbf{Equation 3.2}$$

Thus, a deviatoric stress at the end of consolidation (q_c) is calculated by replacing σ'_x, σ'_y, σ'_z with σ'_{xc}, σ'_{yc}, and σ'_{zc} in Equation 3.2,respectively. A Lode's angle θ is defined as

$$cos3\theta = \frac{9}{2}\frac{tr\boldsymbol{s}^3}{q^3} \qquad \textbf{Equation 3.3}$$

where $\boldsymbol{s}$ denotes a deviator stress tensor, which is given by

$$\boldsymbol{s} = \begin{bmatrix} s_x & 0 & 0 \\ 0 & s_y & 0 \\ 0 & 0 & s_z \end{bmatrix} = \begin{bmatrix} \sigma_x & 0 & 0 \\ 0 & \sigma_y & 0 \\ 0 & 0 & \sigma_z \end{bmatrix} - p\begin{bmatrix} 1 & 0 & 0 \\ 0 & 1 & 0 \\ 0 & 0 & 1 \end{bmatrix}. \qquad \textbf{Equation 3.4}$$

It is noted that θ =0° represents conventional triaxial compression ($\sigma_z \geq \sigma_x = \sigma_y$), while θ =60° represents conventional triaxial extension ($\sigma_x = \sigma_y \geq \sigma_z$). A Lode's angle at the end of consolidation (θ_c) was obtained by replacing σ_x , σ_y and σ_z with σ_{xc} , σ_{yc} and σ_{zc}, respectively.

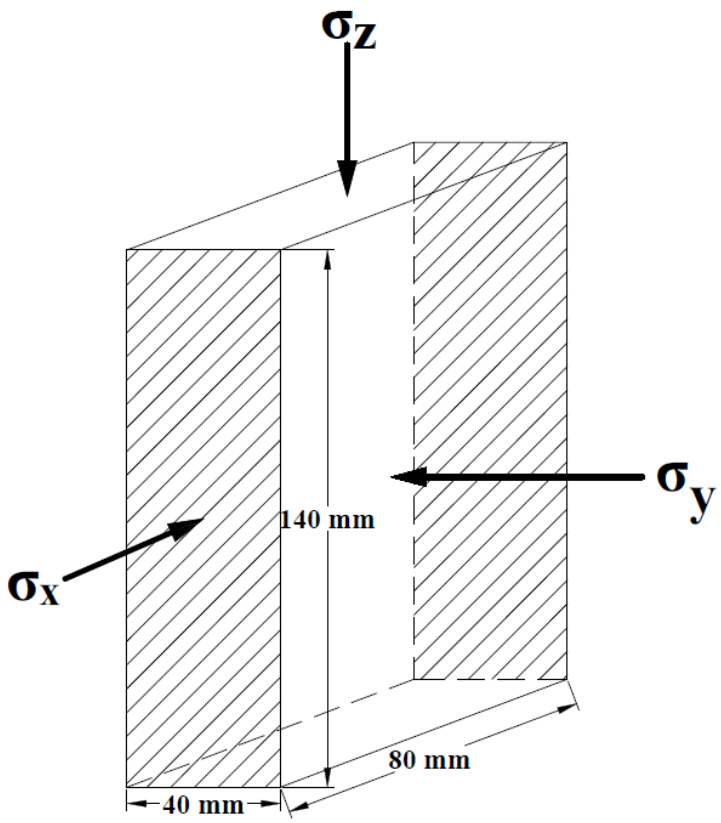

Figure 3.11 Principal stress directions

In Table 3.2, $\dot{\varepsilon_a}$ denotes an axial strain rate during compression to failure, while e_c denotes a void ratio at the end of consolidation. Two groups of strain rates were used: a slow rate corresponding to approximately 0.35% per hour and a fast rate corresponding to approximately 3.49% per hour. The final undrained compression stage was performed in the mixed control mode whereby strain rates in the vertical direction and out-of-plane horizontal directions and total stress rate in the other horizontal direction were maintained constant. Specifically, $\dot{\varepsilon_x} = \dot{\sigma_y} = 0$ and $\dot{\varepsilon_z} =$ constant value.

Alternative test names in Table 3.2 indicate consolidation, mean effective stress, and the axial (vertical) strain rate. For example, Test #4 is alternatively named as PS-139F, indicating that it is a plane strain test (PS) with a consolidation mean effective stress of 139 kPa and that the sample was subjected to a fast strain rate (F). Finally, the overconsolidation ratio (OCR) is defined as

$$OCR = \frac{p'_{max}}{p'_c} \qquad \textbf{Equation 3.5}$$

where the past maximum mean effective stress (p'_{max}) was experienced during K_o slurry consolidation. Thus, p'_{max} is given by

$$p'_{max} = \frac{\sigma'_{z,max}}{3}(1 + 2K_o) \qquad \textbf{Equation 3.6}$$

where $\sigma'_{z,max}$ was equal to 210 kPa. The coefficient of lateral earth pressure at rest (K_o) was determined based on results of triaxial tests on a kaolin clay [28]. K_o for normally consolidated clay is given by

$$K_o = 1 - sin\emptyset' \qquad \textbf{Equation 3.7}$$

where $\emptyset'$ is the internal friction angle of kaolin clay, which is equal to 20.1^{o} [28] at critical state.

In summary, tests PS-139F (T4) and PS-139S (T5) were conducted on lightly overconsolidated samples, while tests PS-57F (T1), PS-55 F/S (T3), and PS-61S (T6) were conducted on heavily overconsolidated clay samples. Furthermore, axial strain rates in PS-139F and PS-57FS were approximately 10 times larger than axial strain rates in PS-139S, PS-55F/S, and PS-61S. Therefore, the tests were grouped into slow tests (T3, T5, and T6) and fast tests (T1 and T4). The axial strain rate in Test #3 changed from fast to slow rate shortly after the test commenced. Consequently, two axial strain rates were contained in Test #3 (PS-55F/S).

Chapter 4 - Results and Discussion

4.1 Results

This section presents results of biaxial tests on Georgia kaolin clay that were conducted in the modified plane strain apparatus. Each test identified events based on lateral displacements, PWPs, deviatoric stress, mean effective stress, and a deviatoric stress-to-mean effective stress ratio. PWPs were measured at the top and bottom of each sample. Eight events were identified in each experiment: onset of strain localization (O), maximum deviatoric stress ($Max\ q$), maximum deviatoric-to-mean effective stress ratio ($Max\ q/p'$), maximum average PWP ($Max\ u_{ave}$), end (E) of shear band propagation, minimum average PWP ($Min\ u_{ave}$), minimum deviatoric-to-mean effective stress ratio ($Min\ \ q/p'$), and minimum deviatoric stress ($Min\ q$). Shear band formation was also observed and photographed during each test.

4.1.1 Onset and End

The inception of strain localization, which occurs as the axial strain reaches a level that closely corresponds to the onset of nonuniform lateral strain, is associated with shear band initiation. In this study the onset of strain localization was determined based on measurements obtained from lateral LVDTs by measuring sample width change near the top and bottom of the specimen. The difference between these two width changes was plotted against axial strain, as shown in Figure 4.1 and Figure 4.2, for heavily overconsolidated samples (Tests #1, #3, and #6) and lightly overconsolidated samples (Tests #4 and #5). Additional results showing LVDT displacements are provided in Appendix A .

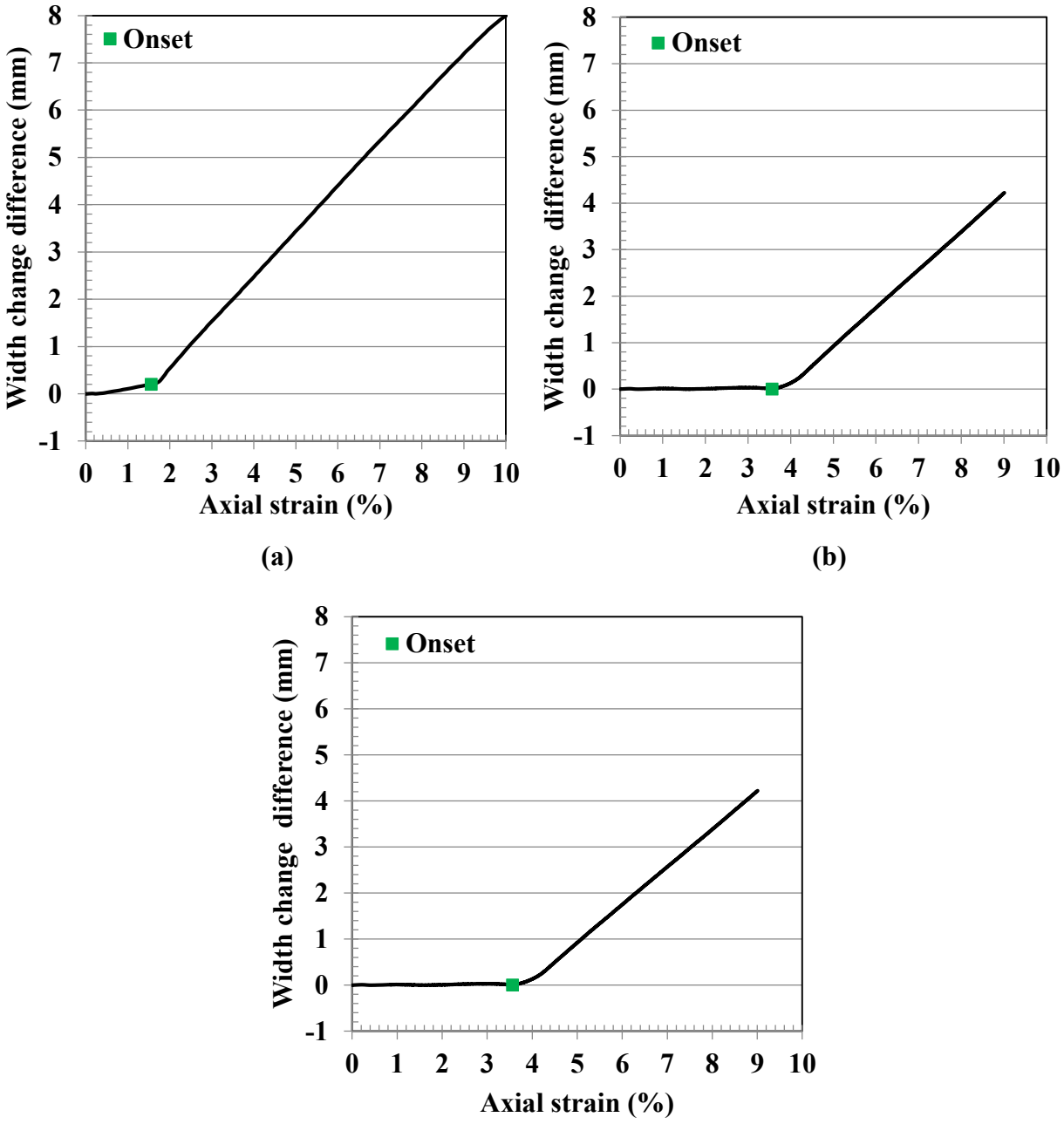

Figure 4.1 Width change difference versus axial strain for (a) Test #1, (b) Test #3, and (c) Test #6

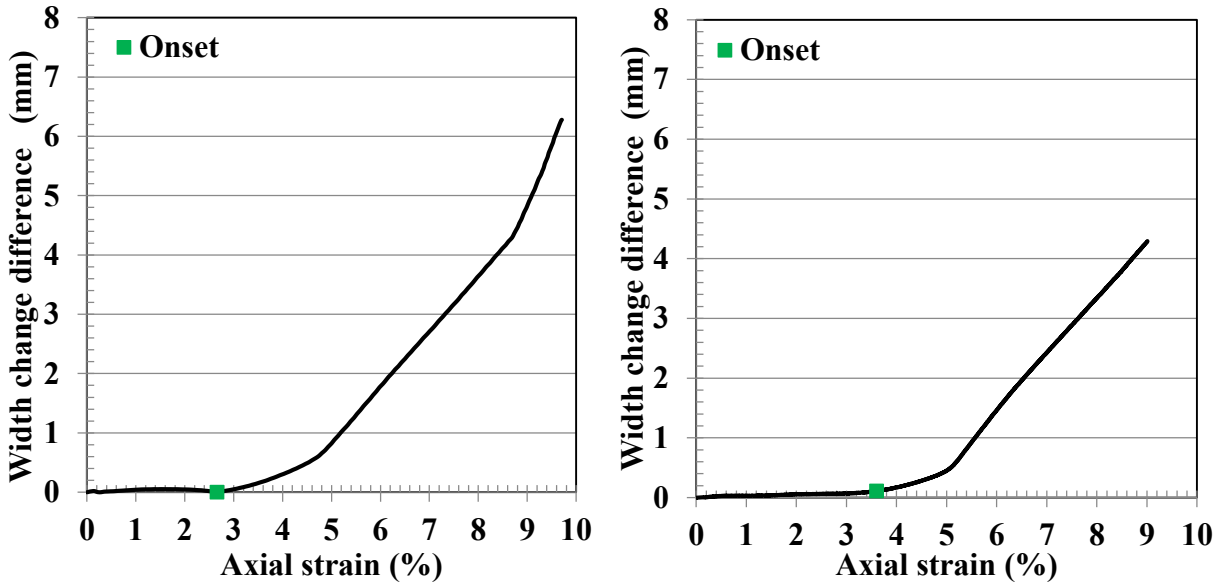

Figure 4.2 Width change difference versus axial strain for (d) Test #4 and (e) Test #5

A deformation band began to propagate across the sample as loading continued. Propagation was complete once a shear band traversed a sample, thereby enabling the sled to start moving (Figure 4.3 and Figure 4.4) in conjunction with the end of a propagation phase. The top width change and bottom width change is shown in Figure 4.5 and Figure 4.6, including an onset of strain localization and an end of shear band propagation.

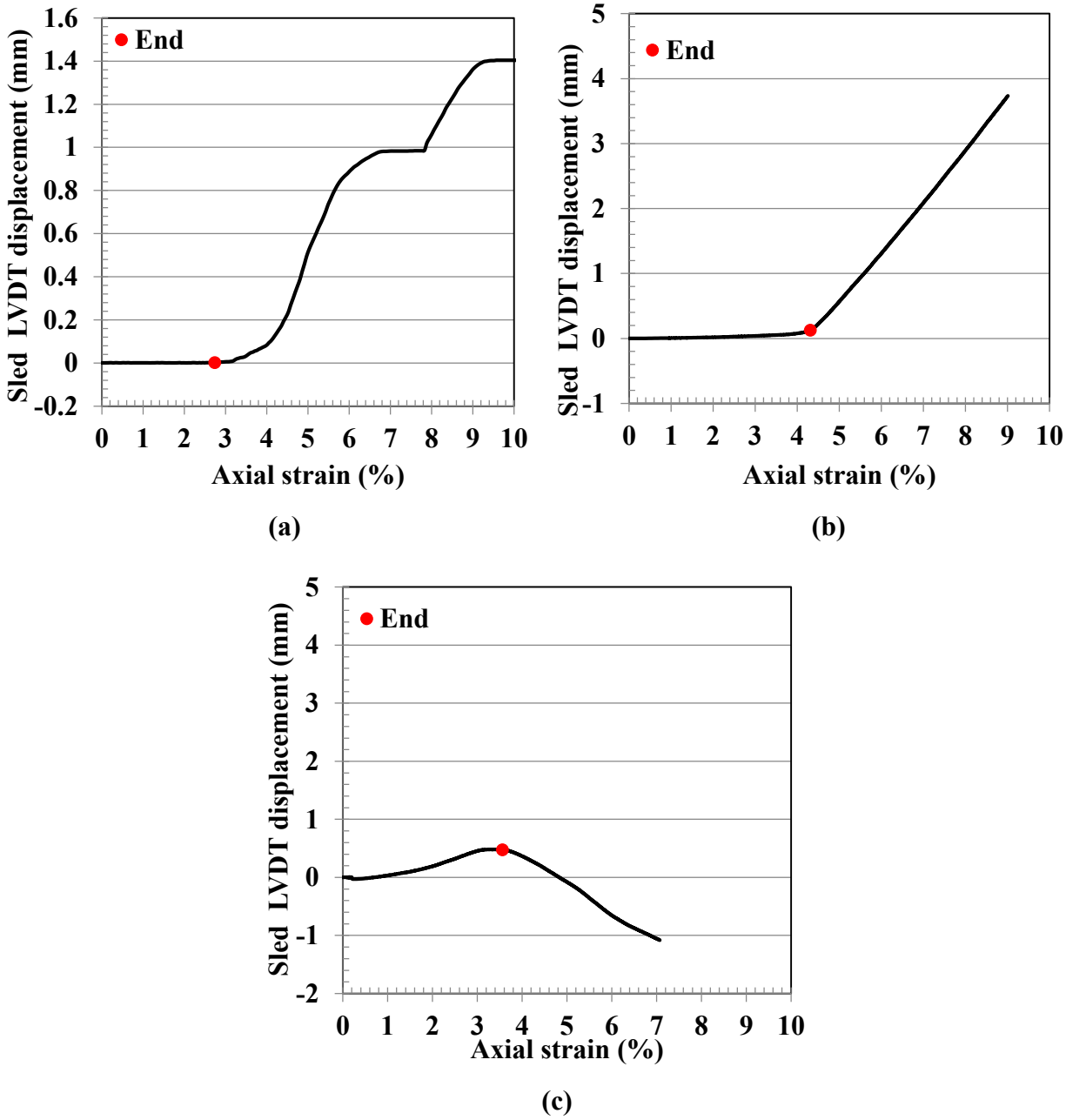

Figure 4.3 Sled LVDT displacement versus axial strain for (a) Test #1, (b) Test #3, and (c) Test #6

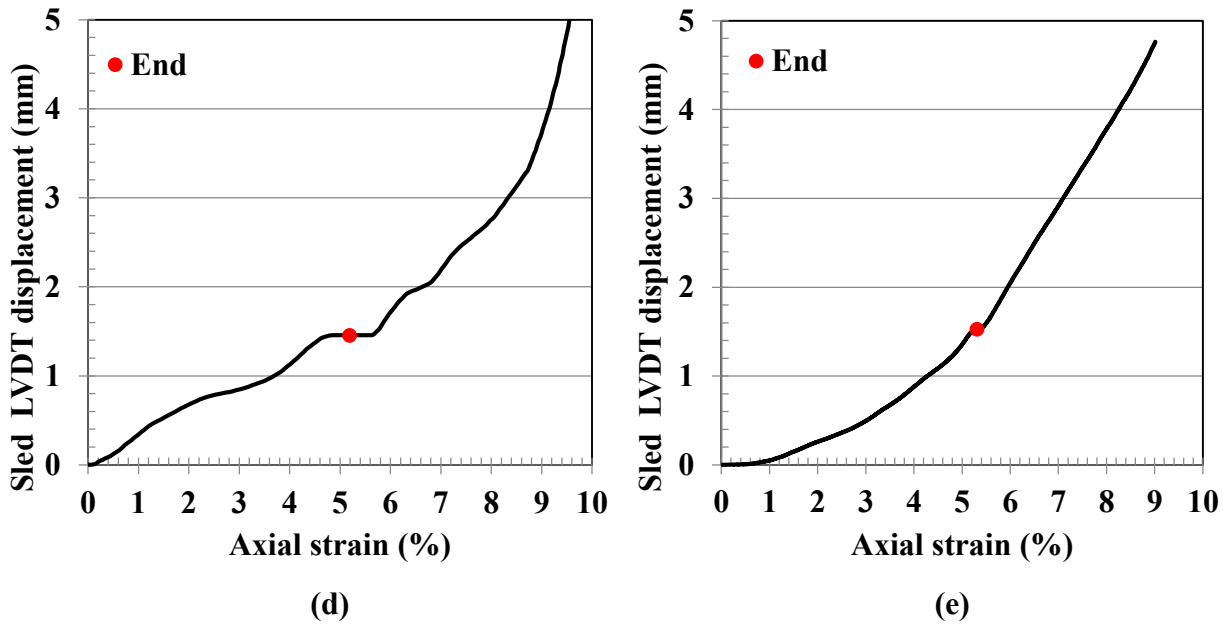

Figure 4.4 Sled LVDT displacement versus axial strain for (d) Test #4 and (e) Test #5

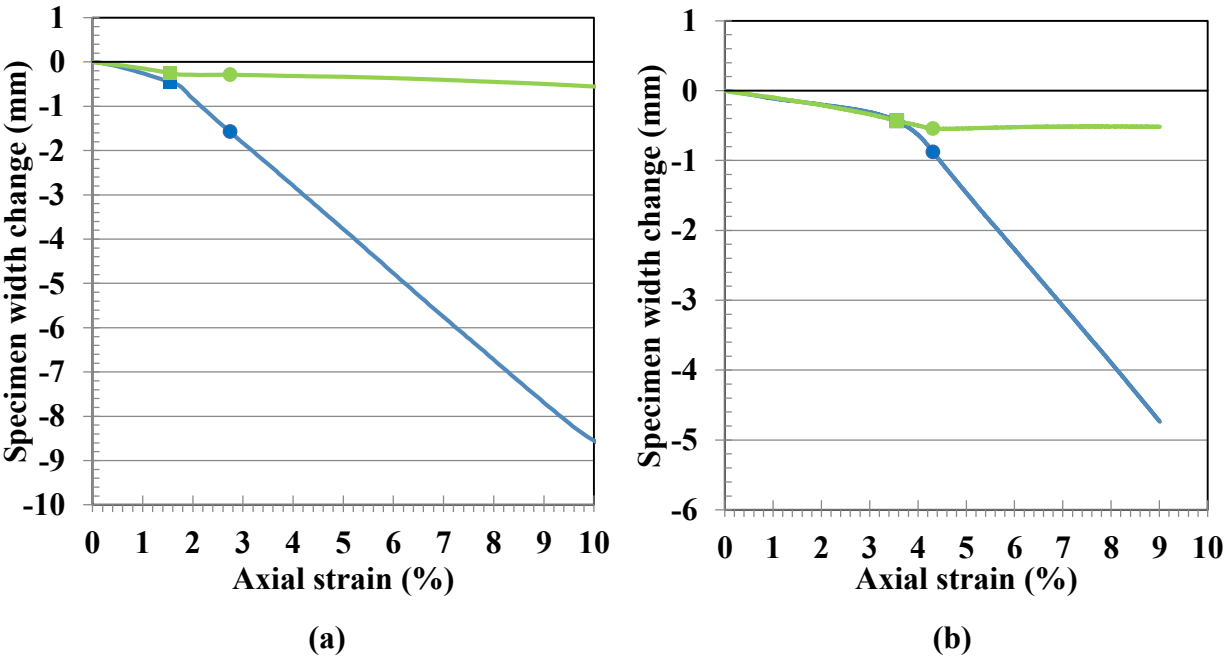

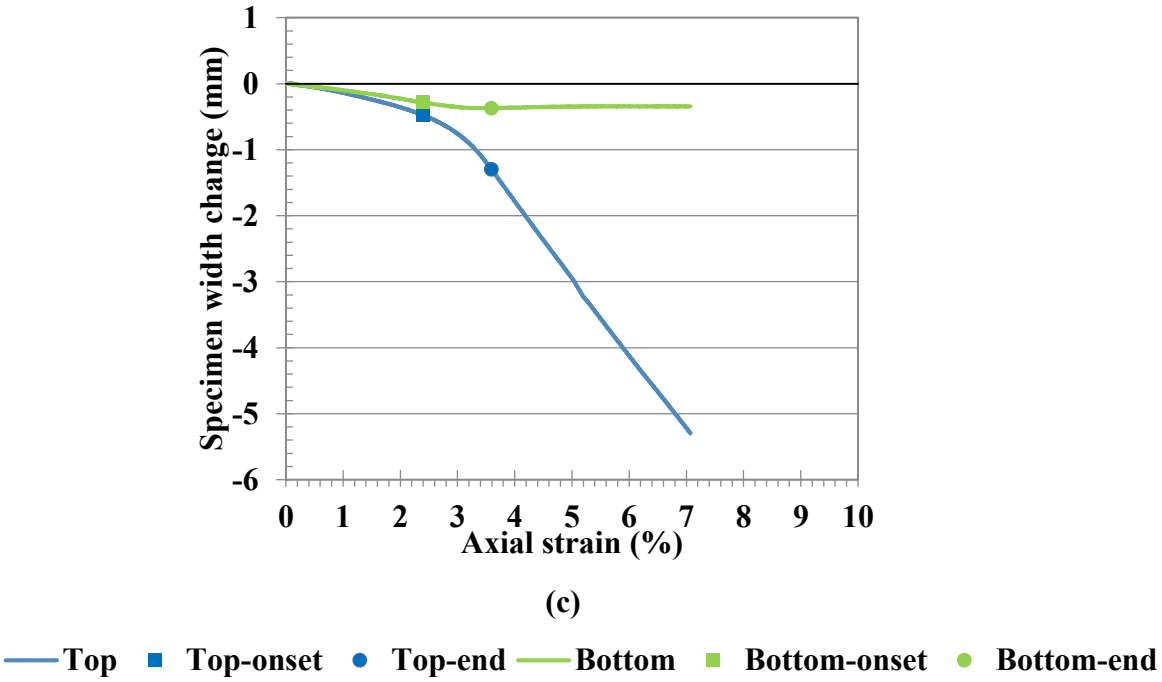

Figure 4.5 Specimen width change versus axial strain for (a) Test #1, (b) Test #3, and (c) Test #6

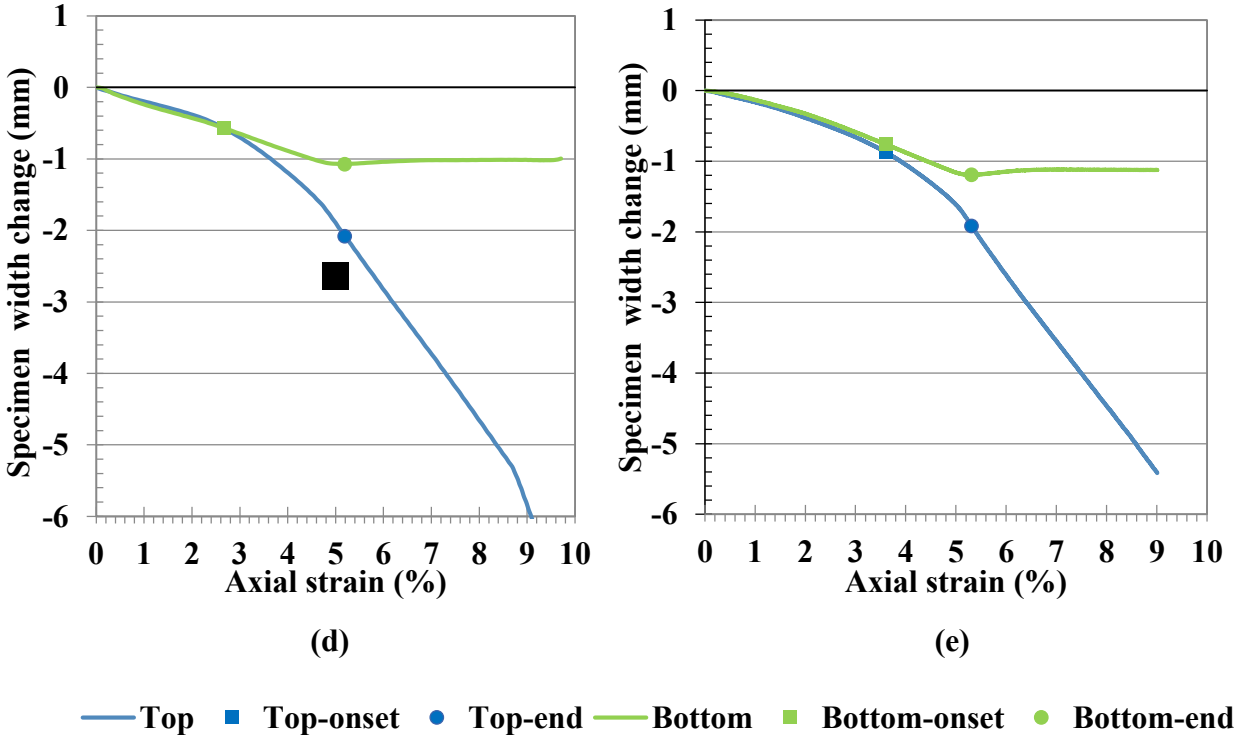

Figure 4.6 Specimen width change versus axial strain for (d) Test #4 and (e) Test #5

4.1.2 Deviatoric Stress

Figure 4.7 and Figure 4.8 show deviatoric stress (q) versus axial (vertical) strain for each test. Maximum and minimum deviatoric stresses ($Max\ q$ and $Min\ q$) were also determined. Although Equation 3.2 (Section 3.4.4) implies that deviatoric stress is always positive, Figure 4.7 shows negative values of deviatoric stress that correspond to the vertical extension. This adjustment was used to obtain smooth response curves. Results showed that the axial strain rate in Test #3 changed from 4.81% per hour to 0.37% per hour at approximately 0.7% axial strain, as shown in Figure 4.7 (b). However, few loading, unloading, and reloading cycles were accidently applied at the beginning of Test # 6, as demonstrated in Figure 4.7 (c). A summary response showing deviatoric stress versus axial strain for all tests is depicted in Figure 4.9, and a summary response of heavily overconsolidated samples is plotted in Figure 4.10. Lightly overconsolidated samples are shown in Figure 4.11.

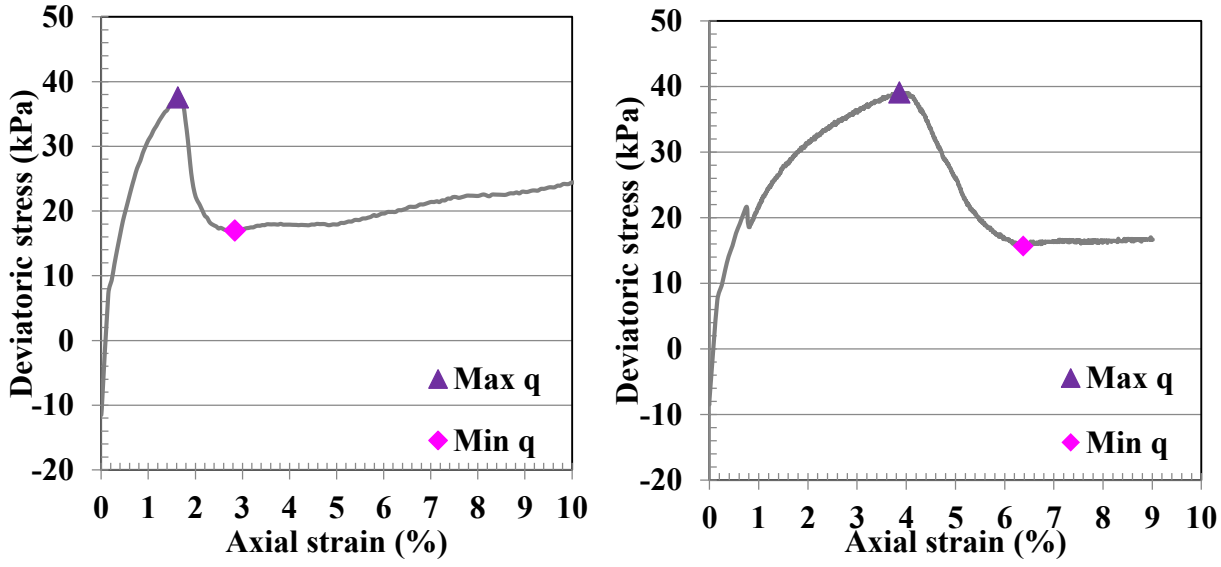

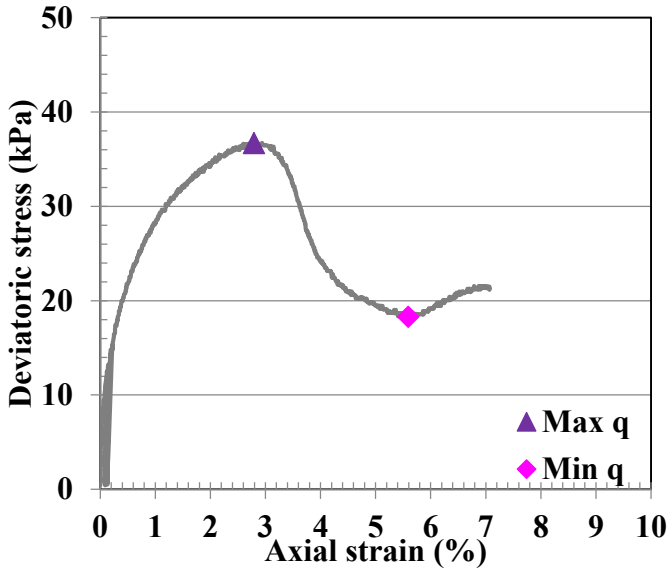

(c)

Figure 4.7 Deviatoric stress versus axial strain for (a) Test #1, (b) Test #3, and (c) Test #6

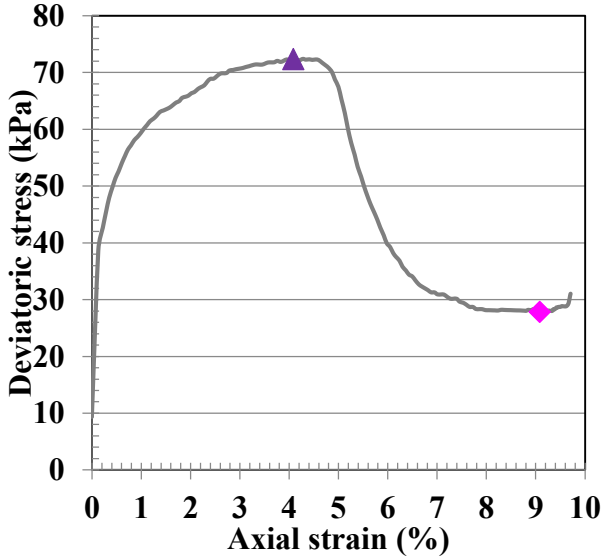

(d)

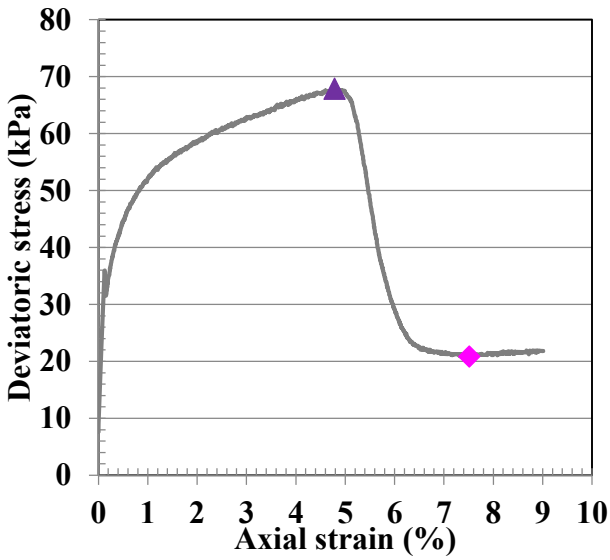

(e)

Figure 4.8 Deviatoric stress versus axial strain for (d) Test #4 and (e) Test #5

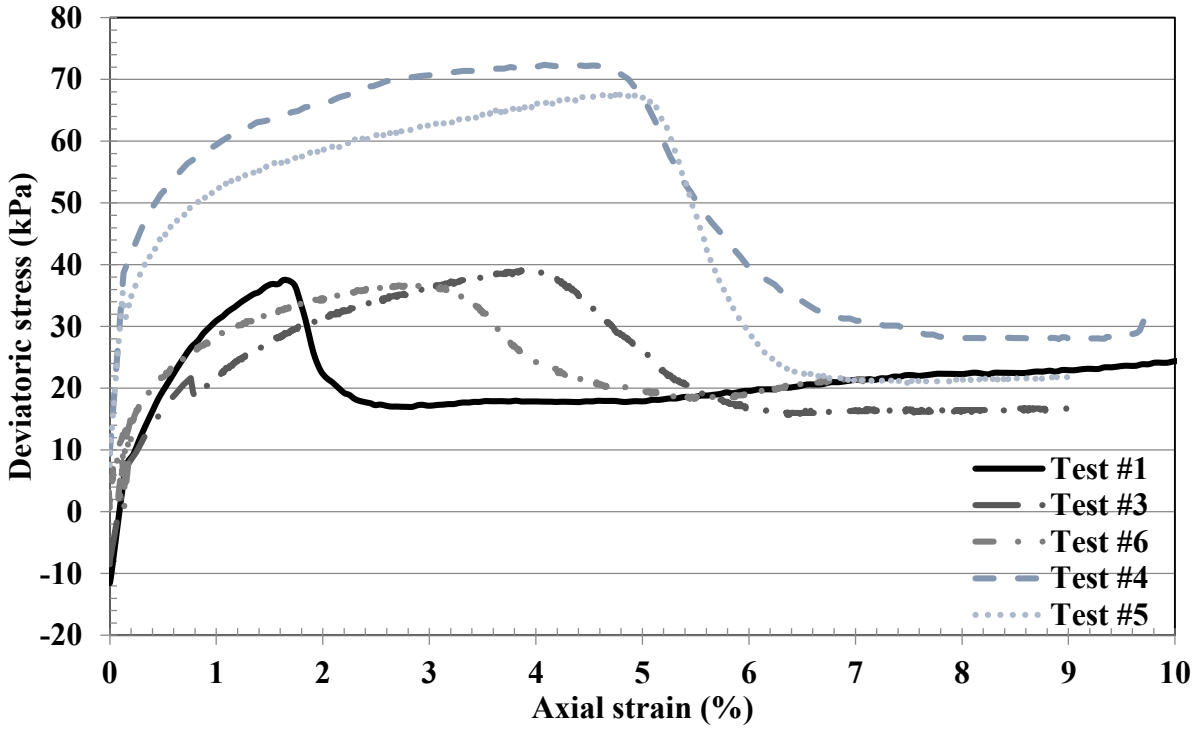

Figure 4.9 Deviatoric stress versus axial strain for all tests

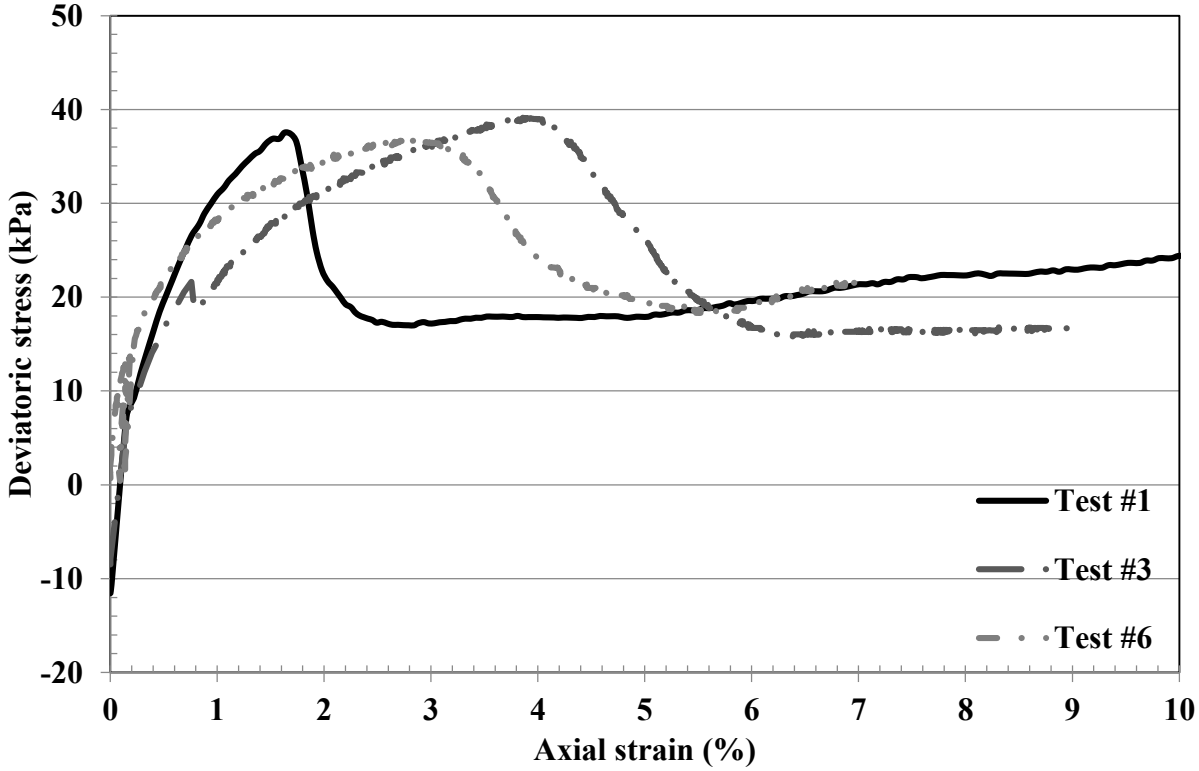

Figure 4.10 Deviatoric stress versus axial strain (Tests #1, #3, and #6)

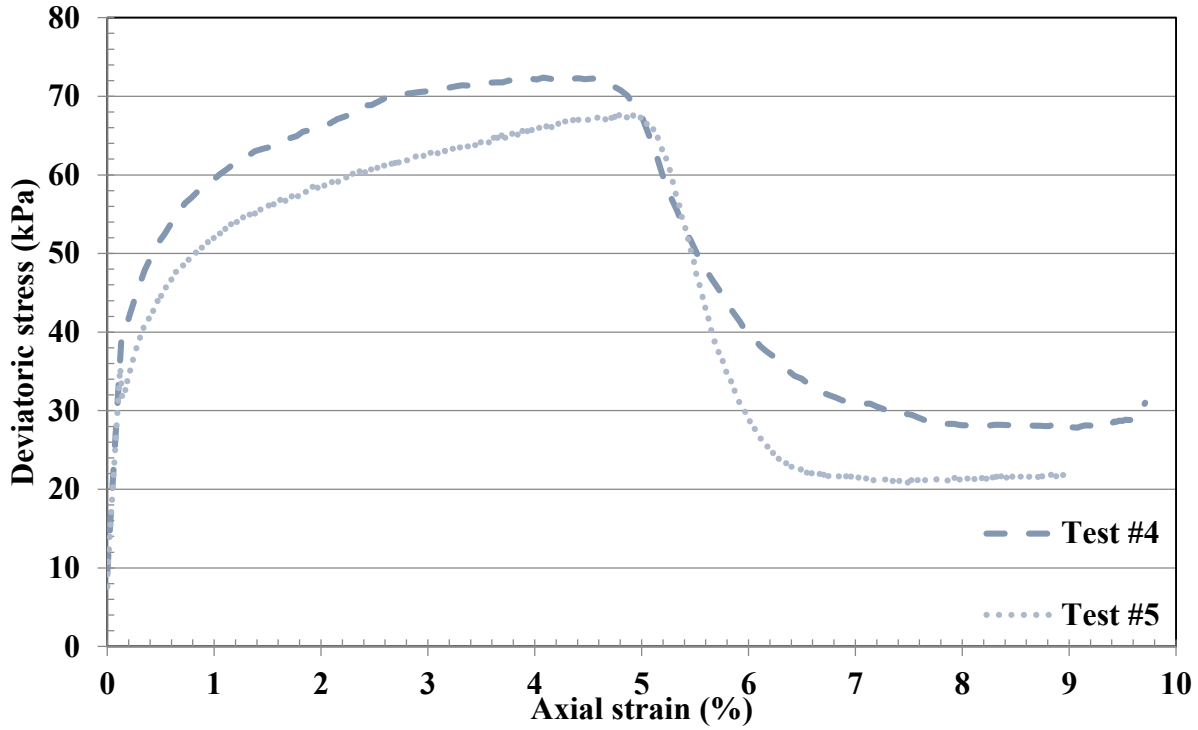

Figure 4.11 Deviatoric stress versus axial strain (Tests #4 and #5)

4.1.3 Pore Water Pressure

PWP was recorded at the top and bottom of each sample with their average value (u_{ave}), maximum average PWP ($Max\ u_{ave}$), and minimum average PWP ($Min\ u_{ave}$), as shown in Figure 4.12 and Figure 4.13.

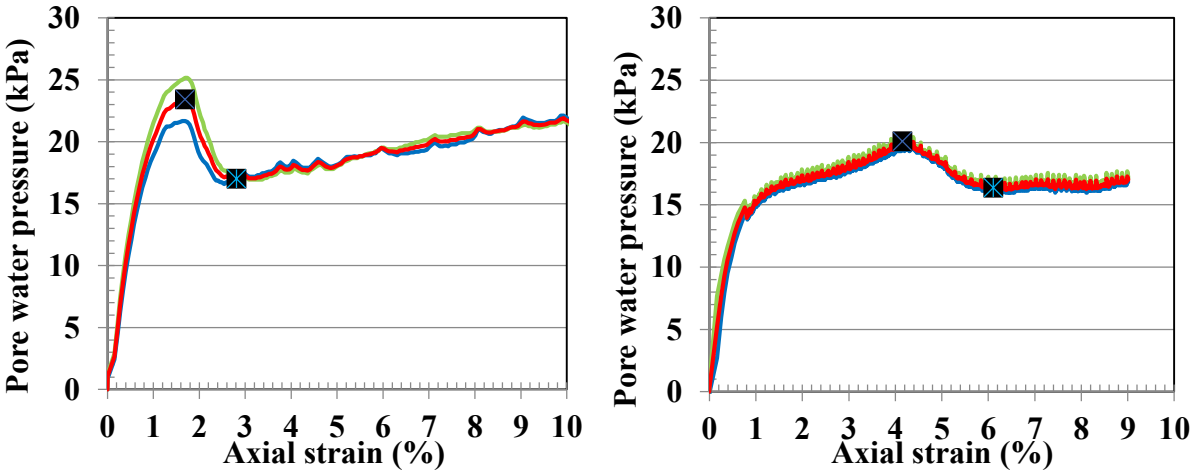

(a) **(b)**

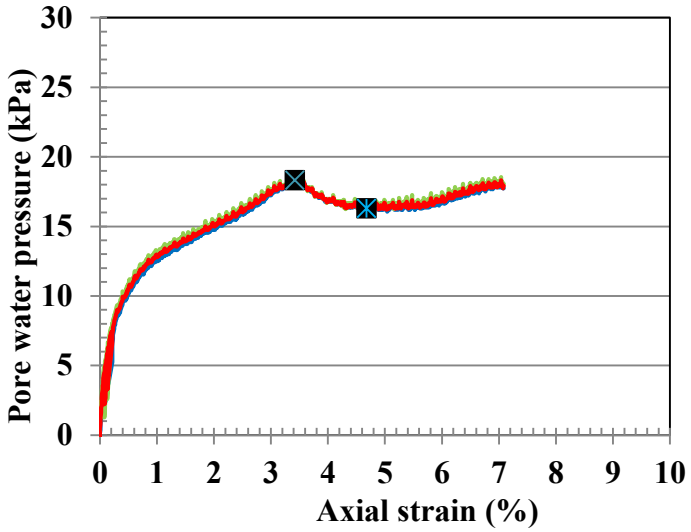

(c)

Figure 4.12 Pore water pressure versus axial strain for (a) Test #1, (b) Test #3, and (c) Test #6

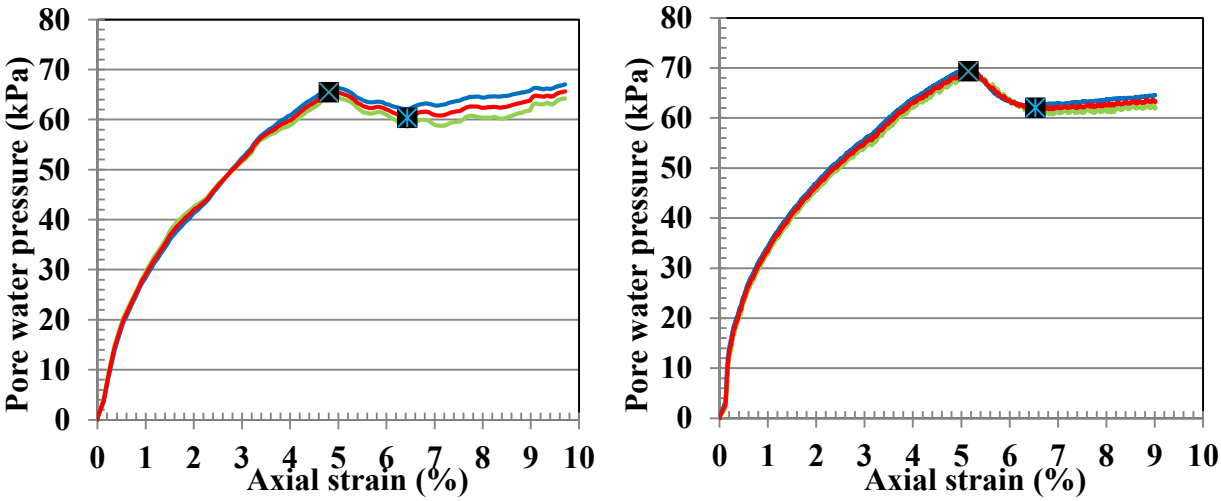

(d)

(e)

Figure 4.13 Pore water pressure versus axial strain for (d) Test #4 and (e) Test #5

4.1.4 Stress Ratio

Stress ratio (q/p') was calculated and plotted versus axial strain with maximum and minimum values of the stress ratio ($Max\ q/p'$ and $Min\ q/p'$), as shown in Figure 4.14 and Figure 4.15. Mean effective stress (p') is defined as

$$p' = p - U_{ave} = \frac{\sigma_x + \sigma_y + \sigma_z}{3} - U_{ave} \qquad \textbf{Equation 4.1}$$

A summarized plot of stress ratio versus axial strain, including all tests, are shown in Figure 4.16. Heavily overconsolidated samples and lightly overconsolidated samples are shown in Figure 4.17 and Figure 4.18, respectively.

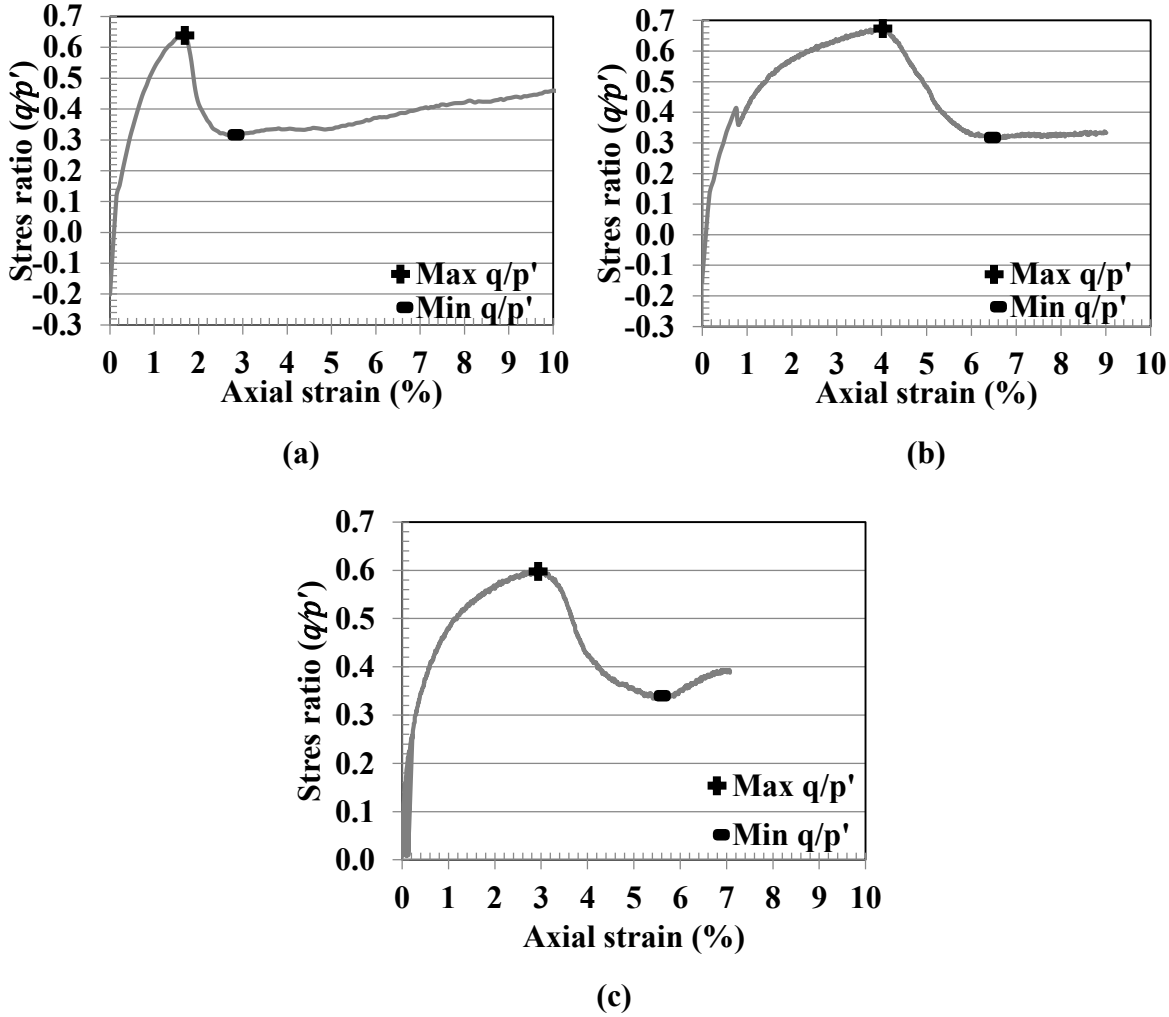

Figure 4.14 Shear stress ratio versus axial strain for (a) Test #1, (b) Test #3, and (c) Test #6

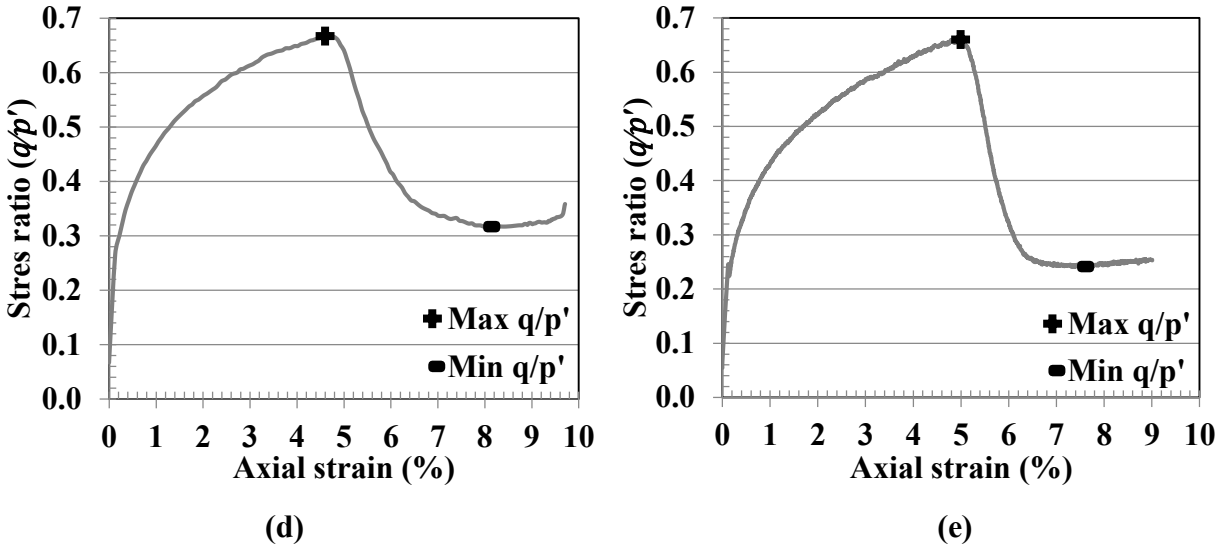

Figure 4.15 Shear stress ratio versus axial strain for (d) Test #4 and (e) Test #5

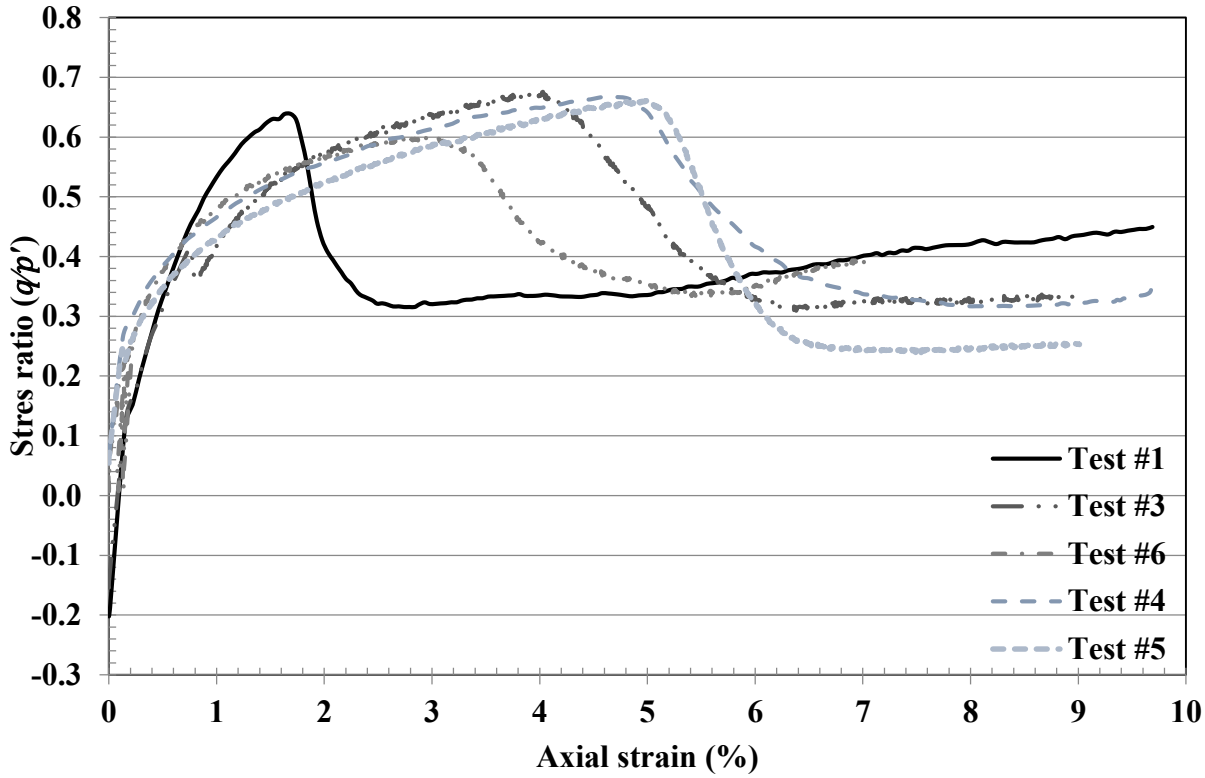

Figure 4.16 Shear stress ratio versus axial strain for all tests

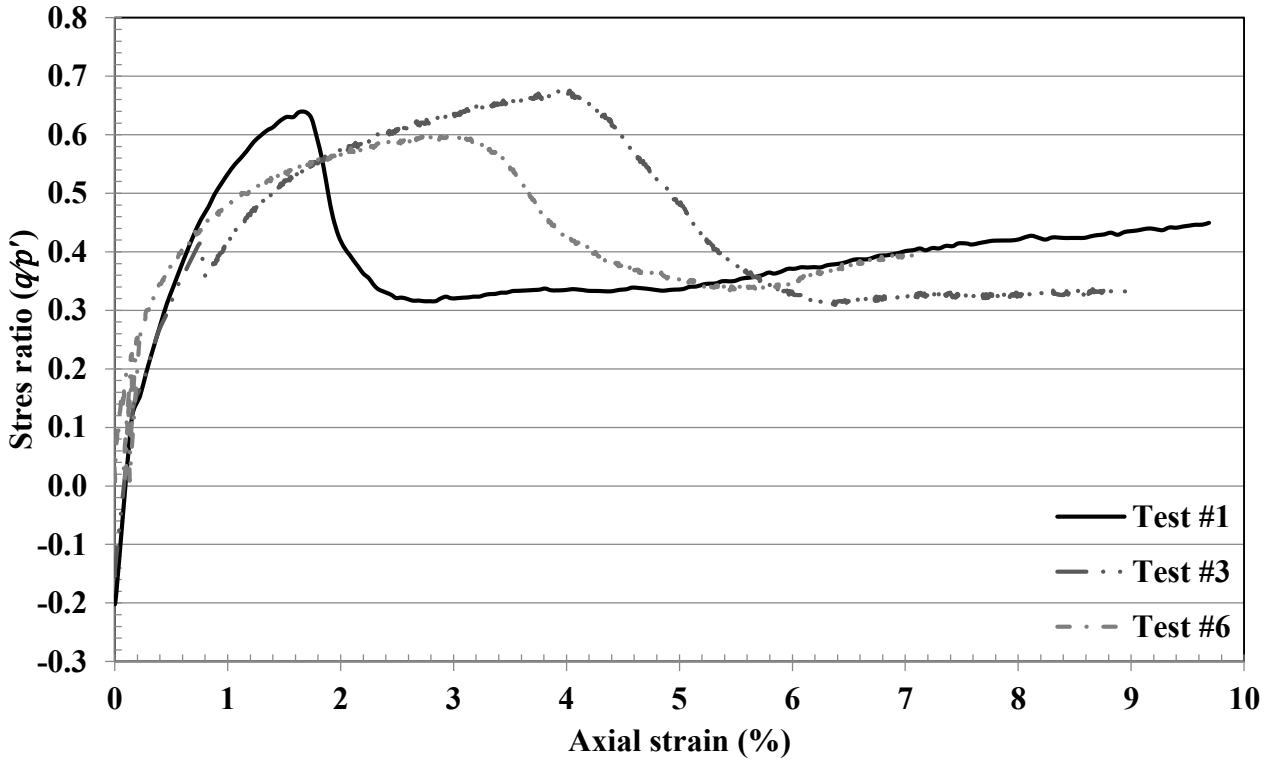

Figure 4.17 Shear stress ratio versus axial strain (Tests #1, #3, and #5)

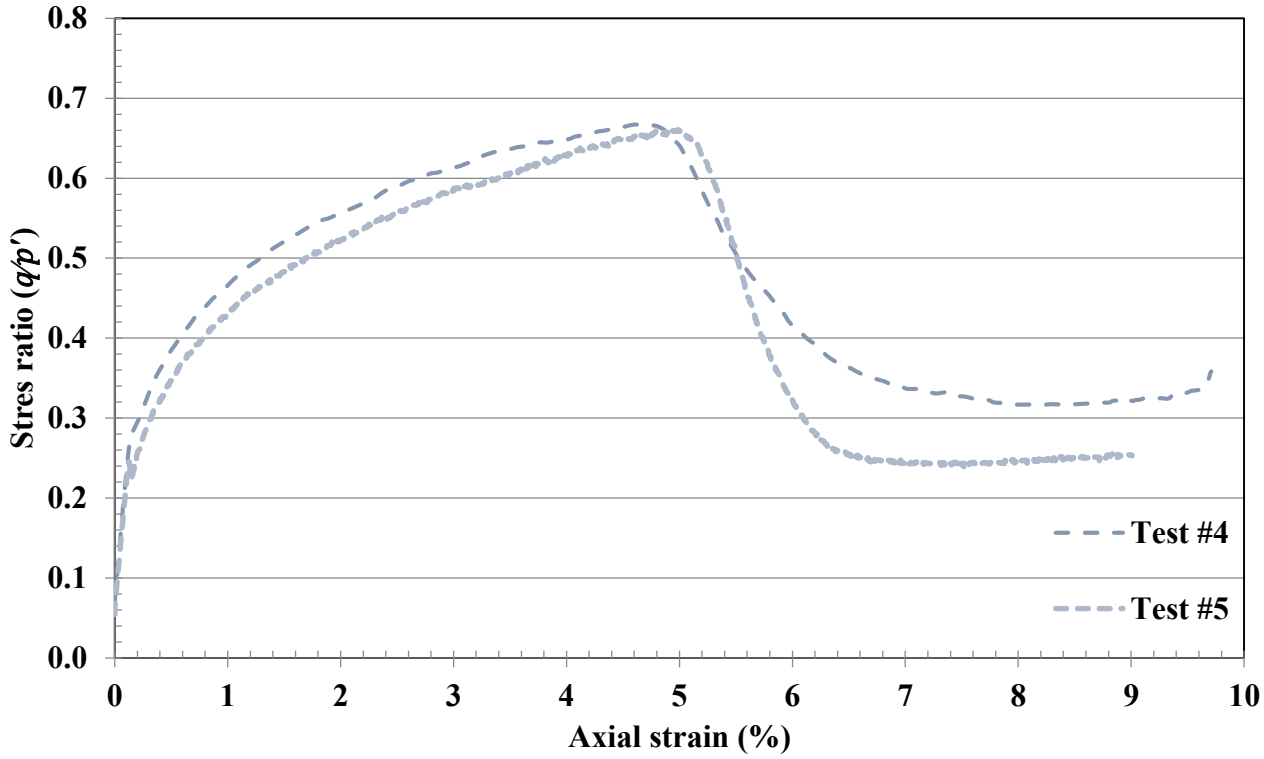

Figure 4.18 Shear stress ratio versus axial strain (Test #4 and #5)

Table 4.1 lists the eight events described in Section 4.1 and corresponding values of axial strain for all tests.

Table 4.1 Axial strain levels corresponding to eight events

Axial strain / Event	ε_a (%)				
	Test #1	**Test #3**	**Test #6**	**Test #4**	**Test #5**
	PS-57F	**PS-55F/S**	**PS-61S**	**PS-139F**	**PS-139S**
O	1.55	3.56	2.40	2.66	3.60
Max q	1.63	3.86	2.79	4.08	4.79
Max q/p'	1.63	4.03	2.94	4.60	4.99
Max u_{ave}	1.69	4.15	3.42	4.80	5.15
E	2.74	4.31	3.59	5.19	5.31
Min u_{ave}	2.81	6.11	4.68	6.43	6.53
Min q/ p'	2.74	6.38	5.52	8.05	7.52
Min q	2.84	6.38	5.59	9.08	7.52

4.1.5 Friction, Tilting, and Eccentricity

Friction between the side walls and the clay specimen was determined by comparing load measurements recorded by the top and bottom load cells. Tilting of the top platen and vertical force eccentricity of the loading shaft were also recorded. Figure 4.19 shows plots for Test #4, including friction, tilting, and eccentricity versus axial strain. Corresponding plots for the other tests are shown in Appendix B . A detailed discussion of the effects of friction, tilting, and eccentricity on onset of strain localization for all tests are provided in Section 4.2.4 Onset of Strain Localization.

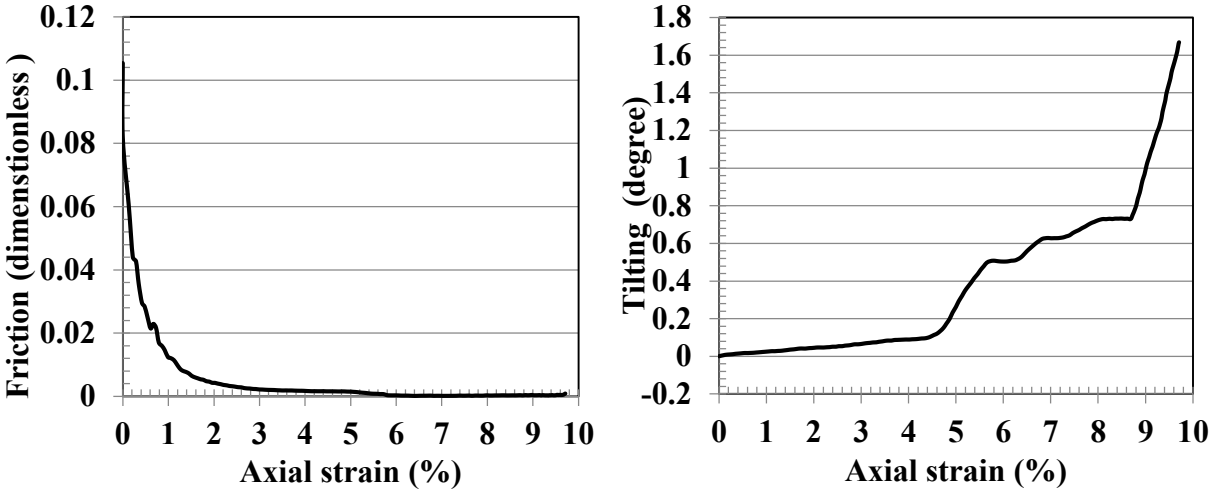

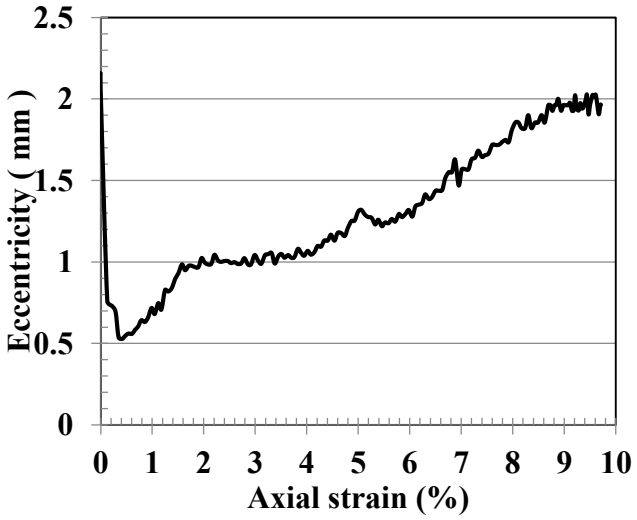

Figure 4.19 (a) Friction, (b) tilting, and (c) eccentricity (Test #4)

4.1.6 Photographs of Shear Band

As mentioned, in this study a grid consisting of vertical and horizontal lines was preprinted on the membrane of each specimen, except for specimen in Test #6, in order to help determine shear band location, orientation, and thickness. However, the printed grid was useful only at a late stage of each test after a shear band became clearly visible. In addition, grid node displacements were not necessarily equal to displacements of the clay specimen. Figure 4.20 shows deformed biaxial specimens at indicated axial strain levels.

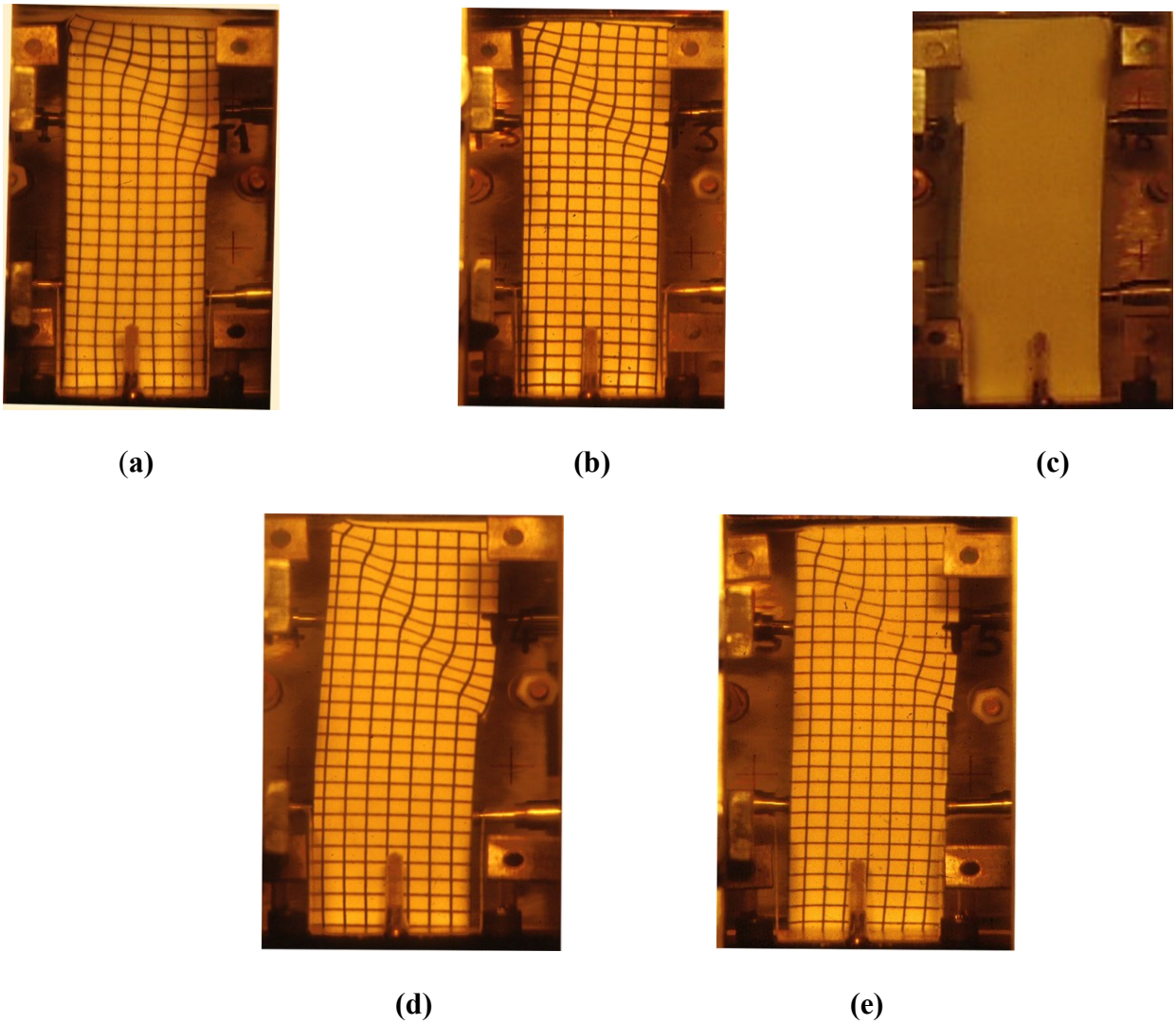

(a) **(b)** **(c)**

(d) **(e)**

Figure 4.20 Biaxial clay specimens at late stages of (a) Test #1: $\varepsilon_a = 2\%$, (b) Test #3: $\varepsilon_a = 6.5\%$, (c) Test #6: $\varepsilon_a = 6\%$, (d) Test #4: $\varepsilon_a = 6\%$, and (e) Test #5: $\varepsilon_a = 8\%$ [26]

4.2 Discussion

This section includes further discussion of biaxial test results, including a summary of compression and shear behaviors, as well as stress paths in deviatoric plane. This section also details development of strain localization, including propagation and evolution phases, and highlights eight events that occurred during the biaxial test.

4.2.1 Compression and Shear Behaviors

Figure 4.21 through Figure 4.25 depict deviatoric and volumetric responses for heavily overconsolidated samples (Tests #1, #3, and #6) and lightly overconsolidated samples (Tests #4 and #5). The eight events (O, $Max\ q$, $Max\ q/p'$, $Max\ u_{ave}$, E, $Min\ U_{ave}$, $Min\ q/p'$, and $Min\ q$) are labeled on the response curves. Corresponding axial strain levels, values of stress tensor invariants (q, p', p^*, θ), and average PWP are listed in Table 4.2 through Table 4.6 for all tests. A modified total mean stress (p^*) is defined as

$$p^* = p - U_o \qquad \textbf{Equation 4.2}$$

where U_o is the PWP at the beginning of the undrained shear stage. Coupled deviatoric and volumetric-shear behaviors is depicted in Figure 4.26 for all tests.

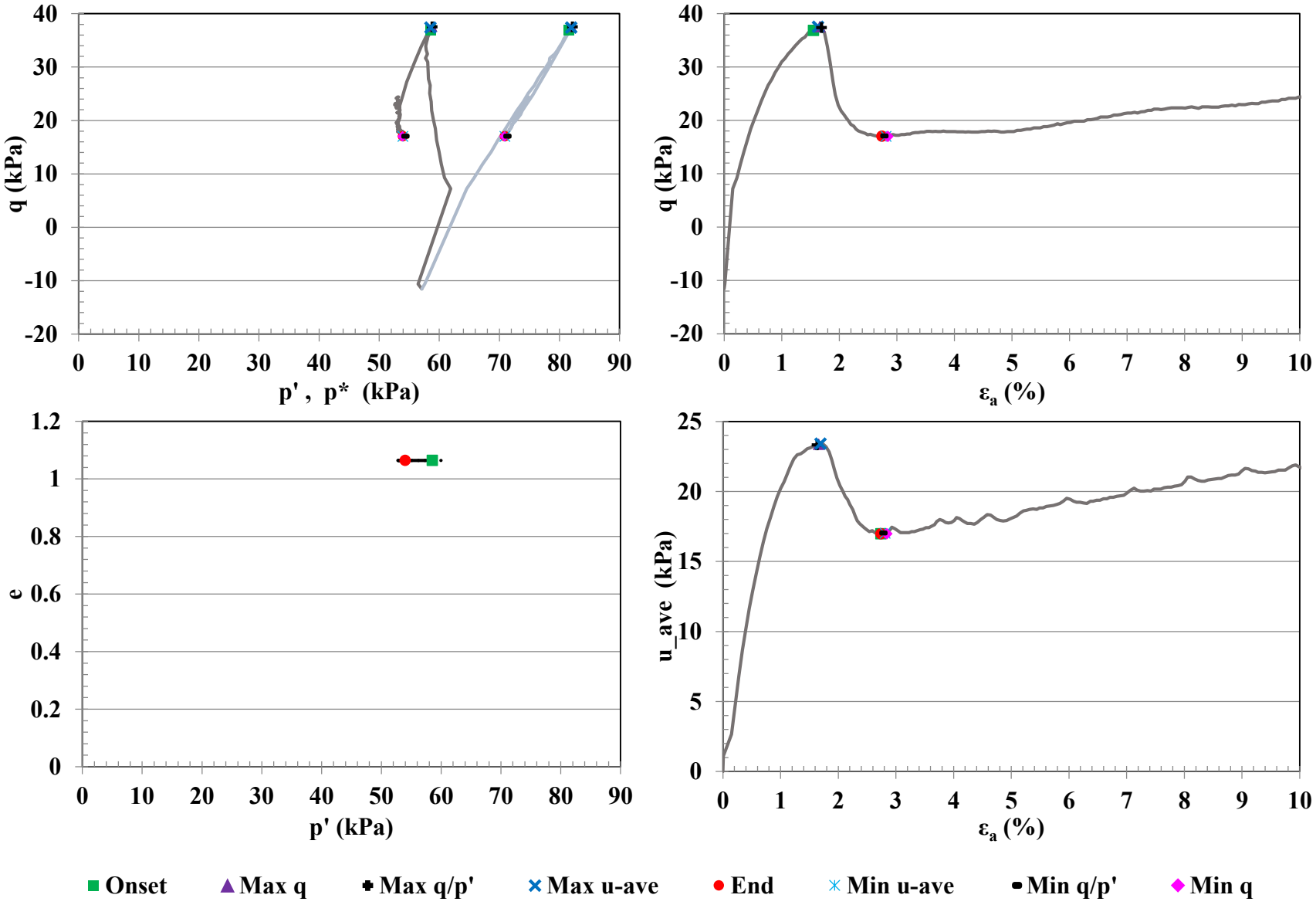

Figure 4.21 Deviatoric and volumetric responses for Test #1

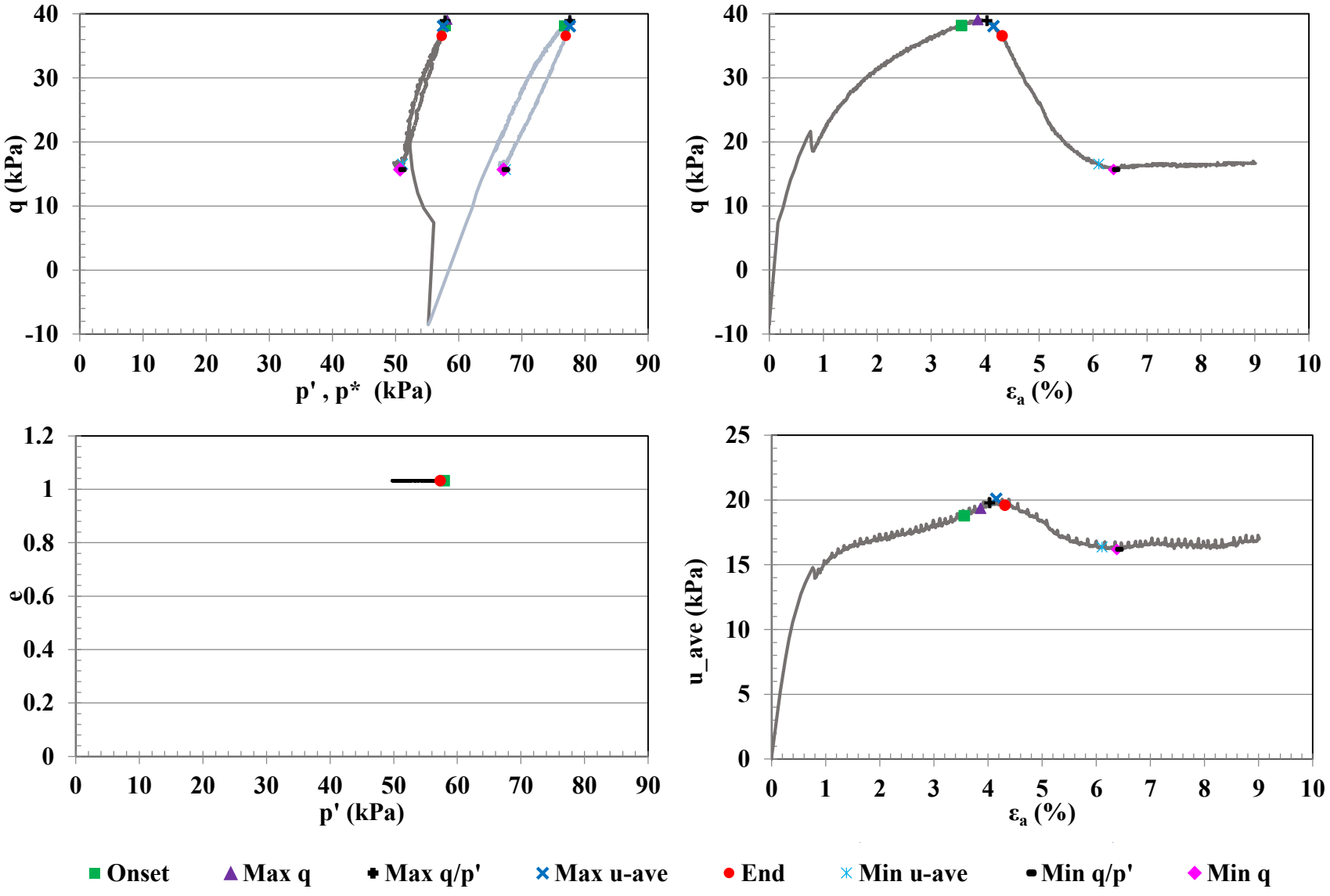

Figure 4.22 Deviatoric and volumetric responses for Test #3

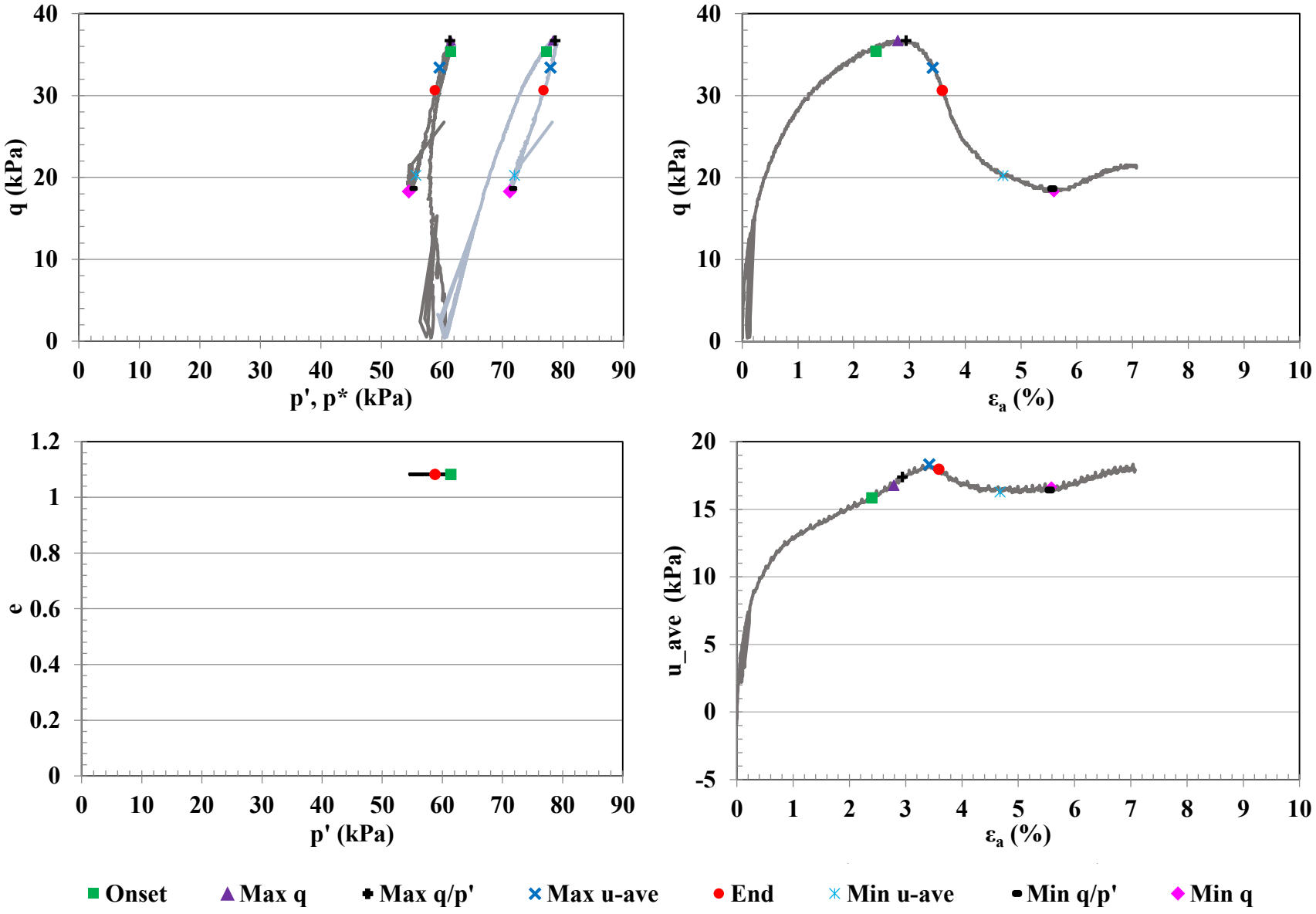

Figure 4.23 Deviatoric and volumetric responses for Test #6

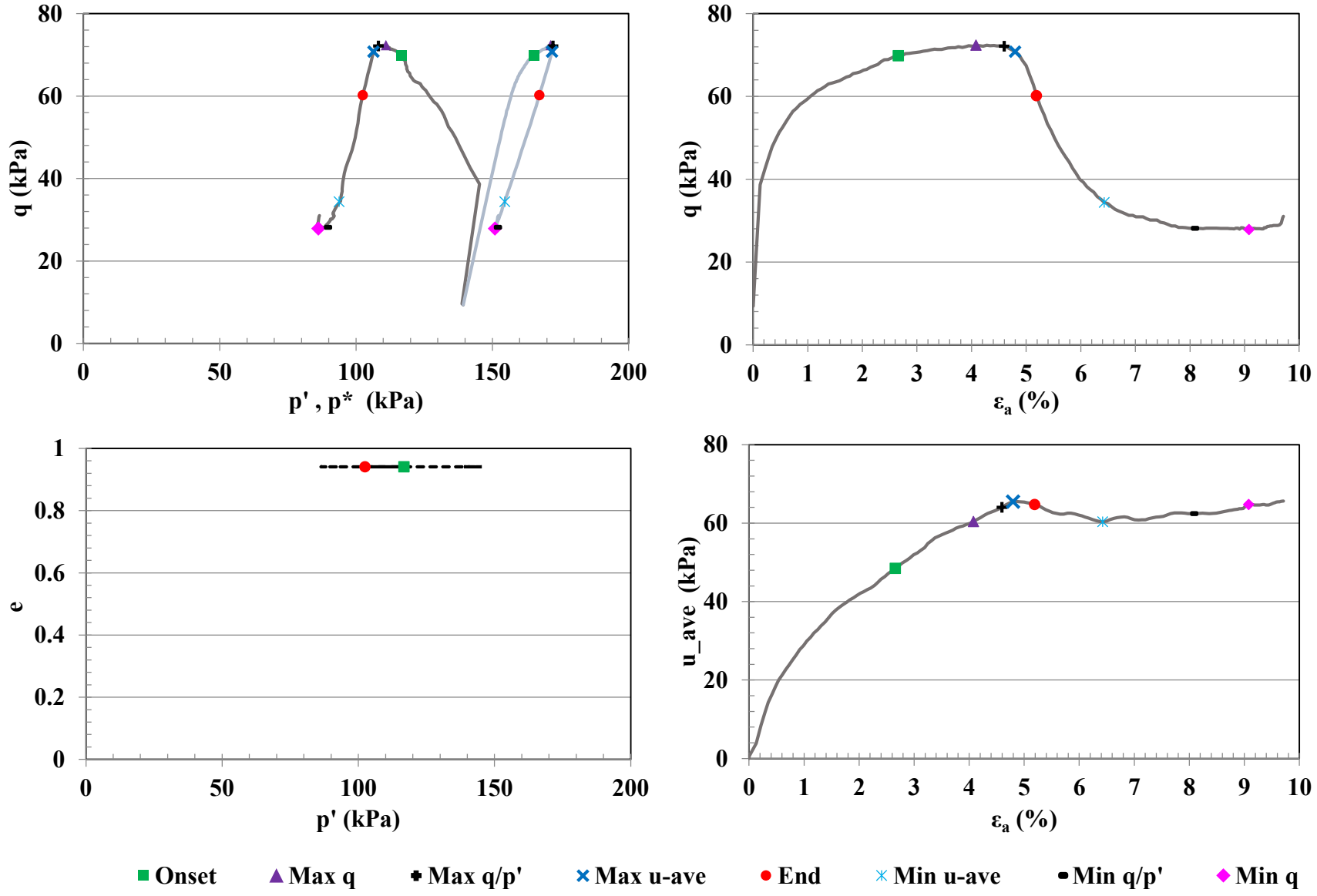

Figure 4.24 Deviatoric and volumetric responses for Test #4

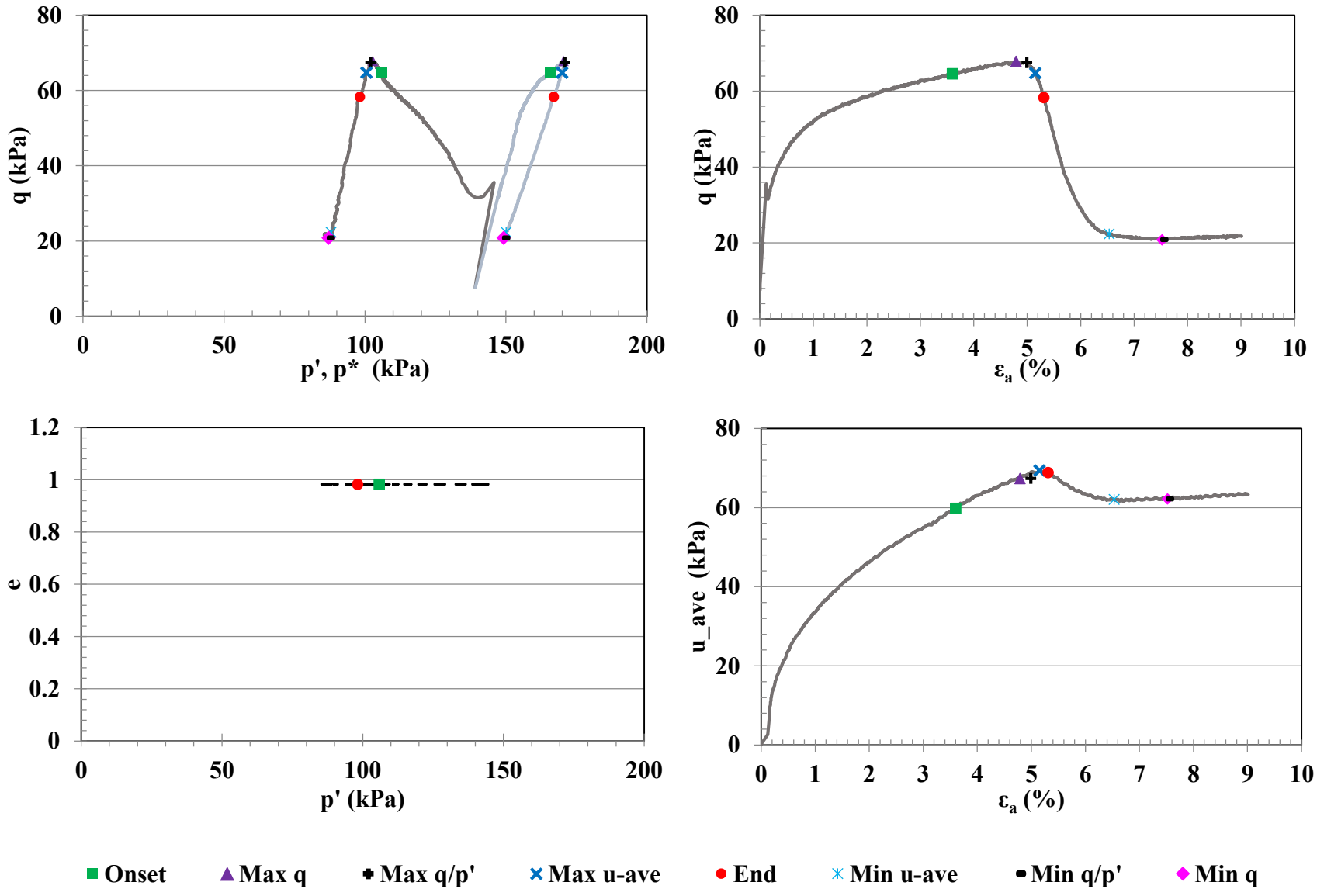

Figure 4.25 Deviatoric and volumetric responses for Test #5

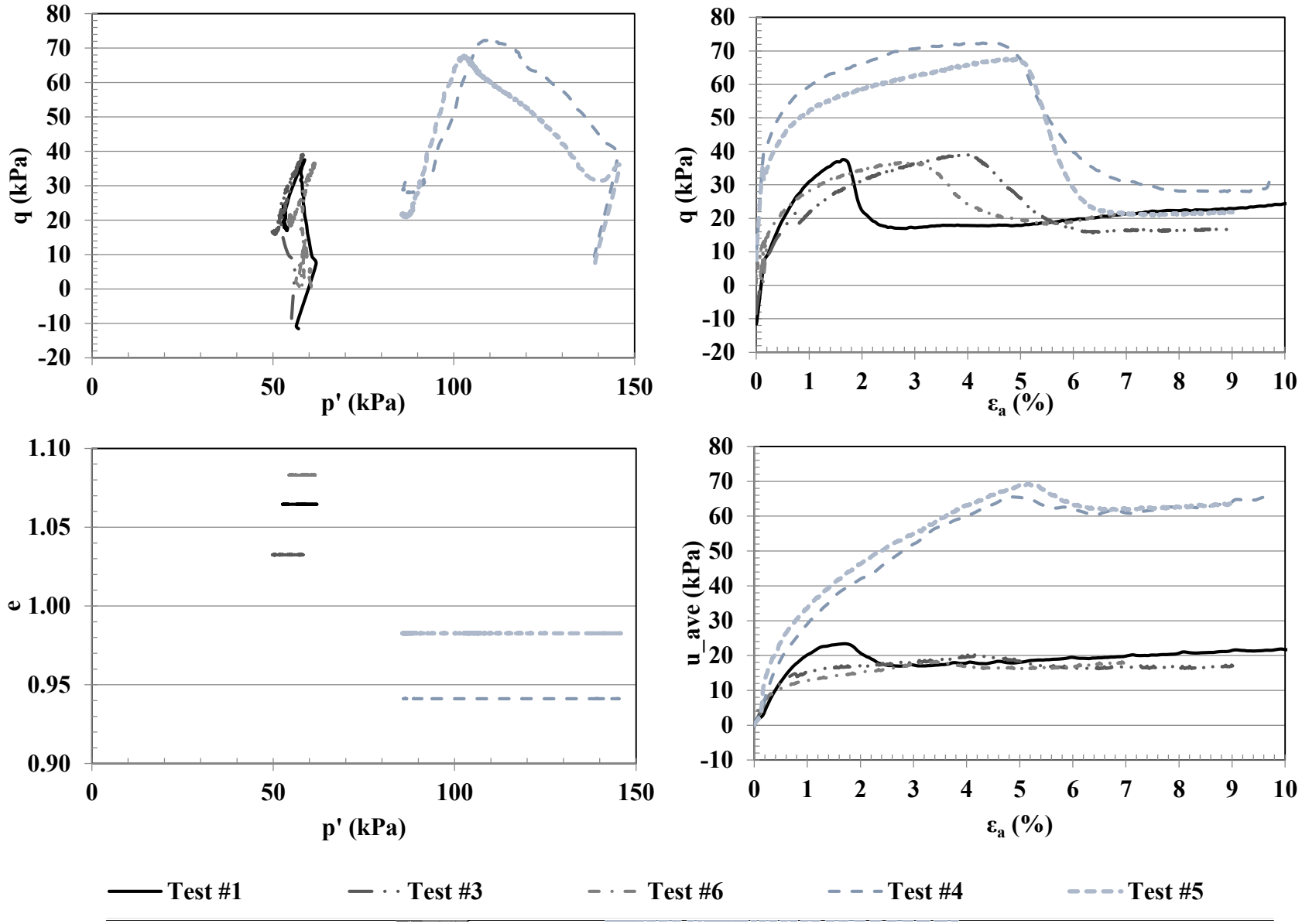

Figure 4.26 Deviatoric and volumetric responses for all tests

Table 4.2 Summary of the eight events for Test #1

Test #1	ε_a	q	p'	p^*	u_{ave}	θ
PS-57F	%	kPa	kPa	kPa	kPa	Degree
O	1.55	36.89	58.53	81.58	23.09	33.21
Max q	1.66	37.55	58.83	82.04	23.37	33.25
Max q/p'	1.63	37.55	58.80	82.14	23.34	33.12
Max u_{ave}	1.69	37.38	58.54	81.95	23.41	33.38
E	2.74	17.06	53.95	70.93	16.98	52.86
Min u_{ave}	2.81	17.01	53.95	70.92	17.02	52.85
Min q/p'	2.74	17.06	53.95	70.92	17.02	52.86
Min q	2.84	17.00	53.87	70.85	16.98	52.84

Table 4.3 Summary of the eight events for Test #3

Test #3	ε_a	q	p'	p^*	u_{ave}	θ
PS-55F/S	%	kPa	kPa	kPa	kPa	Degree
O	3.56	38.17	57.93	76.72	18.80	17.19
Max q	3.86	39.11	58.23	77.60	19.37	18.45
Max q/p'	4.03	38.95	57.82	77.61	19.79	19.21
Max u_{ave}	4.15	38.09	57.51	77.60	20.09	19.92
E	4.31	36.57	57.32	76.92	19.61	20.65
Min u_{ave}	6.11	16.55	51.10	67.44	16.37	26.19
Min q/p'	6.38	15.68	50.71	67.08	16.19	26.27
Min q	6.38	15.68	50.71	67.08	16.19	26.27

Table 4.4 Summary of the eight events for Test #6

Test #6	ε_a	q	p'	p^*	u_{ave}	θ
PS-61S	%	kPa	kPa	kPa	kPa	Degree
O	2.40	35.39	61.41	77.25	15.84	8.48
Max q	2.79	36.73	61.51	78.30	16.79	16.92
Max q/p'	2.94	36.72	61.31	78.71	17.40	18.71
Max u_{ave}	3.42	33.41	59.60	77.92	18.32	19.32
E	3.59	30.65	58.79	76.75	17.96	20.83
Min u_{ave}	4.68	20.24	55.70	71.99	16.30	23.55
Min q/p'	5.52	18.64	54.92	71.34	16.43	23.59
Min q	5.59	18.28	54.53	71.19	16.66	23.18

Table 4.5 Summary of the eight events for Test #4

Test #4	ε_a	q	p'	p^*	u_{ave}	θ
PS-139F	%	kPa	kPa	kPa	kPa	Degree
O	2.66	69.84	116.74	165.23	48.49	10.64
Max q	4.08	72.37	110.96	171.42	60.47	17.54
Max q/p'	4.60	72.16	108.18	172.26	64.08	17.54
Max u_{ave}	4.80	70.80	106.42	171.90	65.49	18.21
E	5.19	60.20	102.46	167.22	64.77	19.14
Min u_{ave}	6.43	34.41	93.77	154.61	60.36	24.85
Min q/p'	8.05	28.14	88.82	151.21	62.39	24.11
Min q	9.08	27.85	86.21	150.97	64.77	24.11

Table 4.6 Summary of the eight events for Test #5

Test #5	ε_a	q	p'	p^*	u_{ave}	θ
PS-139S	%	kPa	kPa	kPa	kPa	Degree
O	3.60	64.58	105.89	165.71	59.82	14.45
Max q	4.79	67.86	102.81	170.43	67.34	16.97
Max q/p'	4.99	67.48	102.03	170.87	67.37	17.80
Max u_{ave}	5.15	64.75	100.56	169.92	69.36	20.82
E	5.31	58.30	98.18	166.99	68.82	22.11
Min u_{ave}	6.53	22.36	87.99	150.07	62.08	27.39
Min q/p'	7.52	20.82	87.06	149.22	62.17	29.10
Min q	7.52	20.82	87.06	149.22	62.17	29.11

4.2.2 Stress Path in Deviatoric Plane

Figure 4.27 and Figure 4.28 depict stress paths for all tests in a deviatoric plane, utilizing the Haigh-Westergaard coordinate system (ρ ,θ). A radial distance (ρ) is defined as

$$\rho = \sqrt{\frac{2}{3}}\, q \qquad \textbf{Equation 4.3}$$

Figure 4.27 and Figure 4.28 also indicate stress state during initial homogenous deformation of the specimens, which corresponds to CTC (θ =0°) in Tests #4, #5 and #6. The stress state during initial homogenous deformation of specimens in Tests #1 and #3 also corresponds to approximately

constant Lode's angles; however, in Tests #1 and #3 it differed from zero. The onset of strain localization occurred shortly after the departure of Lode's angles from their initial constant value.

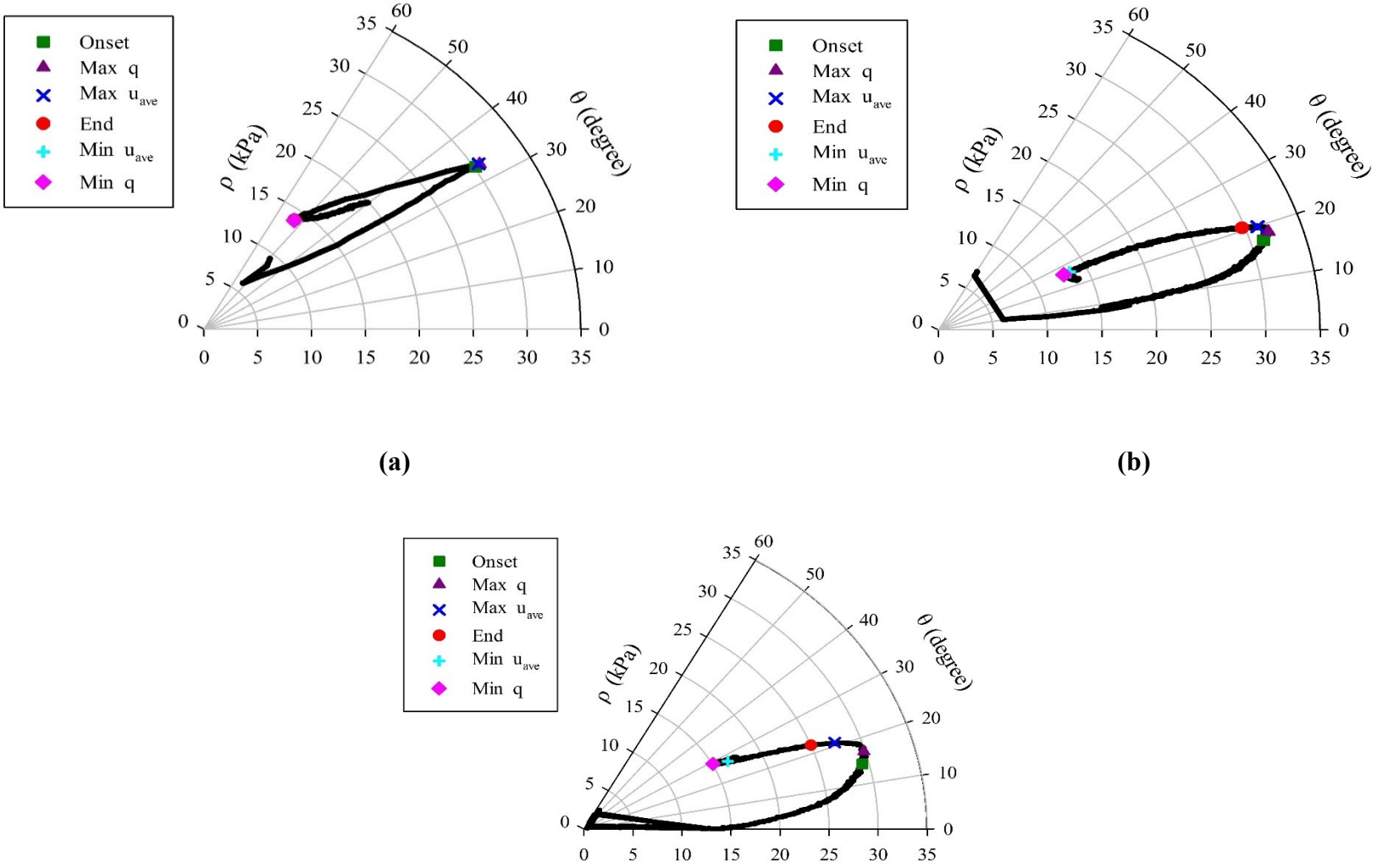

(a) **(b)**

(c)

Figure 4.27 Stress path with eight events for (a) Test #1, (b) Test #3, and (c) Test #6

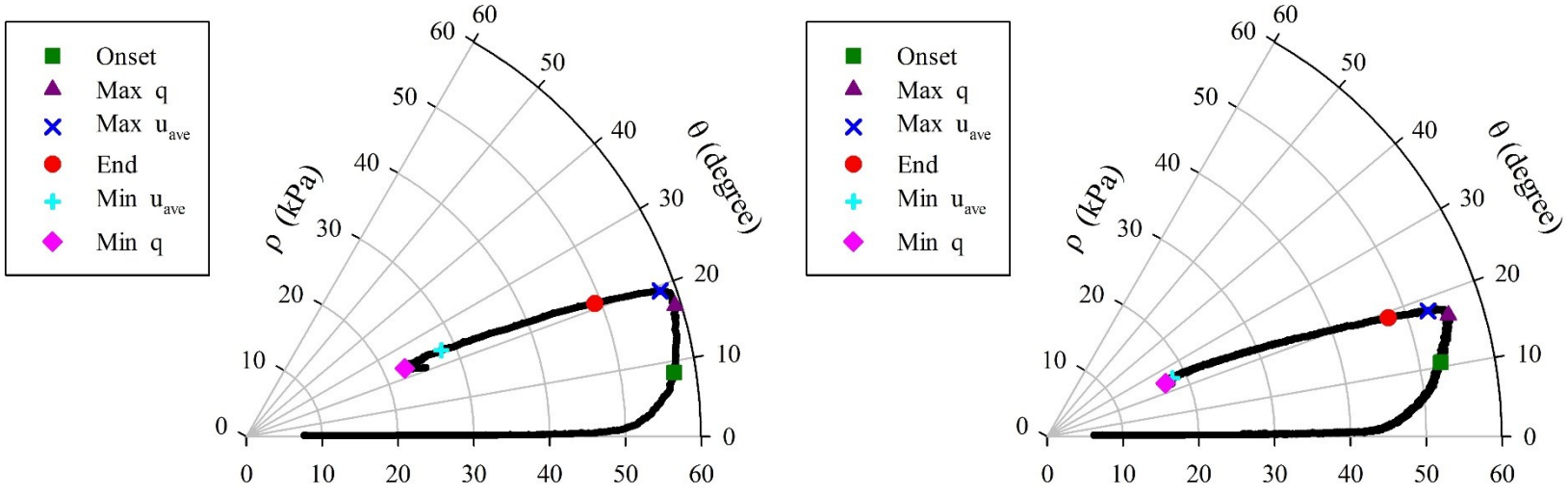

(d) **(e)**

Figure 4.28 Stress path with eight various for (d) Test #4 and (e) Test #5

4.2.3 Development of Strain Localization

Although the inception of strain localization occurred relatively early, shear bands became visible to the naked eye at late stages of the tests. Four crosshairs were permanently marked on the transparent side walls, thus providing the scale to determine the shear band inclination angle (θ_B). The horizontal shear band inclination angle was measured using photographs from AutoCAD. These angles and corresponding axial strain levels are provided in Table 4.7. Thickness of the shear band at the end of the propagation stage (t_E) based on the corresponding top and bottom width difference of the specimens (Figure 4.5 and Figure 4.6) is listed in Table 4.7.

Table 4.7 Inclination angle and thickness of shear band

Test number	ε_a	θ_B	t_E[1]
	%	degree	mm
Test #1	2	50.41	1.28
	3	51.00	
Test #3	6.29	52.66	0.33
	6.50	53.64	
Test #4	7	58.05	1.01
	8	57.17	
Test #5	6	54.90	0.72
	7	55.01	

[1] t_E was determined at the end of propagation stage

4.2.4 Onset of Strain Localization

The onset of strain localization indicates that the clay specimen reached the end of a homogenous deformation stage coinciding with the beginning of shear band formation. Several factors have proven to affect strain localization. Andrade and Borja [29] showed that inhomogeneity in the form of unstructured random density affects the onset of strain localization in sand. Drescher and Vardoulakis [30] showed that a combination of height-to-diameter ratio and boundary friction also affect the inception of strain localization. Marachi et al. [24] , Peters et al.

[3], and Perić et al. [13] showed that the plane strain state is far more susceptible to strain localization than the axisymmetric state of stress.

In order to further elucidate factors that may affect the onset of strain localization, the current study ranked friction, tilting, and vertical force eccentricity based on measurements during each test. A coefficient of friction between the sample and side walls was obtained based on measurements from the top and bottom axial loading cells and side wall load cells. The axial strain level corresponding to the onset of strain localization was the smallest in Test #1, followed by Tests #6, #4, #3, and #5 (Table 4.1). Furthermore, the inception of strain localization occurred at the smallest axial strain value in the fast test on heavily overconsolidated sample. The largest axial strain level at the onset of strain localization was registered in the slow test on lightly overconsolidated sample.

An eccentricity of axial force was obtained based on measurement comparisons of the bottom axial load cells. Tilting of the top platen was determined based on two axial LVDT measurements. Based on the plots of coefficients of friction, tilting, and eccentricity versus axial strain (Figure 4.19 and Appendix B), Figure 4.29 shows the magnitudes of friction, tilting, and eccentricity at the onset of strain localization, as well as their maximum values.

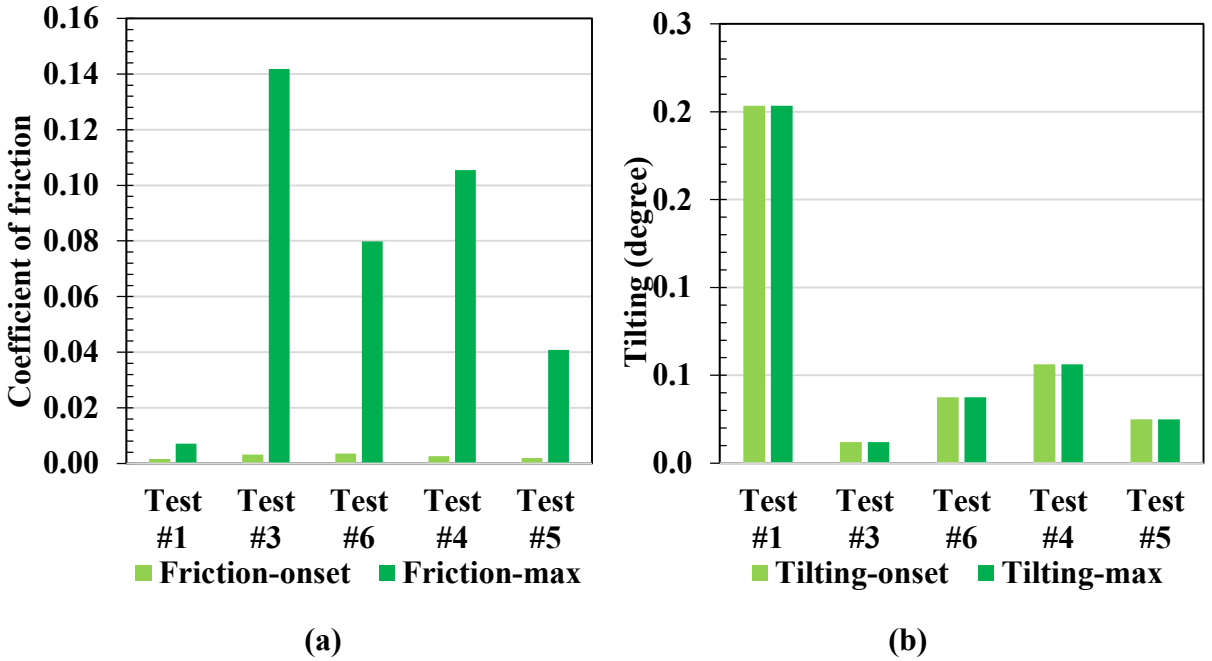

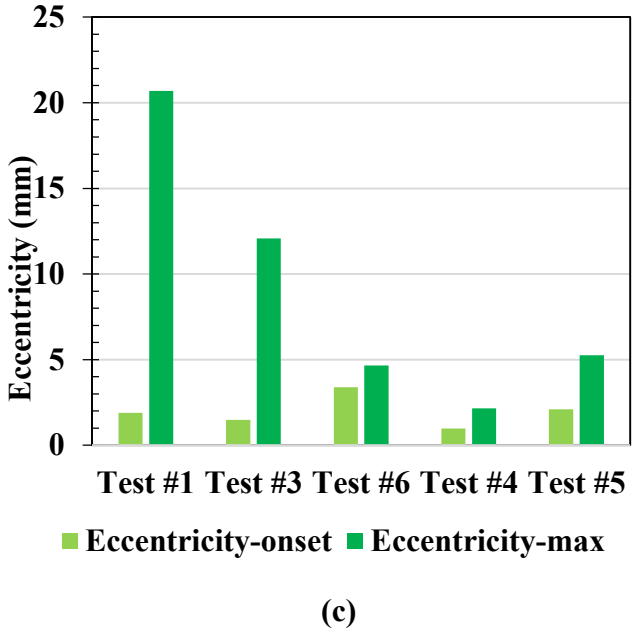

Figure 4.29 Onset and maximum values of (a) friction, (b) tilting, and (c) eccentricity

Friction, tilting, and eccentricity were ranked based on Figure 4.29. The larger the value of friction, tilting or eccentricity, the smaller the rank it received. The resulting overall rank was based on the summation of the three effects, ranging from smaller to larger values. Overall rankings

correspond to the actual onset of strain localization are listed in the right-hand columns of Table 4.8 through Table 4.10. The strongest correlation between the predicted and actual onset of strain localization was obtained based on maximum values of friction, tilting, and eccentricity shown in Table 4.9. In summary, the maximum values of friction, tilting, and eccentricity may cause earlier inception of strain localization. However, the effects of sample inhomogeneity could not be evaluated in this study.

Table 4.8 Friction, tilting, and eccentricity rank at onset

Test number	Friction, tilting and eccentricity at onset					ε_a	
	Friction Rank	Tilting Rank	Eccentricity Rank	Sum	Overall rank	%	Rank
Test #1	5	1	3	9	2	1.55	1
Test #3	2	5	4	11	**4**	3.56	**4**
Test #6	1	3	1	5	1	2.40	2
Test #4	3	2	5	10	**3**	2.66	**3**
Test #5	4	4	2	10	3	3.60	5

Table 4.9 Maximum values of friction, tilting, and eccentricity rank

Test number	Maximum value rank					ε_a	
	Friction Rank	Tilting Rank	Eccentricity Rank	Sum	Overall rank	%	Rank
Test #1	5	1	1	7	**1**	1.55	**1**
Test #3	1	5	2	8	2	3.56	4
Test #6	3	3	4	10	4	2.40	2
Test #4	2	2	5	9	**3**	2.66	**3**
Test #5	4	4	3	11	**5**	3.60	**5**

Table 4.10 Combination of overall effects and axial strain level rank

	Onset value rank		Maximum value rank		Overall[1] value rank		ε_a
	Sum	Rank	Sum	Rank	Overall[1] sum	Rank	Rank
Test #1	9	2	7	1	16	2	1
Test #3	11	3	8	2	19	3	4
Test #6	5	1	10	4	15	1	2
Test #4	10	4	9	3	19	**3**	**3**
Test #5	10	4	11	5	21	4	5

[1] The overall sum was determined by adding the onset value sum and maximum value sum.

4.2.5 Homogeneous Deformation, Propagation, and Evolution of Strain Localization

Based on internal measurements of lateral displacement, sled displacement, and axial strain, three distinct phases were identified for each test in this study. These phases, as shown in Figure 4.30 for Test #3, were (1) homogeneous deformation, (2) the propagation of strain localization, and (3) the evolution of strain localization. In all tests specimens deformed homogeneously during phase I, as indicated in Figure 4.5 and Figure 4.6, so the beginning of phase II coincided with the onset of strain localization. The end of the propagation phase corresponded to a sudden change in sled velocity in a majority of the tests, as shown in Figure 4.31 and Figure 4.32. During phase II, which corresponded to a propagation of a shear band, a magnitude of the bottom-width increase rate slowed down while a magnitude of the top-width increase rate increased significantly, as shown in Figure 4.31 and Figure 4.32. Although primary shear band propagation occurred across the specimen width, a comparison of top and bottom width changes (Figure 4.5 and Figure 4.6) indicated a small lateral propagation of the shear band during phase II. The end of phase II was determined based by on sled displacement rate and bottom width change. Specifically, a slight decrease in bottom width (Figure 4.5 and Figure 4.6) indicated the beginning of elastic unloading

of the material outside the shear band, which was signified at the commencement of phase III, during which further evolution of shear band occurred.

Elastic unloading began after the shear band propagated across the entire sample. This elastic unloading coincided closely with the sudden change in LVDT sled displacement (Figure 4.3 and Figure 4.4) and specimen width change rate (Figure 4.31 and Figure 4.32). A close correspondence between the beginning of elastic unloading and the sudden change in the sled velocity was found in all tests except for Test #4 (Figure 4.31 and Figure 4.32), thus strongly corroborating the end of shear band propagation. For Test #4, the end of shear band propagation was determined based on the commencement of elastic unloading, which occurred directly before the sled velocity changed. The remaining part of biaxial tests consisted of a phase III during which a large deformation was concentrated inside the shear band, indicating global axial strain due to sliding along the shear band.

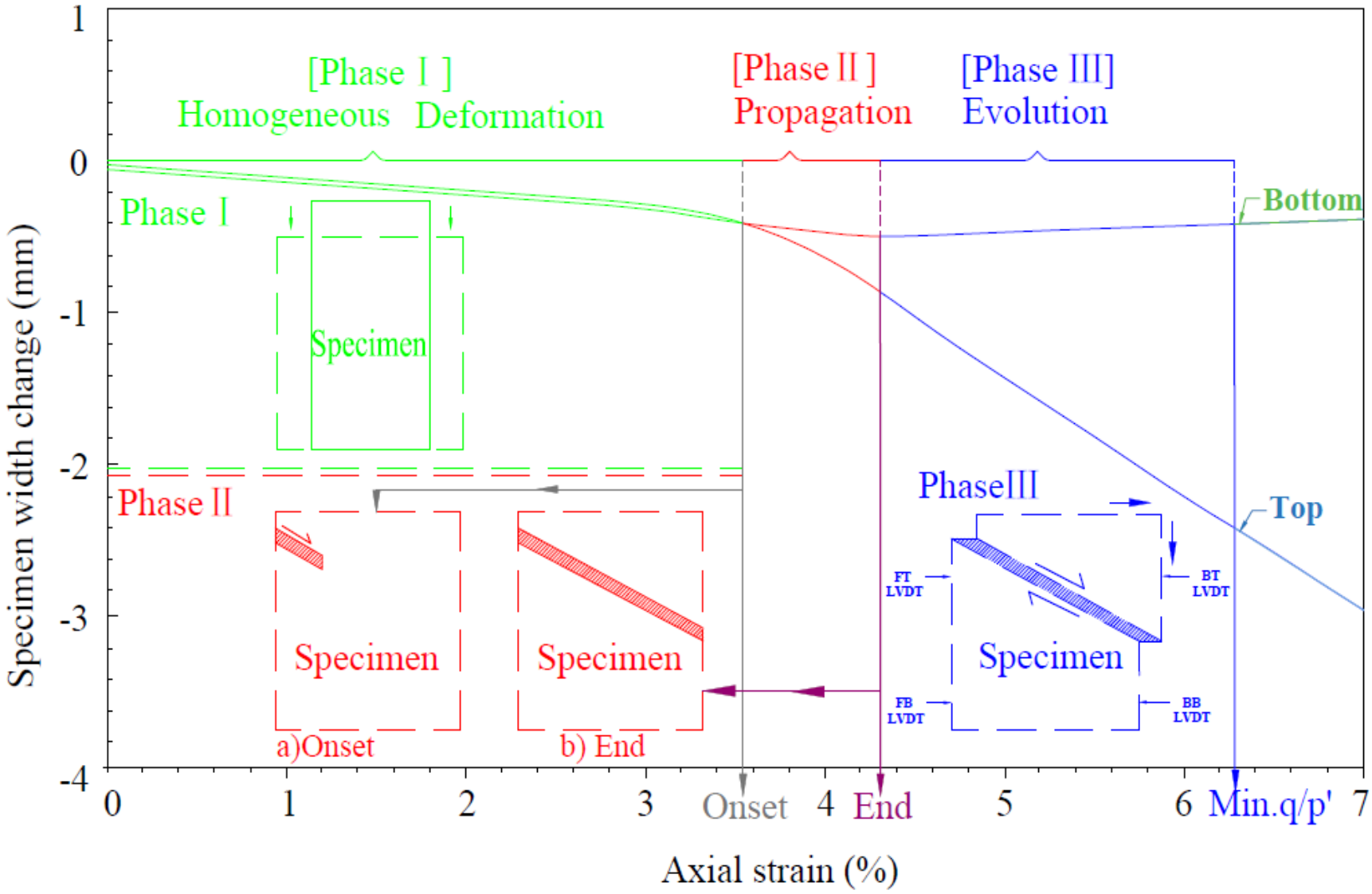

Figure 4.30 Three phases of biaxial test (Test #3)

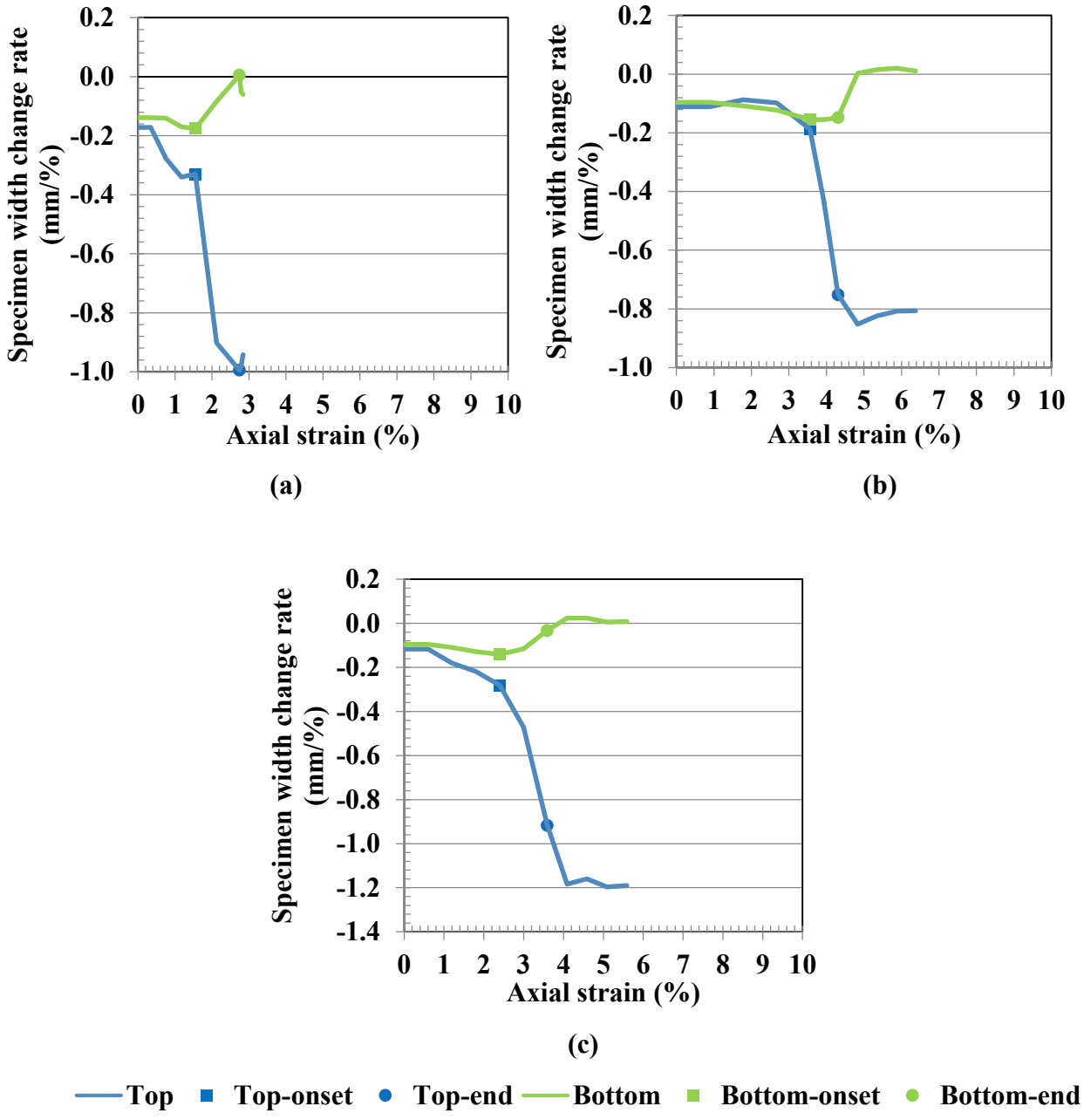

Figure 4.31 Width change rate versus axial strain for (a) Test #1, (b) Test #3, and (c) Test #6

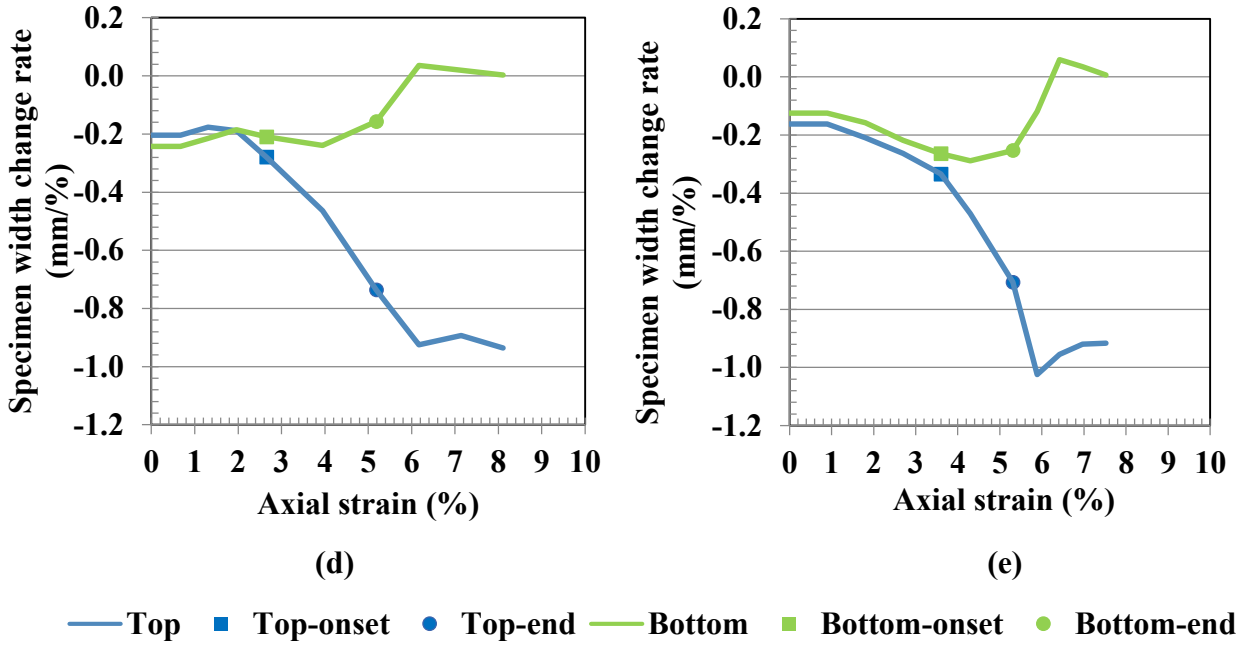

Figure 4.32 Width change rate versus axial strain for (d) Test #4 and (e) Test #5

4.2.5.1 Propagation Phase

Results of laboratory tests carried out on stiff clays [31] and soft clays [12] indicated that strain localization is progressive process, involving the propagation phase that ultimately results in formation of a shear band. Viggiani et al. [31] found that local measurements of horizontal displacements in the biaxial device showed complete formation of a shear band that "came out from the boundaries" well after the onset of strain localization, as confirmed by stereophotogrammetry [32].

4.2.5.2 Evolution Phase

In another study, Viggiani et al. [32] found that a shear band became exposed to specimen boundaries after a post-peak knee point, which corresponds to the beginning of an elastic unloading or end point. This observation was in complete agreement with the findings of the current study because the propagation phase was completed by the end event, and the remaining part of the biaxial test is named the evolution phase. During the evolution phase, strains became increasingly

concentrated within the shear band while the remaining part of the sample unloaded elastically. Therefore, shear and volumetric strains at the level of the shear band were computed based on internal measurements, and the assumption was made that shear band deformed in a simple shear mode, thus remaining inextensible. Corresponding undeformed and deformed configurations are shown in Figure 4.33. A photograph of a clearly visible shear band at the end of Test #5 is shown in Figure 4.34.

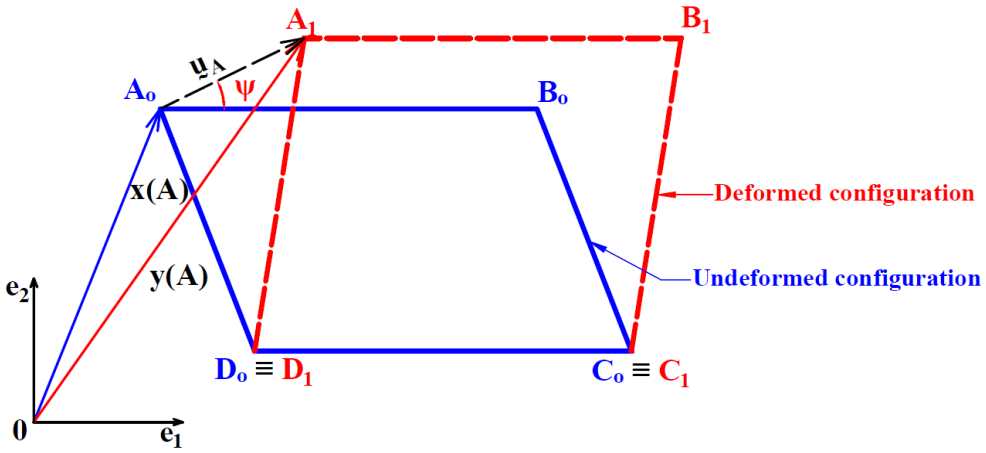

Figure 4.33 Undeformed and deformed shear band configuration

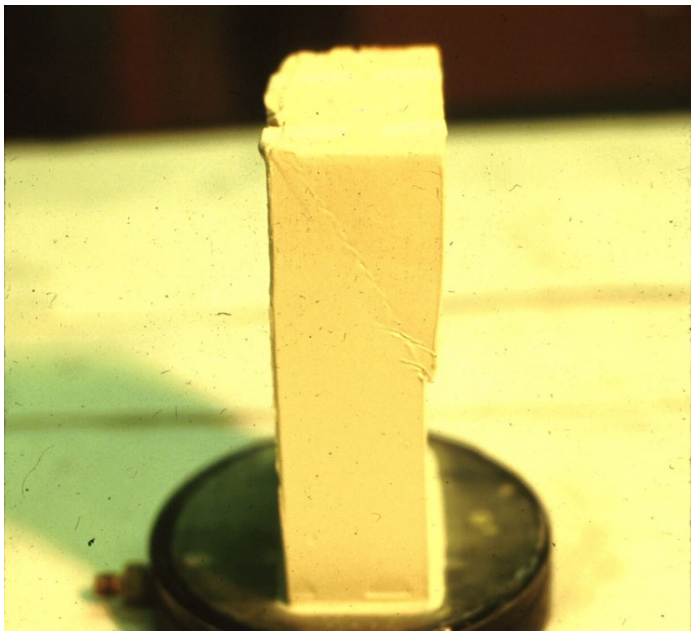

Figure 4.34 Shear band (Test #5) [26]

According to Bower [33], the Lagrange strain tensor is used in calculation in which large shear changes as expected. Its components are given by

$$\varepsilon_{x_1x_1} = \frac{du_1}{dx_1} + \frac{1}{2}\left[\left(\frac{du_1}{dx_1}\right)^2 + \left(\frac{du_2}{dx_1}\right)^2\right] \quad \textbf{Equation 4.4(a)}$$

$$\varepsilon_{x_2x_2} = \frac{du_2}{dx_2} + \frac{1}{2}\left[\left(\frac{du_1}{dx_2}\right)^2 + \left(\frac{du_2}{dx_2}\right)^2\right] \quad \textbf{Equation 4.4(b)}$$

$$\varepsilon_{x_1x_2} = \frac{1}{2}\left[\frac{du_2}{dx_1} + \frac{du_1}{dx_2} + \left(\frac{du_1}{dx_1}\right)\left(\frac{du_1}{dx_2}\right) + \left(\frac{du_2}{dx_1}\right)\left(\frac{du_2}{dx_2}\right)\right], \quad \textbf{Equation 4.4(c)}$$

where $\varepsilon_{x_1x_1}$ and $\varepsilon_{x_2x_2}$ are normal strains and $\varepsilon_{x_1x_2}$ is shear strain at the level of the shear band. Moreover, the magnitude of displacement vector (u) at any time (t) and any point is given by

$$u(t) = \frac{u_A(t)}{t_E}(x_2(t) - x_{2D}) \quad \textbf{Equation 4.5(a)}$$

$$u_1(t) = \frac{u_A(t)}{t_E}\,(x_2(t) - x_{2D})\cos\Psi(\mathrm{t}) \quad \textbf{Equation 4.5(b)}$$

$$u_2(t) = \frac{u_A(t)}{t_E}\,(x_2(t) - x_{2D})\sin\Psi(\mathrm{t}) \quad \textbf{Equation 4.5(c)}$$

where t_E is thickness of the shear band at the end of the propagation stage. Combining Equation 4.4 (a) with Equations 4.5 (b) and (c) results in $\varepsilon_{x_1x_1}$ equal to 0. Combining Equation 4.4 (b) with Equations 4.5 (b) and (c) results in $\varepsilon_{x_2x_2}$, as follows

$$\varepsilon_{x_2x_2}(t) = \frac{u_A(t)}{t_E}\left[\frac{u_A(t)}{2t_E} + \sin\Psi(\mathrm{t})\right] \quad \textbf{Equation 4.6}$$

Combining Equation 4.4 (c) with Equation 4.5 (b) and (c) results in $\varepsilon_{x_1x_2}$ given by

$$\varepsilon_{x_1x_2}(t) = \frac{u_A(t)}{2t_E}\cos\Psi(\mathrm{t}) \quad \textbf{Equation 4.7}$$

where Ψ is a dilatancy angle of the shear band defined as

$$\Psi\,(\mathrm{t}) = \theta_B - \Psi^*\,(\mathrm{t}) \quad \textbf{Equation 4.8}$$

where Ψ^* (t) is the angle given by

$$\Psi^*(t) = \arctan\frac{u_2(t)}{u_1(t)} \qquad \textbf{Equation 4.9}$$

and θ_B is the measured shear band inclination angle, as provided in Table 4.7. Figure 4.35 and Figure 4.36 depict shear and volumetric strains of shear bands for Tests #3, #4, and #5. Volumetric strain is given by

$$\varepsilon_{vol} = -\frac{u_A(t)}{t_E}\sin\Psi(t). \qquad \textbf{Equation 4.10}$$

The lines in Figure 4.35 and Figure 4.36 that stop at the axial strain level which corresponds to the minimum vertical force because unrestricted evolution of shear band is inhibited from this point on. Additional plots depict magnitude of vertical force versus axial strain is provided in Appendix C . Maximum and minimum values of vertical forces and corresponding axial strain levels and axial displacement that are shown in Figure C.1 through Figure C.4. Additional summary results of maximum and minimum values of vertical forces corresponding to the axial strain level and axial displacement are listed in Table 4.11.

Table 4.11 Maximum and minimum forces corresponding to axial strain level

Test number	Axial strain	Displacement	Max force	Axial strain	Displacement	Min force
	%	mm	kN	%	mm	kN
Test #1	1.63	2.29	1.35	2.37	3.33	1.29
Test #3	4.13	5.67	1.33	5.88	8.08	1.29
Test #6	3.15	4.36	1.33	4.31	5.98	1.31
Test #4	4.80	6.52	1.74	6.63	9.00	1.65
Test #5	4.97	6.81	1.73	6.52	8.93	1.61

. Figure 4.35 and Figure 4.36 show that large shear strains evolved in shear bands during the evolution stage. As shown in the figure, shear band initiated very close to the top surface of the sample in Test #1, thus impeding the evolution stage. Consequently Test #1 is excluded in Figure

4.35. In Test #3 the shear band developed the largest shear strain, which was equal to approximately 450% at the minimum vertical force due to small initial shear band thickness (Table 4.7). Saada et al. [21] and Lupini et al. [34] found that the shear band in heavily overconsolidated samples was thinner than that in a lightly overconsolidated samples. Shear bands in Tests #4 and #5 also developed large shear strains, but they were smaller than those found in Test #3. The shear band in Test #3 also developed the largest volumetric strain, while shear bands in Tests #4 and #5 developed smaller volumetric strains.

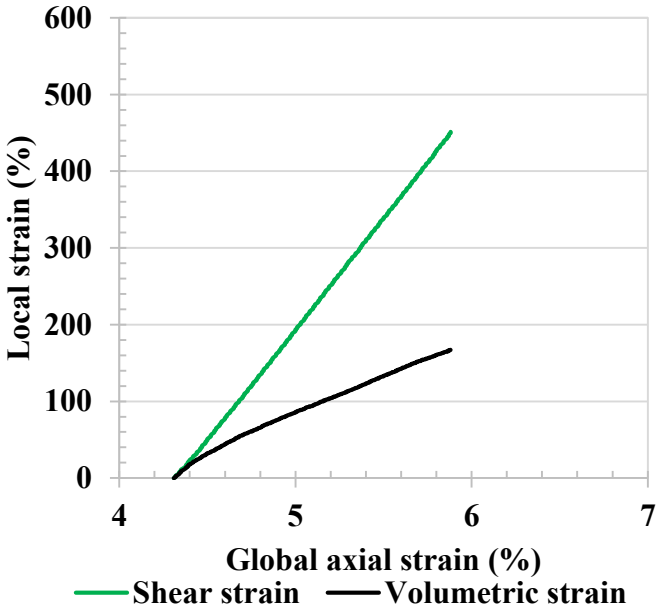

Figure 4.35 Shear and volumetric strain of shear band for Test #3

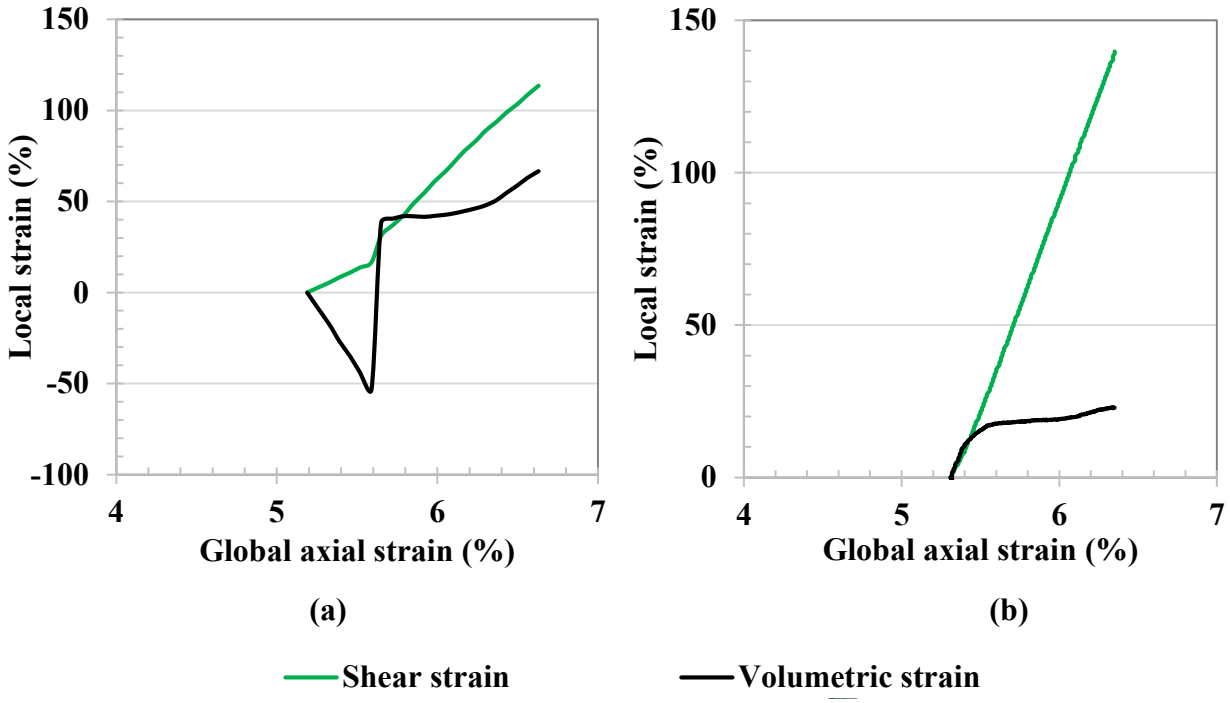

Figure 4.36 Shear and volumetric strain of shear band for (a) Test #4 and (b) Test #5

Figure 4.37 and Figure 4.38 shows a dilatancy angle of the shear band versus global axial strain for Tests #3, #4, and #5. Negative values of dilatancy angles in the figure indicate that shear bands were contractant shear bands. In Test #3 and #5 the shear bands and dilatancy angles ultimately approached steady-state deformation. The dilatancy angle in Test #4, which was the only fast undrained test is shown in Figure 4.38, and it exhibited more erratic behavior.

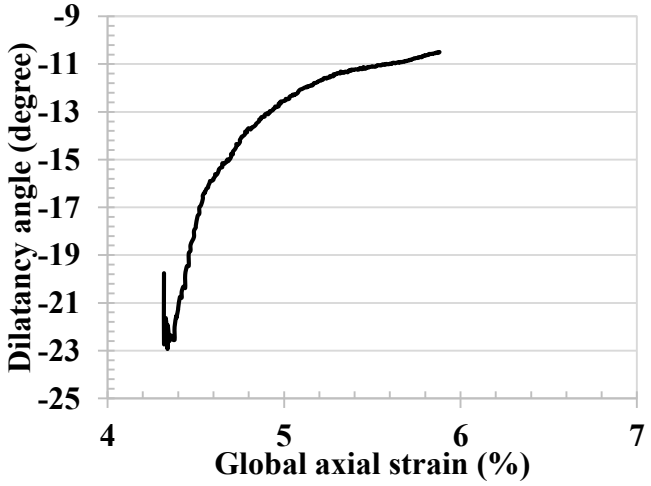

Figure 4.37 Dilatancy angle for Test #3

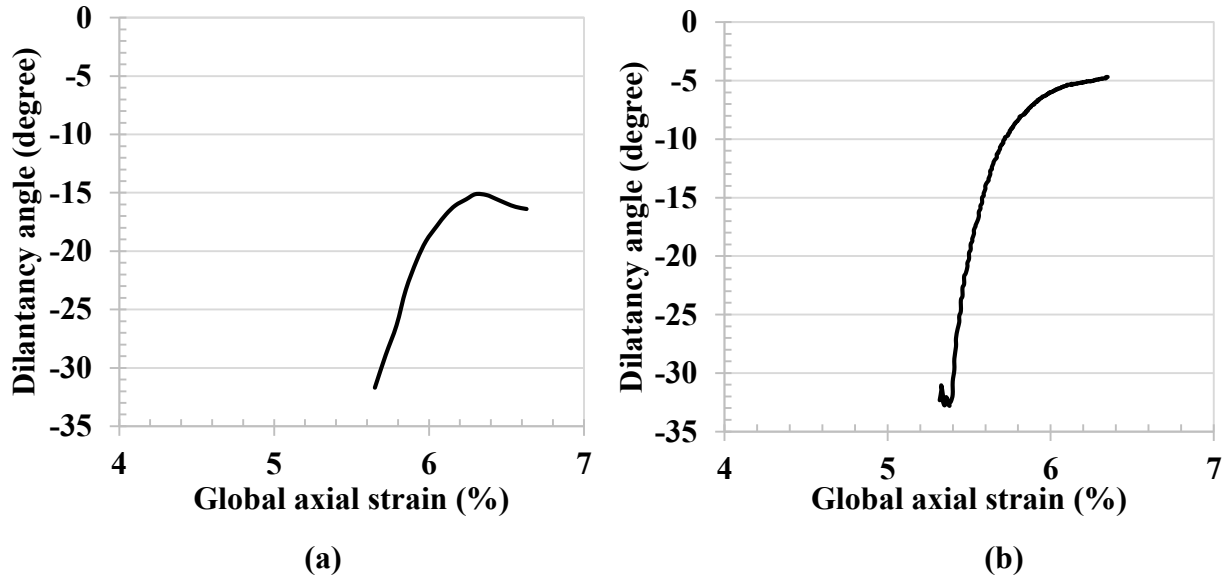

Figure 4.38 Dilatancy angle for (a) Test #4 and (b) Test #5

4.2.6 Eight Events

Figure 4.39 is based on summary results for the eight events presented in Table 4.1. For the lightly overconsolidated samples (Tests #1, #3, and #6), the eight events were grouped into two clusters. The first cluster for Tests #3 and #6 included $O, Max\ q, Max\ q/p'$, $Max\ u_{ave}$, and E; the first cluster corresponded to the propagation stage. These five events followed one another closely, causing the axial strain range corresponding to the first cluster to be 0.75% for Test #3 and 1.19% for Test #6. The second cluster, which included $Min\ u_{ave}$, $Min\ q/p'$, and $Min\ q$, coincided with the evolution stage. The axial strain range corresponding to evolution was equal to 2.07% for Test #3 and 2% for Test #6. The remaining test (Test #1) for heavily overconsolidated samples also revealed two clusters, but the end of propagation belonged to the second cluster. Therefore, an axial strain range of 1.19% corresponded to the propagation stage. The shear band intersected the top surface of the sample shortly after the end of the propagation phase, thereby preventing the evolution phase. In Test #1 the events that belonged to each cluster (propagation and evolution phases) were spaced the closest to one another.

Tests #4 and #5 also exhibited two clusters, but the onset of strain localization in these two tests did not belong to either of the two clusters, indicating slower propagation of the shear band in these tests. Specifically, the axial strain range corresponding to the propagation phase was 2.53% and 1.71% in Tests #4 and #5, respectively. Furthermore, the axial strain range that corresponded to the evolution stage was 3.89% and 2.21% in Tests #4 and #5, respectively.

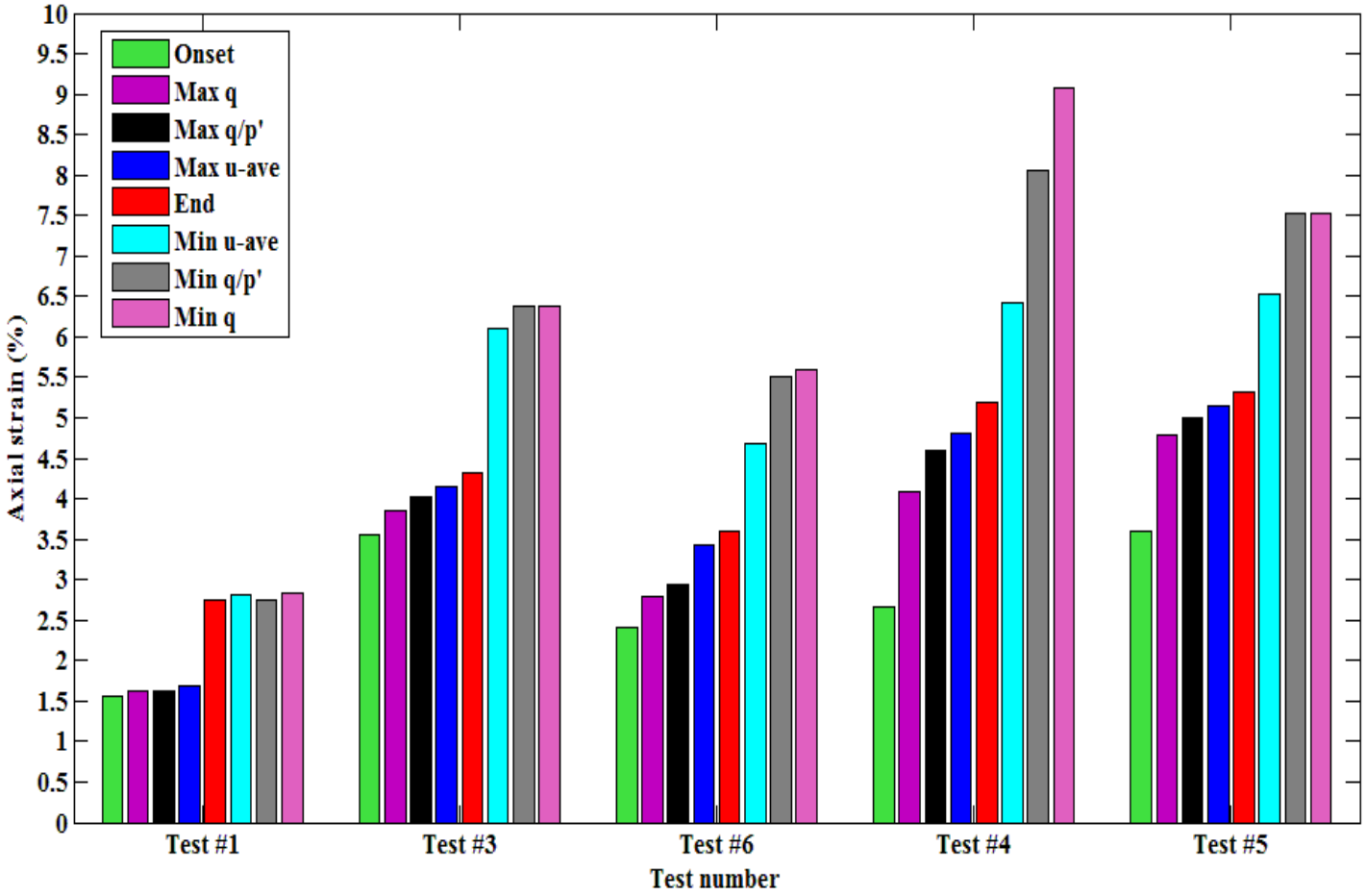

Figure 4.39 Axial strain levels corresponding to the eight events

The propagation and evolution of shear bands were faster in heavily overconsolidated clays than in nearly normally consolidated clays. Furthermore, the faster the loading rate, the faster the shear band propagation. The fastest propagation was observed in Test #1 with 25.48 minutes, and the slowest propagation was observed in Test #5 with 333.51 minutes. The fastest evolution of strain localization was observed in Test #4 (65.02 minutes), and the slowest evolution of strain localization was observed in Test #5 (424.48 minutes). The evolution stage was not available for Test #1 because the corresponding shear band intersected the top platen shortly after the end of propagation.

In summary, the axial strain range corresponding to the propagation and evolution stages was smaller in heavily overconsolidated samples than lightly overconsolidated samples regardless of strain rate, excluding Test #1. Figure 4.40 depicts axial ranges that corresponded to the propagation and evolution stages, and Figure 4.41 shows time ranges corresponding to the propagation and evolution stages. A summary of axial strain and time ranges is provided in Table 4.12.

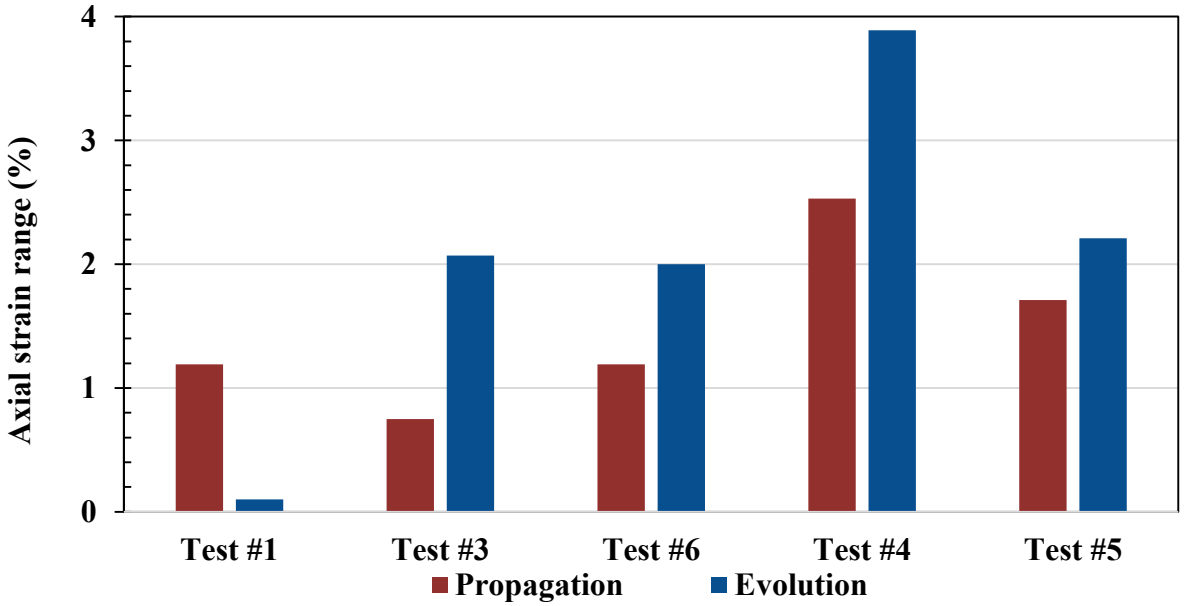

Figure 4.40 Axial strain ranges of propagation and evolution stages

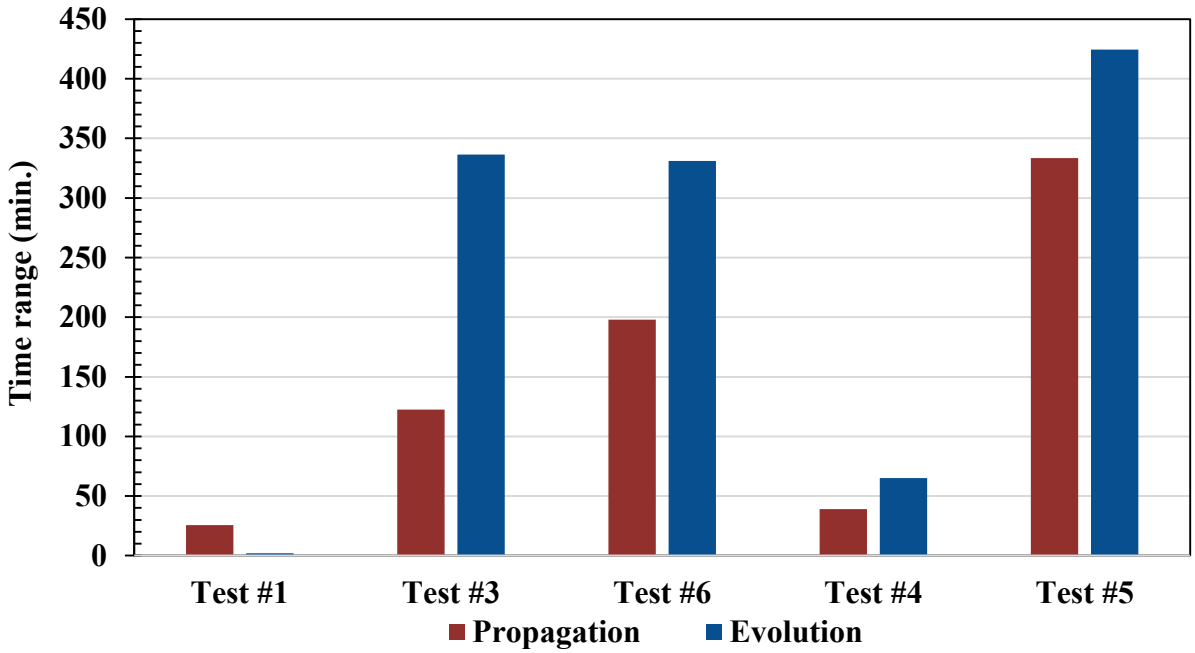

Figure 4.41 Time ranges of propagation and evolution stages

Table 4.12 Axial strain and time ranges for propagation and evolution stages

Test number	Axial strain range (%)		Time range (min.)	
	Propagation	Evolution	Propagation	Evolution
Test #1	1.19	0.10	25.48	2.02
Test #3	0.75	2.07	122.51	336.49
Test #6	1.19	2.00	198.00	330.99
Test #4	2.53	3.89	39.00	65.02
Test #5	1.71	2.21	333.51	424.48

4.2.7 Effective Friction Angle and Cohesion

This study used two methods to trace the evolution of the effective cohesion (c') and effective friction angle ($\emptyset'$). The first method was based on in-plane normal effective and shear stresses acting on the actual failure plane, and the second method was based on overall deviatoric and mean effective stresses. Experimental data from Test #3 and Test #5 only were used because the corresponding strain rates were sufficiently slow.

4.2.7.1 In-plane Normal Effective and Shear Stresses

In-plane normal effective (σ'_α) and shear (τ_a) stresses acting on the shear band were determined from Mohr's circle stresses as

$$\sigma'_a = \frac{\sigma'_y + \sigma'_z}{2} + \frac{\sigma'_y - \sigma'_z}{2}\cos 2\alpha \qquad \textbf{Equation 4.11}$$

$$\tau_a = \frac{\sigma'_y - \sigma'_z}{2}\sin 2\alpha \qquad \textbf{Equation 4.12}$$

where α is a measured shear band inclination angle from horizontal direction, as listed in Table 4.7. The values of α used for these calculations were 50.41° for Test #1 and 52.66° for Test #3. Average inclination angle values were 57.61° and 54.96° for Tests #4 and #5, respectively. A summary of effective normal and shear stresses on shear bands for all tests is provided in Table 4.13 through Table 4.16. Figure 4.42 through Figure 4.49 depict corresponding results associated with the eight events.

Table 4.13 Effective normal and shear stresses for Test #1

Test #1 / Event	ε_a	σ'_y	σ'_z	σ'_α	τ_α	Abs. τ_α
	%	kPa	kPa	kPa	kPa	kPa
O	1.55	36.58	79.11	61.84	-20.89	20.89
Max q	1.63	36.48	79.77	62.19	-21.26	21.26
Max q/p'	1.63	36.48	79.77	62.19	-21.26	21.26
Max u_{ave}	1.69	36.26	79.34	61.85	-21.16	21.16
E	2.74	42.69	60.80	53.45	-8.90	8.90
Min u_{ave}	2.81	42.65	60.75	53.40	-8.89	8.89
Min q/p'	2.74	42.69	60.80	53.45	-8.90	8.90
Min q	2.84	42.62	60.71	53.37	-8.89	8.89

Table 4.14 Effective normal and shear stresses for Test #3

Test #3 / Event	ε_a	σ'_y	σ'_z	σ'_α	τ_α	Abs. τ_α
	%	kPa	kPa	kPa	kPa	kPa
O	3.56	39.26	82.23	66.43	-20.72	20.72
Max q	3.86	38.76	82.90	66.67	-21.29	21.29
Max q/p'	4.03	38.16	82.34	66.09	-21.30	21.30
Max u_{ave}	4.15	38.08	81.38	65.45	-20.88	20.88
E	4.31	38.57	80.01	64.77	-19.99	19.99
Min u_{ave}	6.11	41.98	60.87	53.92	-9.11	9.11
Min q/p'	6.38	42.01	60.09	53.44	-8.71	8.71
Min q	6.38	42.01	60.09	53.44	-8.71	8.71

Table 4.15 Effective normal and shear stresses for Test #4

Test #4 / Event	ε_a	σ'_y	σ'_z	σ'_α	τ_α	Abs. τ_α
	%	kPa	kPa	kPa	kPa	kPa
O	2.66	87.77	162.79	141.26	-33.93	33.93
Max q	4.08	75.72	157.11	133.75	-36.82	36.82
Max q/p'	4.60	72.03	153.74	130.29	-36.96	36.96
Max u_{ave}	4.80	70.63	150.96	127.91	-36.34	36.34
E	5.19	71.35	139.97	120.28	-31.04	31.04
Min u_{ave}	6.43	75.76	115.26	103.92	-17.87	17.87
Min q/p'	8.05	73.73	106.02	96.75	-14.61	14.61
Min q	9.08	71.35	103.27	94.11	-14.44	14.44

Table 4.16 Effective normal and shear stresses for Test #5

Test #5 / Event	ε_a	σ'_y	σ'_z	σ'_α	τ_α	Abs. τ_α
	%	kPa	kPa	kPa	kPa	kPa
O	3.60	77.81	148.26	125.03	-33.12	33.12
Max q	4.79	69.95	146.00	120.93	-35.75	35.75
Max q/p'	4.99	68.90	144.86	119.82	-35.71	35.71
Max u_{ave}	5.15	68.38	141.56	117.44	-34.41	34.41
E	5.31	68.78	134.90	113.10	-31.08	31.08
Min u_{ave}	6.53	75.85	101.48	93.03	-12.05	12.05
Min q/p'	7.52	75.72	99.83	91.88	-11.34	11.34
Min q	7.52	75.72	99.83	91.88	-11.34	11.34

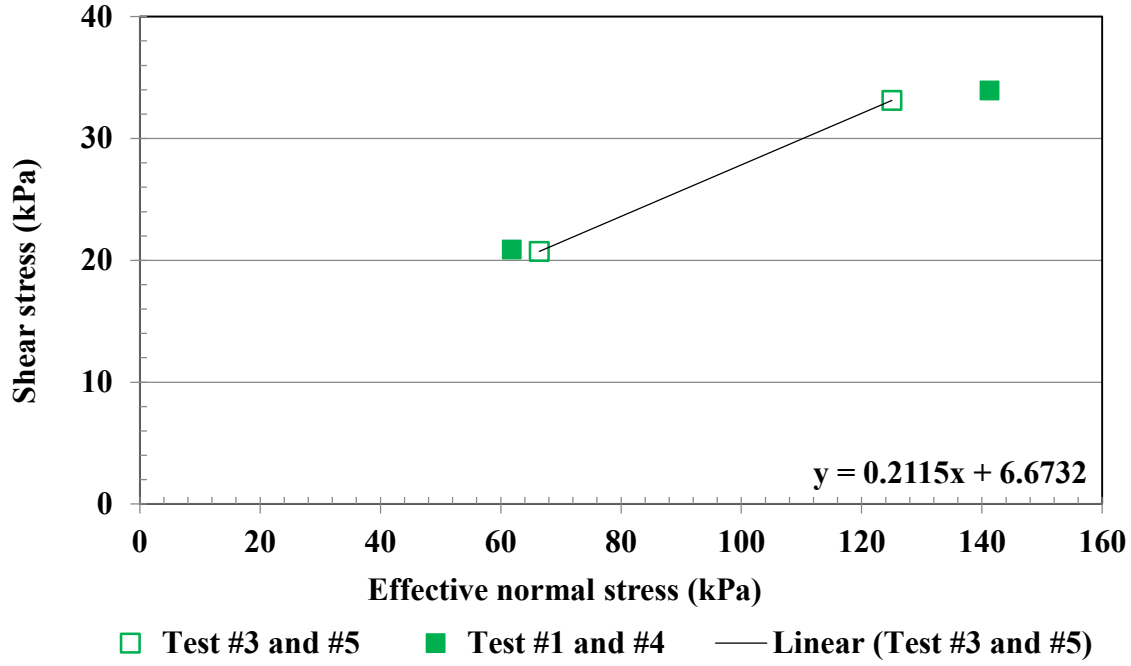

Figure 4.42 Effective normal and shear stresses corresponding to onset

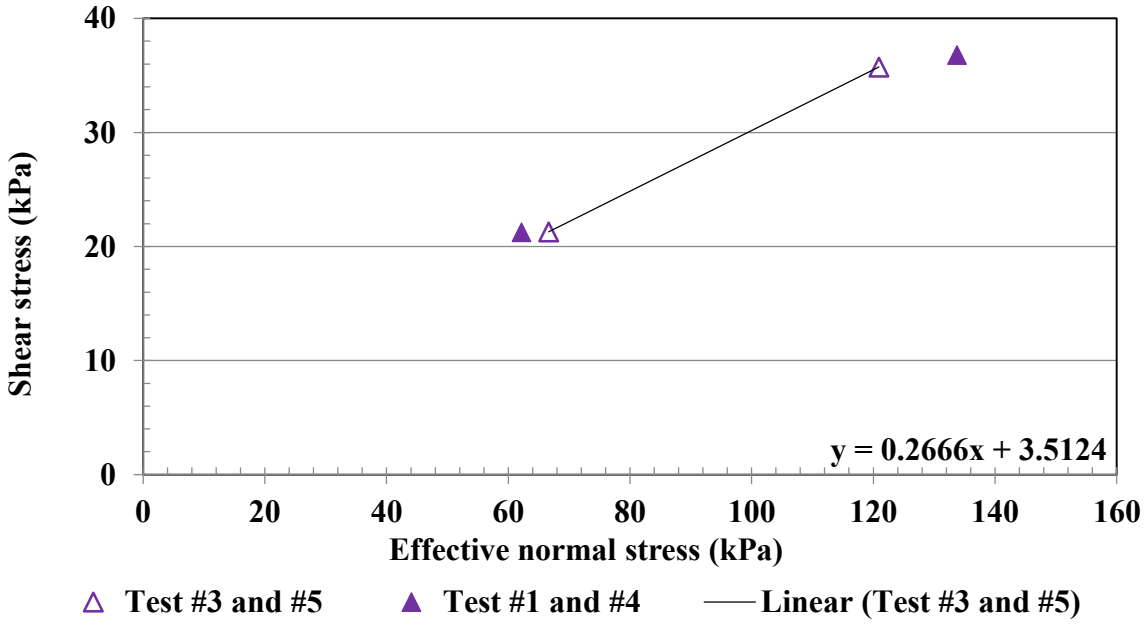

Figure 4.43 Effective normal and shear stresses corresponding to Max q

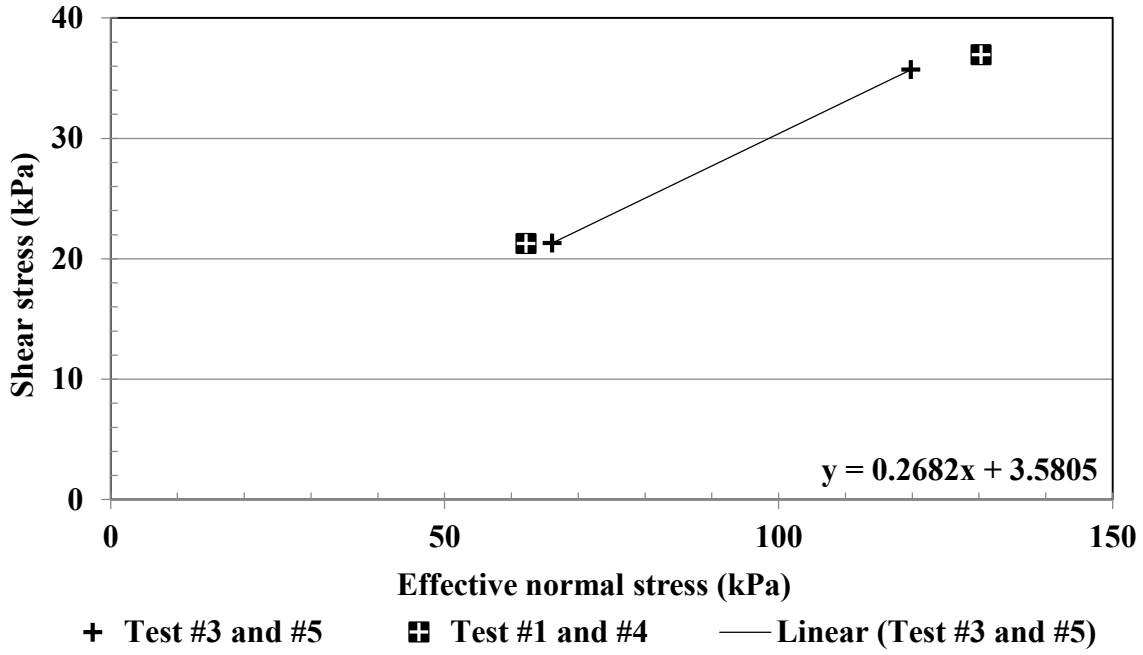

Figure 4.44 Effective normal and shear stresses corresponding to Max q/p'

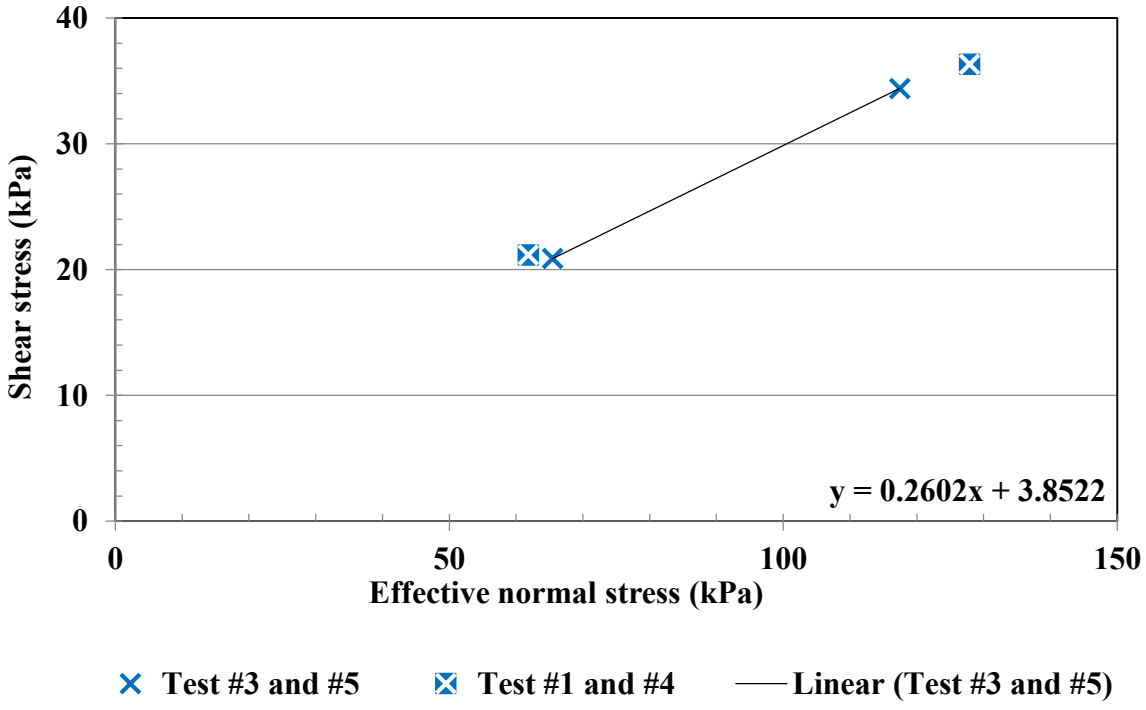

Figure 4.45 Effective normal and shear stresses corresponding to Max u_{ave}

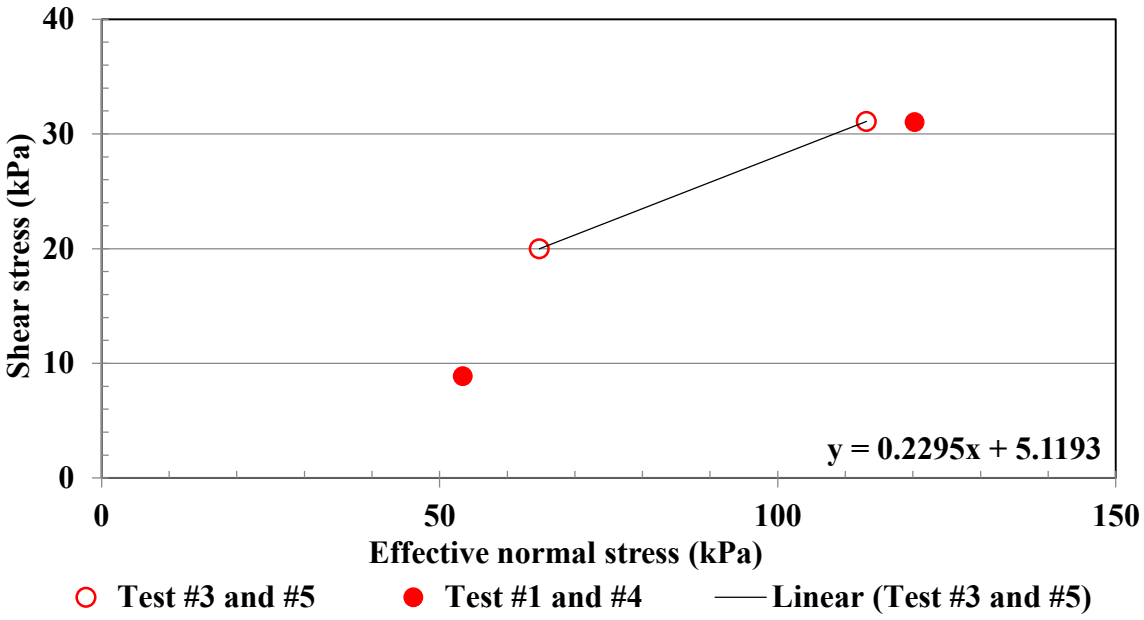

Figure 4.46 Effective normal and shear stresses corresponding to End

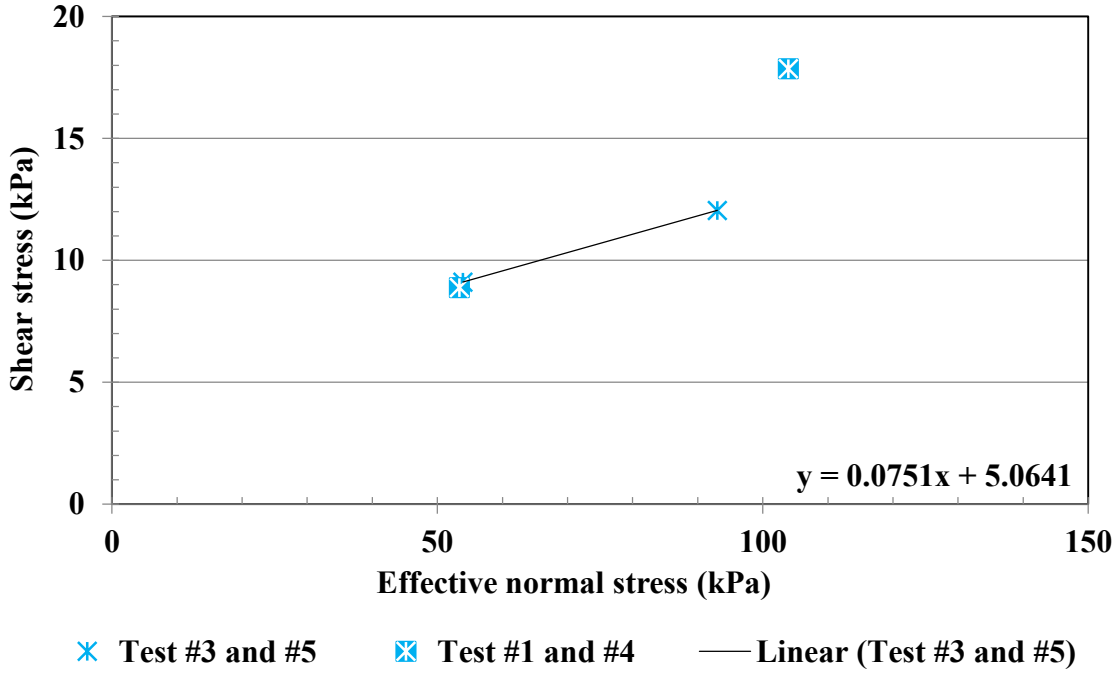

Figure 4.47 Effective normal and shear stresses corresponding to Min u_{ave}

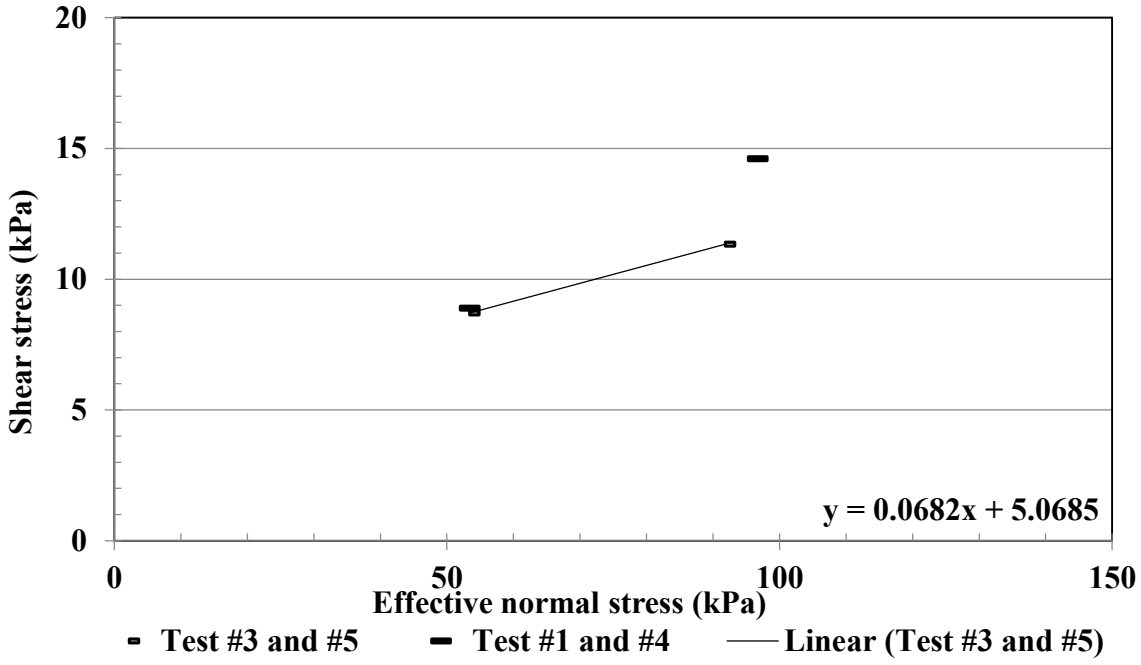

Figure 4.48 Effective normal and shear stresses corresponding to the Min q/p'

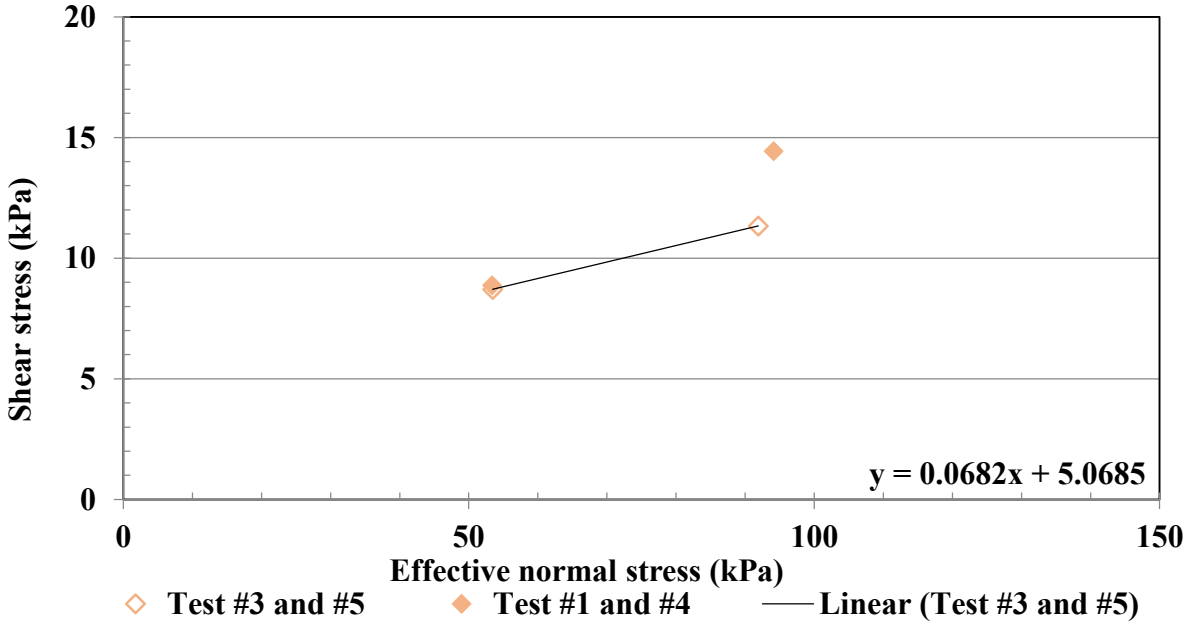

Figure 4.49 Effective normal and shear stresses corresponding to the Min q

The effective cohesion and friction angles of kaolin clays were determined based on Figure 4.42 through Figure 4.49. A summary of effective cohesion and friction from Tests #3 and #5 are listed in Table 4.17 and illustrated in Figure 4.50, in which the last three events each contain two columns reflecting two cross-sectional areas used for stress calculation. The data in the first

column were based on the average area of the entire specimen, while the data in the second column were based on the actual area of the bottom part of specimen.

Table 4.17 Effective cohesion and friction angle of Georgia kaolin

Test #3 and #5 / Events	c'	Ø'
	kPa	Degree
Onset	6.673	11.942
Max q	3.512	14.928
Max q/p'	3.581	15.013
Max u_{ave}	3.852	14.585
End	5.119	12.926
Min u_{ave}	5.064	4.295
Min q	5.069	3.902
Min q/p'	5.069	3.902

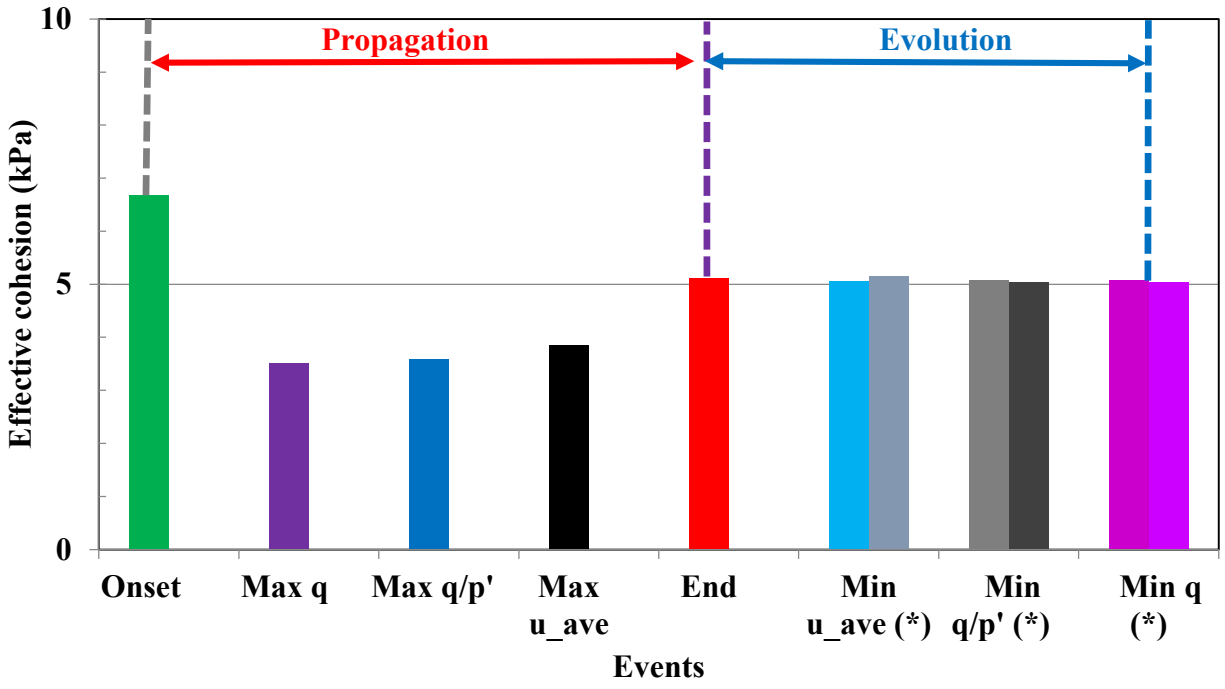

(a)

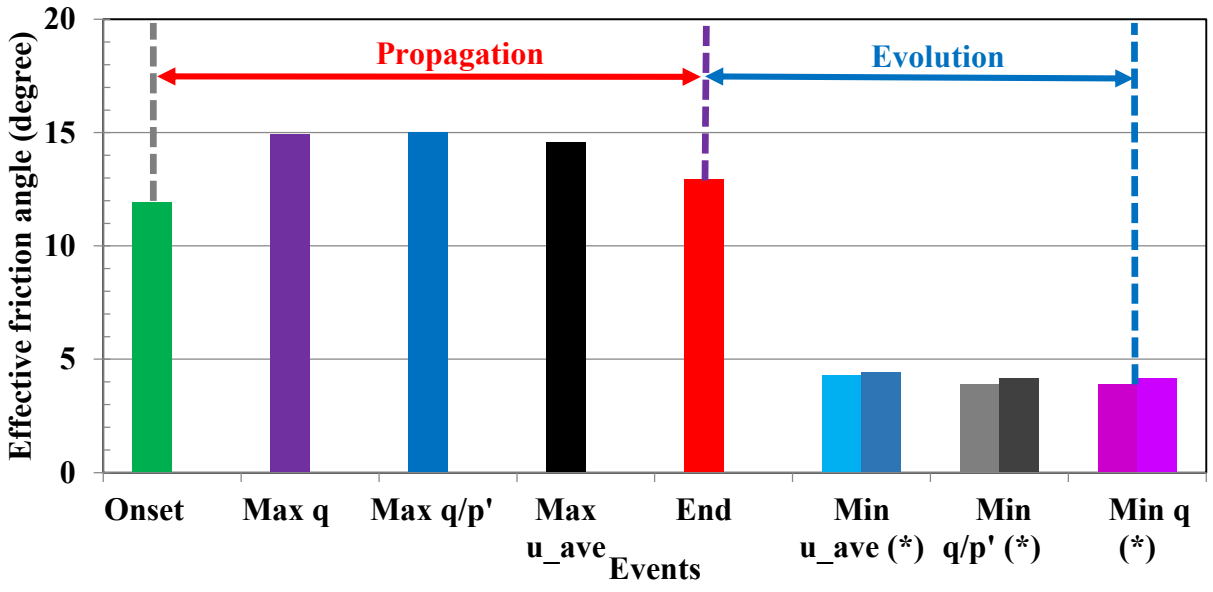

(b)

Figure 4.50 (a) Effective cohesion and (b) friction angle (Tests #3 and #5)

Additional effective friction angles for Test #3 and Test #5 were computed with the assumption that the effective cohesion was zero during the evolution stage. Results are shown in Figure 4.51, whereby three values of effective friction are depicted throughout the evolution phase.

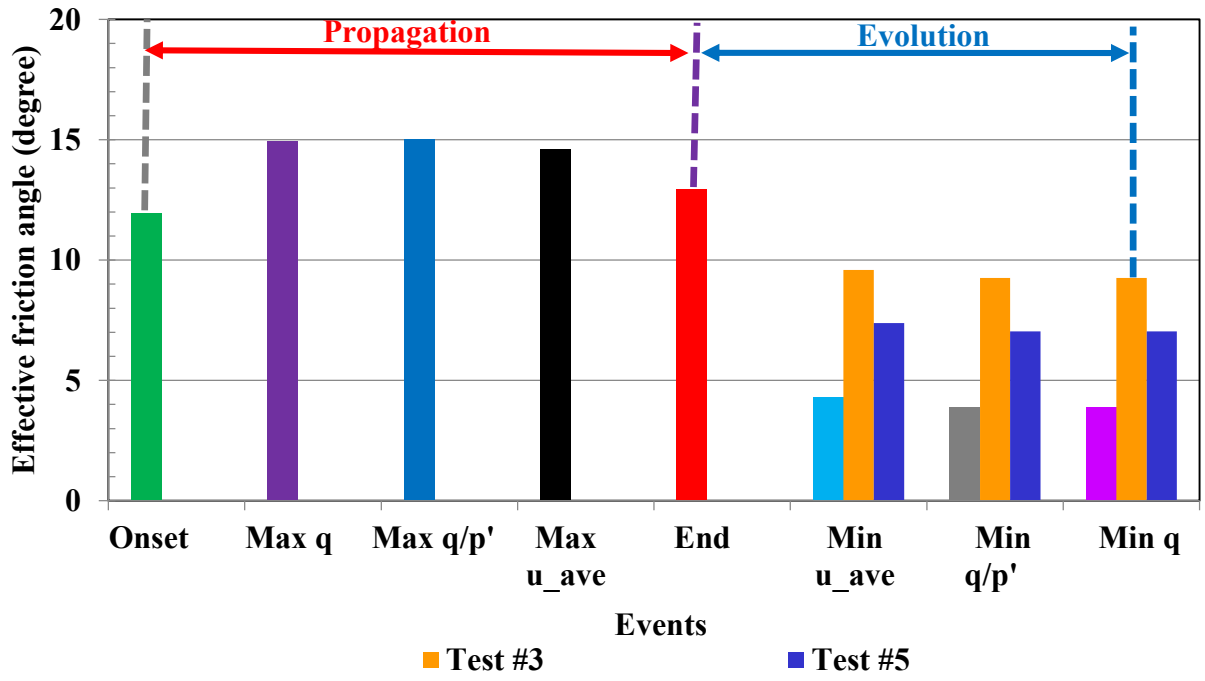

Figure 4.51 Effective friction angle (Tests #3 and #5)

4.2.7.2 Overall Deviatoric and Mean Effective Stresses

Based on load cells measurements, the deviatoric (q) and mean effective stresses (p') and Lode's angle (θ) were calculated and summarized, as described in Section 4.2.1 Compression and Shear Behaviors. Effective cohesion (c') and internal friction angle ($\emptyset'$) were determined by solving a set of simultaneous equations based on results of Tests #3 and #5:

$$q = \frac{3\sin\emptyset'}{\sqrt{3}\cos\theta - \sin\theta\sin\emptyset'}p' + c'\frac{3\cos\emptyset'}{\sqrt{3}\cos\emptyset' - \sin\theta\sin\emptyset'} \qquad \textbf{Equation 4.13}$$

Resulting values of effective friction and cohesion associated with the eight events are listed in Table 4.18, and the propagation and evolution phases are illustrated in Figure 4.52.

Table 4.18 Effective cohesion and friction angle of Georgia kaolin

Test #3 and #5 / Events	c'	$\emptyset'$
	kPa	Degree
Onset	4.31	16.53
Max q	1.40	19.94
Max q/p'	1.39	20.11
Max u_{ave}	1.39	20.11
End	3.03	17.51
Min u_{ave}	4.86	5.22
Min q	4.84	4.73
Min q/p'	4.84	4.73

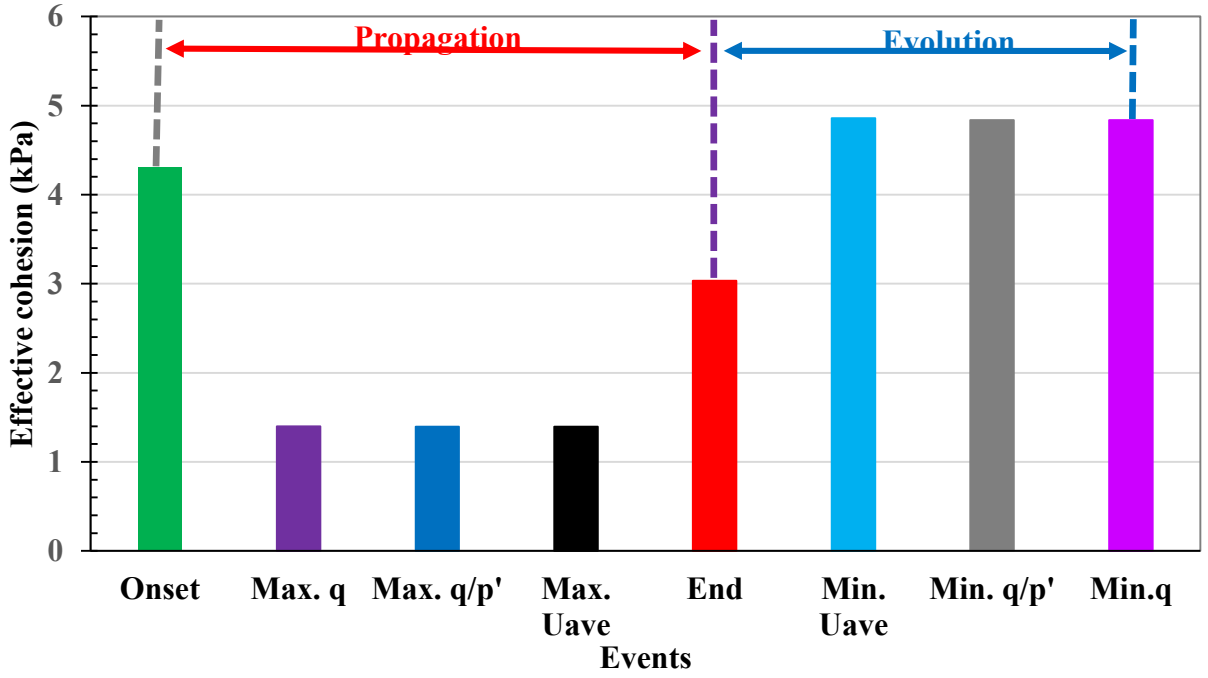

(a)

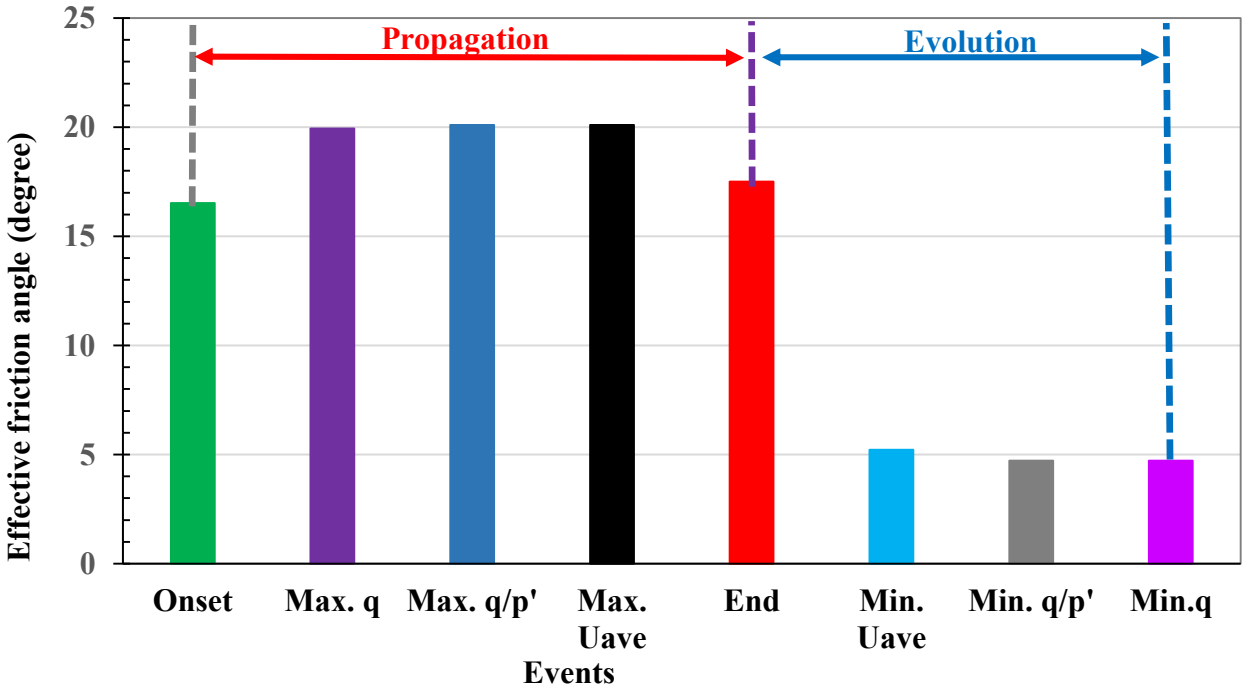

(b)

Figure 4.52 (a) Effective cohesion and (b) friction angle of Georgia kaolin

Although trends indicating evolution of effective cohesion and friction observed from Figure 4.50 and Figure 4.52 were qualitatively similar, they differed quantitatively. Effective cohesion initially decreased during the propagation stage, but effective friction increased. They both stayed approximately constant during the remaining part of the propagation stage. A significant decrease in effective friction occurred during the evolution stage. while effective cohesion remained approximately constant. If effective cohesion during the evolution stage was assumed to be zero, effective friction angles became slightly larger. A significant decrease in the soil friction encountered during the evolution stage is attributed to large shear and volumetric strains at the shear band level (Figure 4.36).

Hicher and Wahyudi [35] used SEM and transmission electron microscope (TEM) to observe orientation of clay particles in the shear zone of CT samples. They found that zones of strain localization were subjected to large distortion and volume change. They also observed a significant evolution of clay structure inside shear bands in the form of strong reorientation of clay particles, which created a significant anisotropy. Sengupta [22] found that degree of magnetic anisotropy, which is a gauge for strain intensity, was larger for clay cores taken from shear bands of biaxial clay samples than for those taken from outside of shear bands. Hicher and Wahyudi [35] and Sengupta [22] confirmed results obtained in the current study, particularly that the main particle scale mechanism that leads to large shear and volumetric strains at the mesoscale is reorientation of clay particles. Thus, the reorientation of clay particles is most likely responsible for a significant decrease in internal friction angle, resulting in ultimate values being significantly smaller than the critical state angle. The critical state effective friction angle of a similar kaolin clay was 20.1° [28].

Chapter 5 - Conclusions and Recommendations

5.1 Conclusions

The plane strain experimental program explored the effects of strain rate and stress history on strain localization behavior in clay. Five undrained plane strain tests were performed on slurry consolidated Georgia kaolin samples, resulting in the following conclusions:

1. Force displacement and stress-strain responses of all samples exhibited a pronounced peak that was followed by a severe post-peak drop.
2. Strain localization in the form of contractant shear bands was observed in most tests.
3. Internal displacement measurements showed that each sample's response consisted of three phases: (1) a homogenous deformation, (2) onset of strain localization and propagation of shear band, and (3) shear band evolution.
4. In all tests a homogenous deformation phase terminated before maximum vertical force was reached. Furthermore, the propagation stage was complete before minimum vertical force was reached.
5. Lagrange strain tensor was used to compute shear and volumetric strains at the level of shear bands during the evolution stage in Tests #3, #4, and #5 using internal displacement measurements. A simple shear mode of deformation was assumed.
6. The evolutions of effective cohesion and effective friction angle were traced from the onset of strain localization to the end of the evolution phase. Unlike in granular materials, ultimate effective friction angle values were significantly lower than critical state values.

7. Based on independent evidence obtained by Hicher and Wahyudi [35] and Sengupta [22], the sub-mesoscale mechanism responsible for large shear and volumetric strains is significant reorientation of clay particles.
8. The important implication for engineering practice is that effective friction can be significantly reduced in the presence of well-developed shear band.

5.2 Recommendations

The following recommendations are suggested for further research related to strain localization in clays:

- More experimental data from plane strain tests, including drained and undrained tests, on various types of clays should be generated.
- It would be advantageous to develop experimental methods for local measurements of PWPs if they did not interfere with the strain localization process.
- A dynamic plane strain tests on clays should be performed to provide experimental data for dynamic strain localization in order to elucidate the behavior of earthquake-induced landslides.
- Additional sub-mesoscale information is also needed for clays. This information could be obtained by combining destructive methods, such as SEM, TEM, and AMS, and nondestructive methods, such as X-ray tomography.

References

[1] K. L. Lee, "Comarison of plane strain and triaxial tests on sand," *Journal of Soil Mech Foundation,* vol. 96, no. 3, p. 901–923, 1970.

[2] H. B. Mühlhaus and I. Vardoulakis, "The thickness of shear bands," *Géotechnique,* vol. 3, no. 37, p. 271–283, 1987.

[3] J. Peters, P. V. Lade and A. Bro, "Shear band fomation in triaxial and plane strain test," in *Advanced Triaxial Testing of Soil and Rock, ASTM STP 977*, Eds., Philadelphia: American Society for Testing and Materials, 1988, p. 640–627.

[4] A. Drescher, I. Vardoulakis and C. Han, "A biaxial apparatus for testing soils," *Geotechnical Testing Journal,* vol. 13, no. 3, p. 226–234, 1990.

[5] C. Han and I. G. Vardoulakis, "Plane-strain compression experiments on water-saturated fine-grained sand," *Géotechnique,* vol. 41, no. 1, p. 49–78, 1991.

[6] C. Han and A. Drescher, "Shear bands in biaxial tests on dry coarse sand," *Soils and Foundations,* vol. 33, no. 1, p. 118–132, 1993.

[7] R. J. Finno, W. W. Harris, M. A. Mooney and G. Viggiani, "Shear bands in plane strain compression of loose sand," *Géotechnique,* vol. 47, no. 1, p. 149–165, 1997.

[8] A. S. Saada, L. Liang, J. L. Figueroa and C. T. Cope, "Bifurcation and shear band propagation in sands," *Géotechnique,* vol. 49, no. 3, p. 365–385, 1999.

[9] K. A. Alshibli and S. Sture, "Shear band formation in plane strain experiments of sands," *Journal of Geotechnical and Geoenvironmental Engineering,* vol. 126, no. 6, p. 495–503, 2000.

[10] A. L. Rechenmacher, "Grain-scale processes governing shear band initiation and evolution in sands," *Journal of the Mechanics and Physics of Solids,* vol. 54, no. 1, p. 22–45, 2006.

[11] L. Zhuang, Y. Nakata and I. M. Lee, "Localized deformation in sands and glass beads subjected to plane strain compressions," *Geomechanics and Engineering,* vol. 5, no. 6, p. 499–517, 2013.

[12] R. Finno and Y. Rhee, "Consolidation, pre- and post-peak data from internally instrumented plane strain," *Geotechnical Testing Journal,* vol. 4, no. 16, p. 496–509, 1993.

[13] D. Perić, K. Runesson and S. Sture, "Shear band formation in triaxial and plane strain test," *Journal of Engineering Mechanics,* vol. 3, no. 118, p. 514–524, 1992.

[14] K. A. Alshibli and I. S. Akbas, "Strain localization in clay: plane strain versus triaxial loading conditions," *Geotechnical and Geological Engineering,* no. 25, p. 45–55, 2007.

[15] G. Viggiani, R. J. Finno and W. W. Harris, "Experimental observations of strain localization in plane strain compression of a stiff clay," in *Localization and Bifucation Theory for Soils and Rocks*, Eds., CRC Press, 1994, p. 189–198.

[16] A. Sengupta, "Strain localization in geomaterials in nature, laboratory tests and numerical analyses," *Current science,* vol. 98, no. 9, p. 141–163, 2010.

[17] J. S. Tchanlenko and N. R. Morgenstern, "Microscopic structures in kaolin subjected to direct shear," *Géotechnique,* no. 17, p. 309–328, 1967.

[18] A. S. Gylland, H. Rueslatten, H. P. Jostad and S. Nordal, "Microstructural observations of shear zones in sensitive clay," *Engineering Geology,* vol. 163, p. 75–88, 2013.

[19] A. S. Gylland, H. P. Jostad and S. Nordal, "Experimental study of strain localization in sensitive clays," *Acta Geotechnica,* vol. 9, p. 227–240, 2014.

[20] P. Anantanasakul, J. A. Yamamuro and P. V. Lade, "Three-dimensional drained behavior of normally consolidated anisotropic kaolin clay," *Soils and Foundation,* vol. 1, no. 52, p. 146–159, 2012.

[21] A. S. Saada, G. F. Bianchini and L. Liang, "Cracks,bifurcation and shear bands propagtaion in saturated clays," *Géotechnique,* vol. 44, no. 1, p. 35–64, 1994.

[22] A. Sengupta, "Anisotropy of magnetic susceptibility study of kaolinite matrix subjected to biaxial tests," *Clays and Clay Minerals,* vol. 57, no. 2, p. 251–263, 2009.

[23] I. Vardoulaksi and M. Goldsheider, "Biaxial apparatus for testing shear bands in soils," in *Tenth Internation Coference on Soil Mechanics and Foundation Engineering*, Stockholm, 1981.

[24] N. Marachi, J. M. Duncan, C. K. Chan and H. B. Seed, "Plane-strain testing of sand," in *Laboratory Shear Strength of Soil, ASTM STP 740*, Eds., Philadelphia: American Society for Testing and Materials, 1981, p. 294–302.

[25] H. W. Wade, "Localizaiton of loss granular soils and its effect on undrained steady state strength," Ph.D. disseration, Dept. Civil. Eng., Northwestern University, Evanston,IL, 1994.

[26] D. Perić, *Private communication,* Manhattan, Kansas: Kansas State University, 2016.

[27] D. Znidarčić, *Private communication,* Boulder, Colorado: University of Colorado, 1998.

[28] D. Perić, "Experimental and numerical modeling of a strip footing on clay," M.S. thesis, Dept. Civil. Enviormental and Architectural Eng., University of Colorado, Boulder,CO, 1988.

[29] J. E. Andrade and R. I. Borja, "Capturing strain localization in dense sands with random density," *International Journal for Numerical Methods in Engineering,* no. 67, p. 1531–1564, 2006.

[30] A. Drescher and I. Vardoulakis, "Geometric softening in the triaxial test on granular material," *Géotechnique,* vol. 32, p. 291–303, 1982.

[31] R. J. Finno, W. W. Harris and G. Viggiani, "Pore pressures and strain localization in stiff clay," in *Fracture and Damage in Quasibrittle Structures*, Prague, E & FN SPON, 1994, p. 441–449.

[32] W. W. Harris, G. Viggiani, M. A. Mooney and R. J. Finno, "Use of stereophotogrammetry to analyze the development of shear bands in sand," *Geotechnical Testing Journal,* vol. 4, no. 18, p. 405–420, 1995.

[33] A. F. Bower, Applied mechanics of solids, Boca Raton, New Jersey: CRC Press, 2010.

[34] J. F. Lupini, A. E. Skinner and P. R. Vaughan, "The drained residual strength of cohesive soils," *Géotechnique,* vol. 2, no. 31, pp. 18 1-213, 1981.

[35] P. Y. Hicher, H. Wahyudi and D. Tessied, "Microstructural analysis of strain localization in clay," *Computers and Geotechnics,* vol. 16, no. 3, p. 205–222, 1994.

[36] P. J. Sabatini and R. Finno, "Effect of consolidation on strain localization," *Computers and Geotechnics,* vol. 4, no. 18, p. 331–339, 1996.

Appendix A - Additional LVDT Displacement Results

The following figures represent all LVDT displacements versus axial strain for each test:

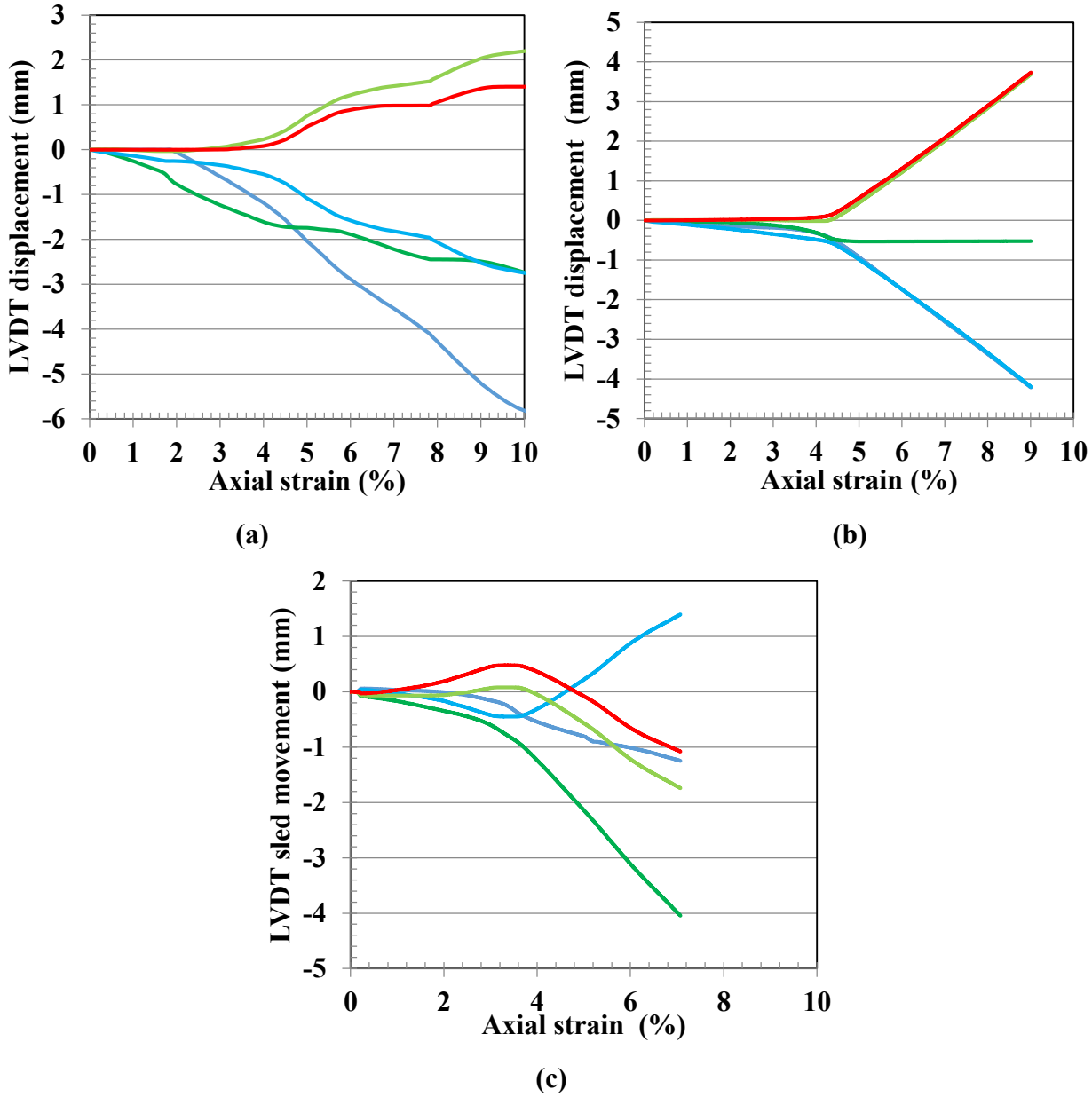

Figure A.1 LVDT displacements for (a) Test #1, (b) Test #3, and (c) Test #6

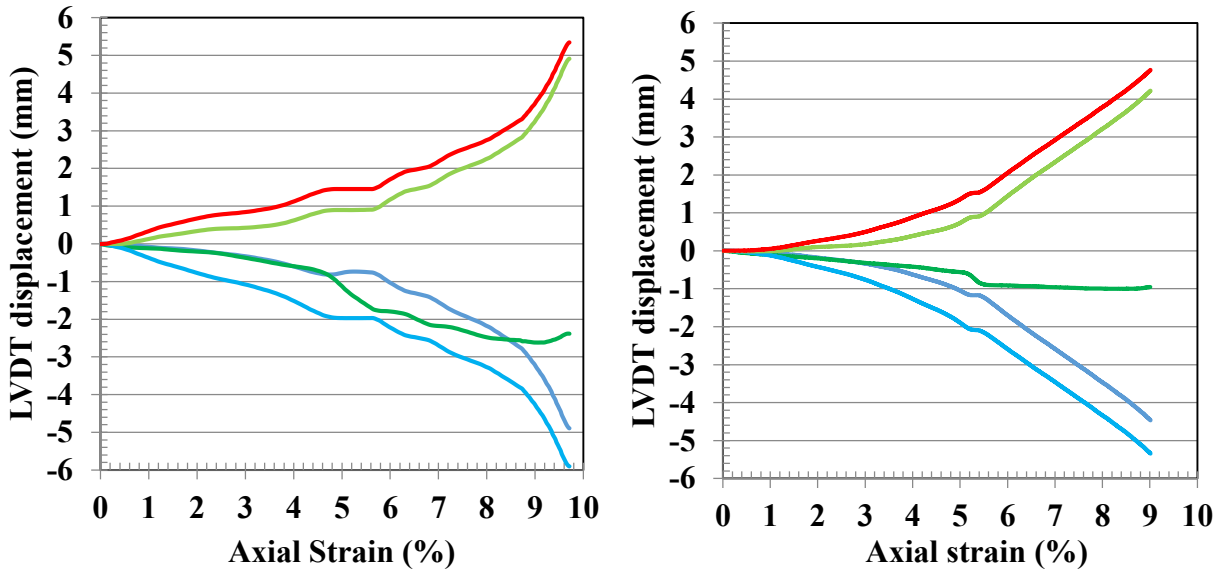

(d) (e)

Figure A.2 LVDT displacements for (d) Test #4 and (e) Test #5

Appendix B - Friction, Tilting, and Eccentricity

The following figures represent (friction, tilting, and eccentricity) and plot their values versus axial strain:

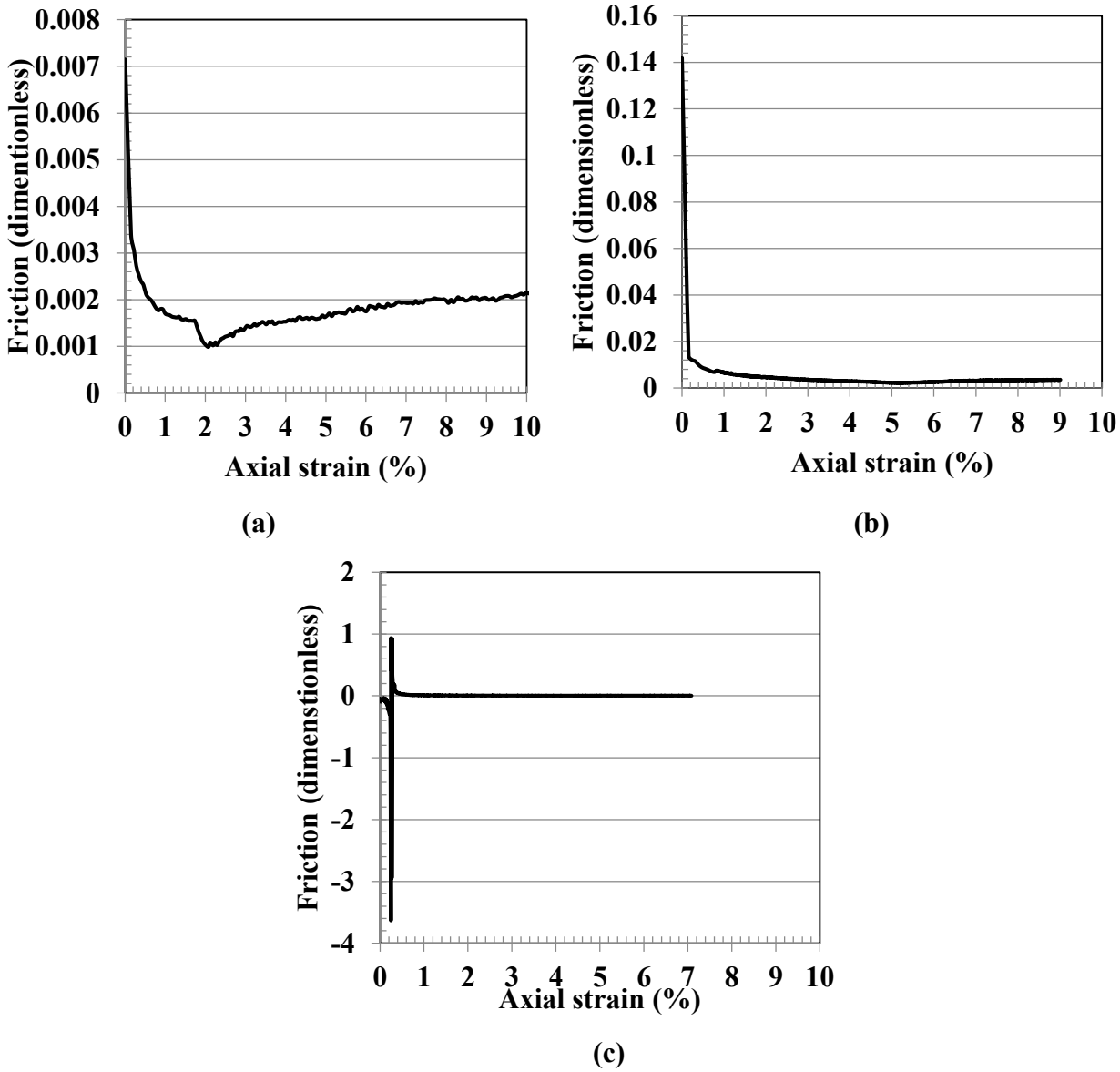

Figure B.1 Friction for (a) Test #1, (b) Test #3, and (c) Test #6

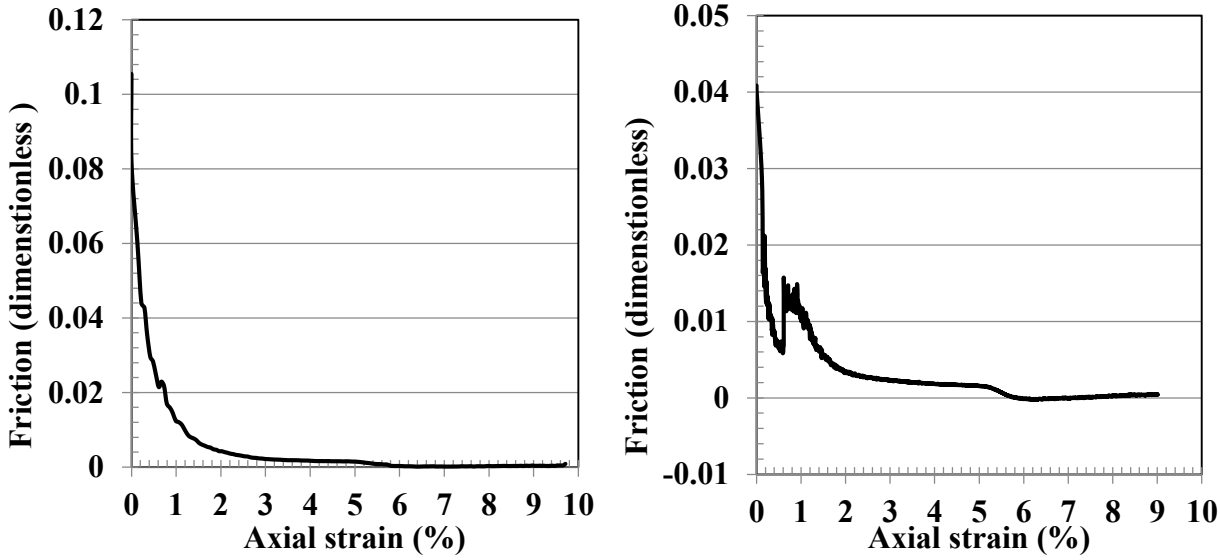

(d) **(e)**

Figure B.2 Friction for (d) Test #4 and (e) Test #5

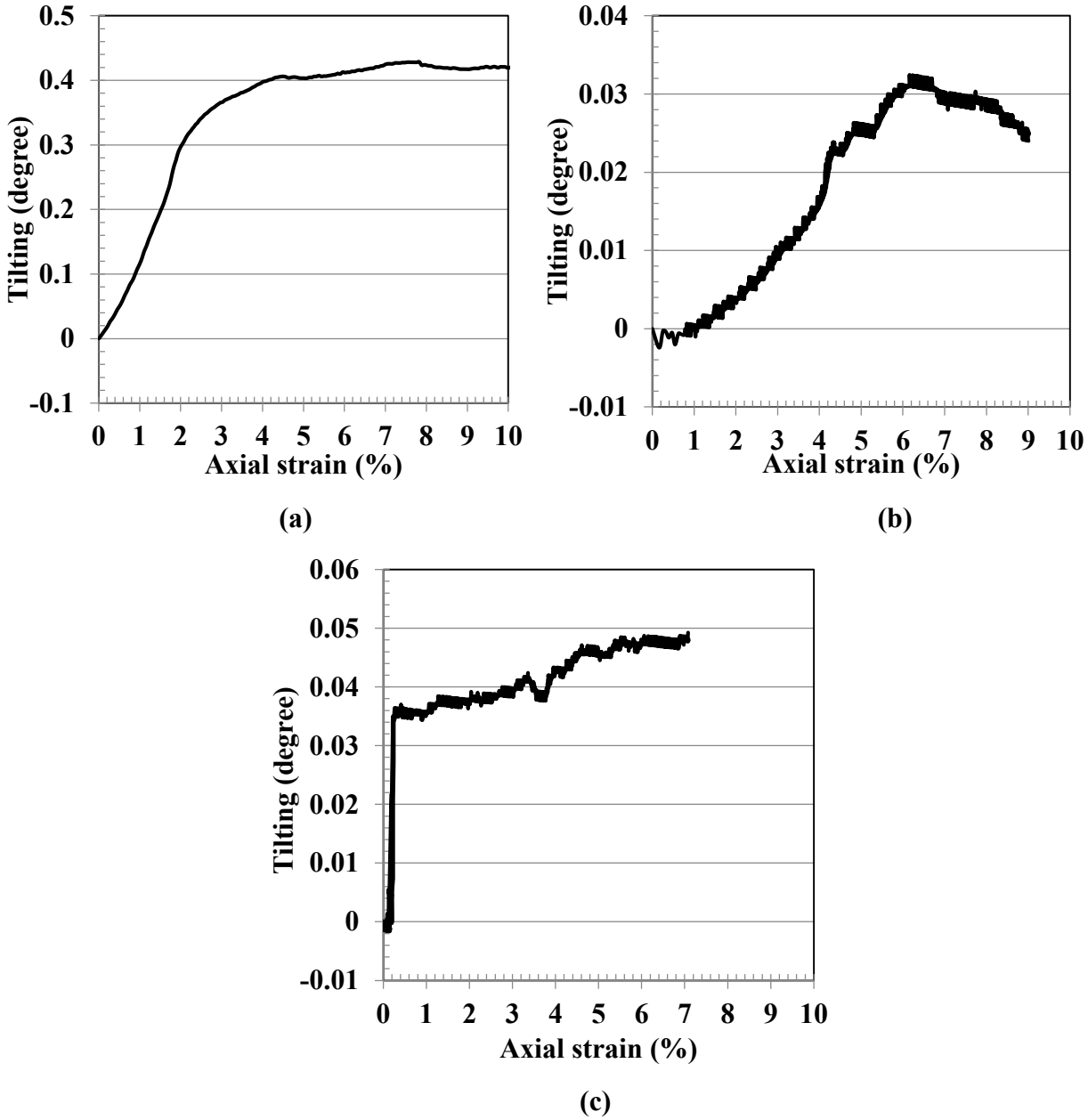

Figure B.3 Tilting for (a) Test #1, (b) Test #3, and (c) Test #6

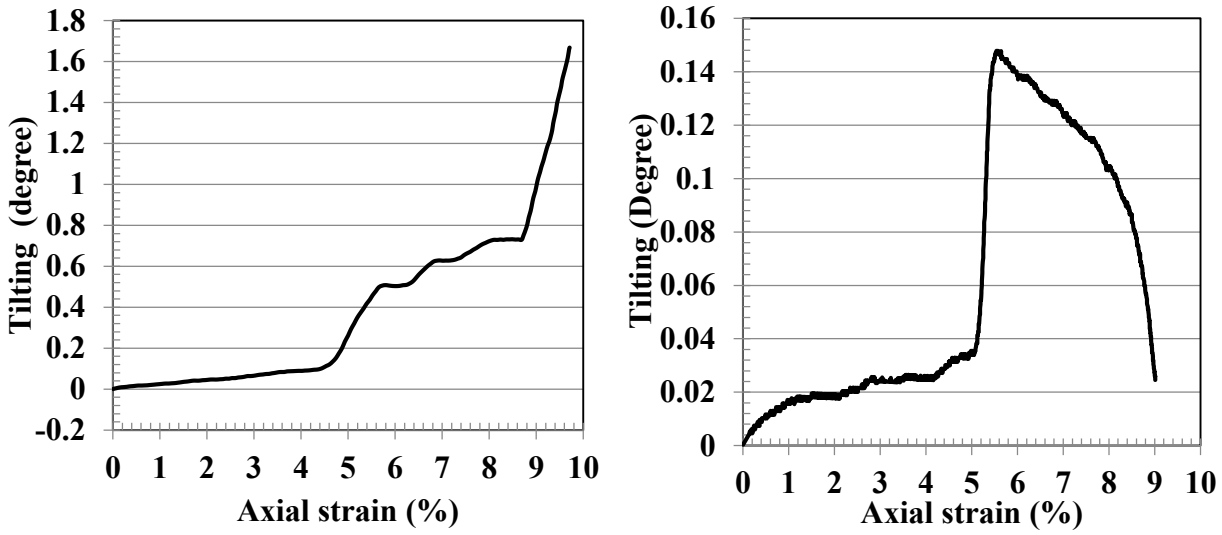

(d) **(e)**

Figure B.4 Tilting for (d) Test #4 and (d) Test #5

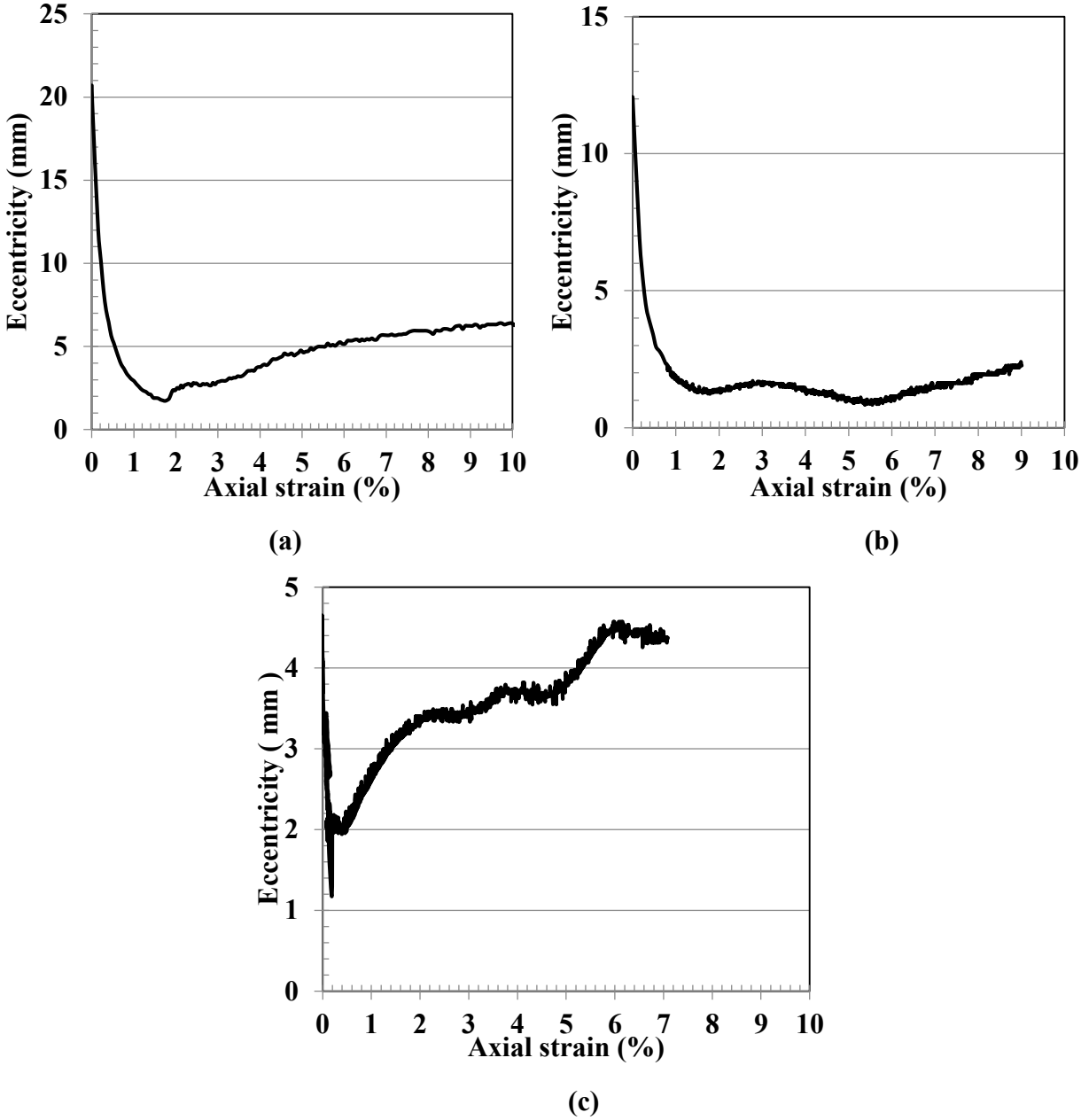

Figure B.5 Eccentricity for (a) Test #1, (b) Test #3, and (c) Test #6

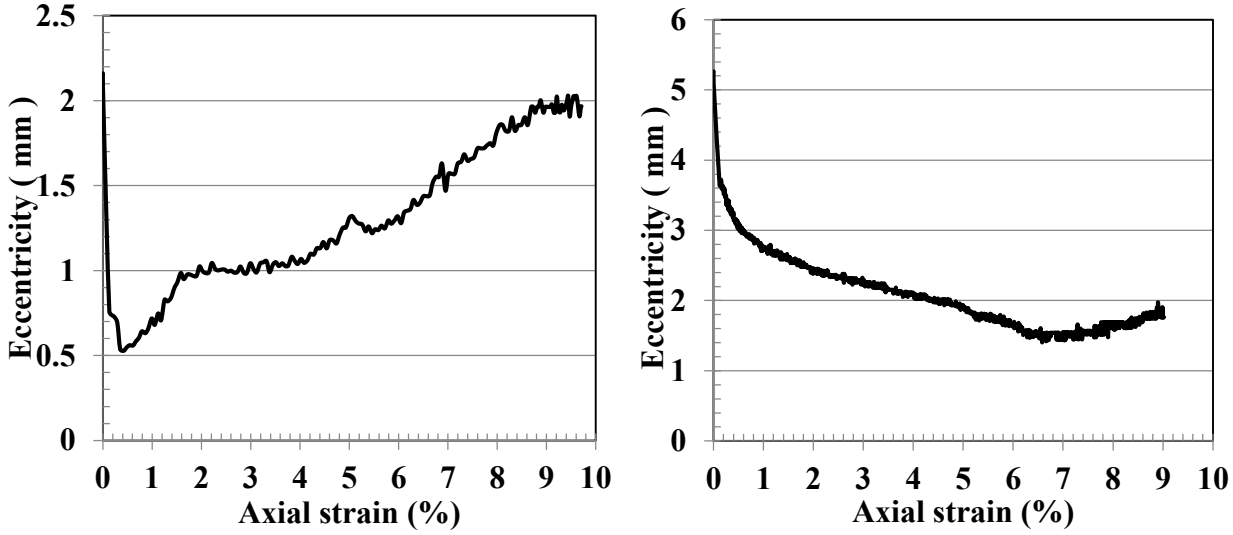

(d) (e)

Figure B.6 Eccentricity for (d) Test #4 and (e) Test # 5

Appendix C – Vertical Force

The following figures represent all experimental measurements, including vertical force and axial (vertical) displacement, vertical force versus axial strain, and vertical displacement:

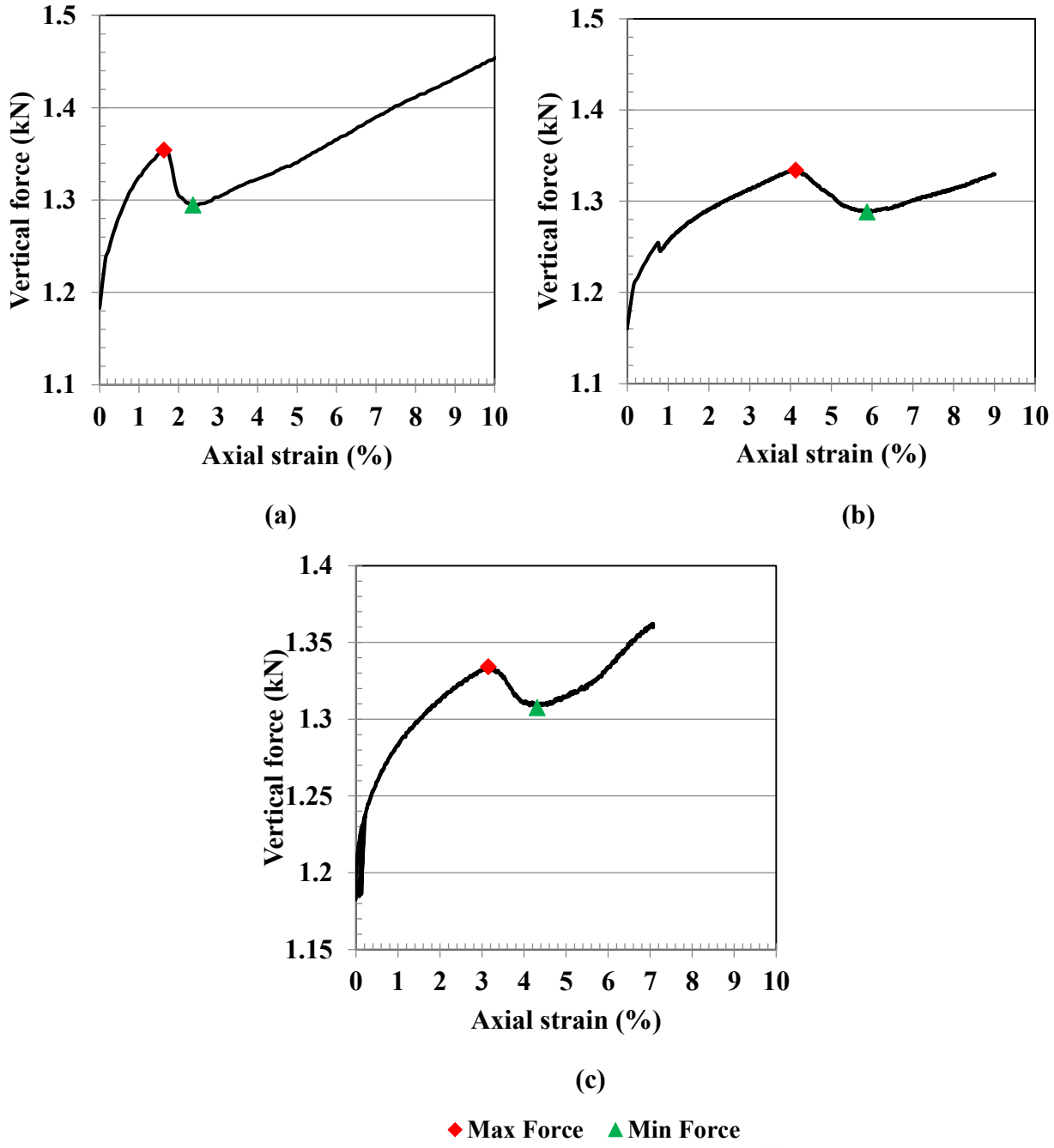

Figure C.1 Vertical force versus axial strain for (a) Test #1, (b) Test #3, and (c) Test #6

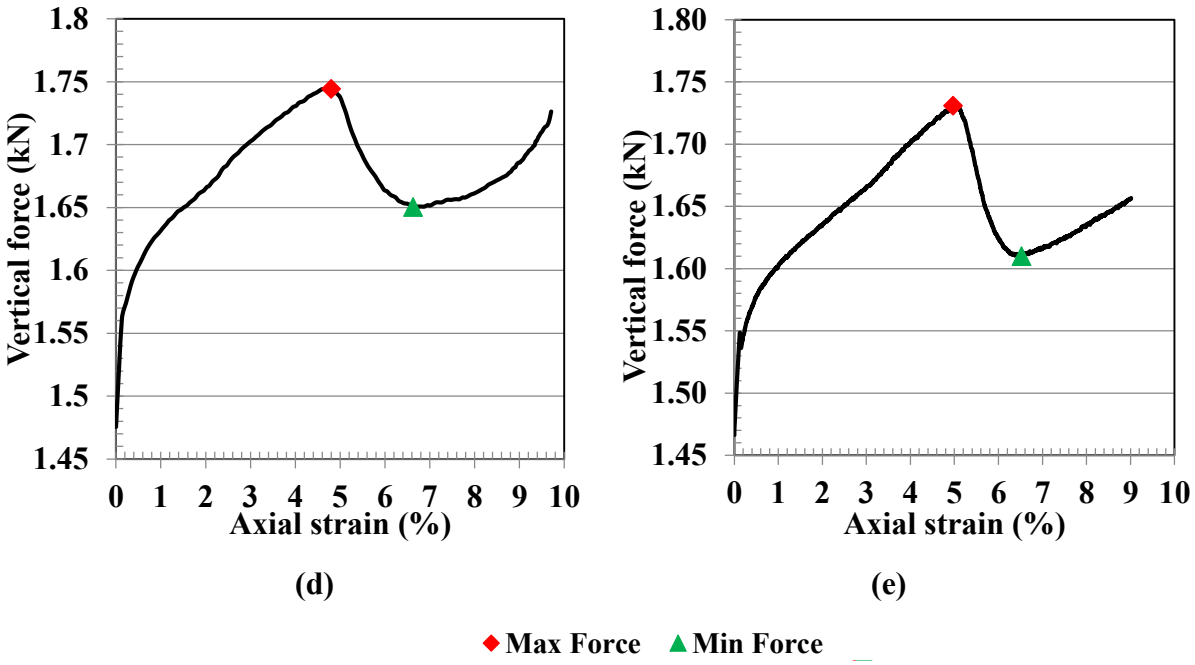

Figure C.2 Vertical force versus axial strain for (d) Test #4 and (e) Test #5

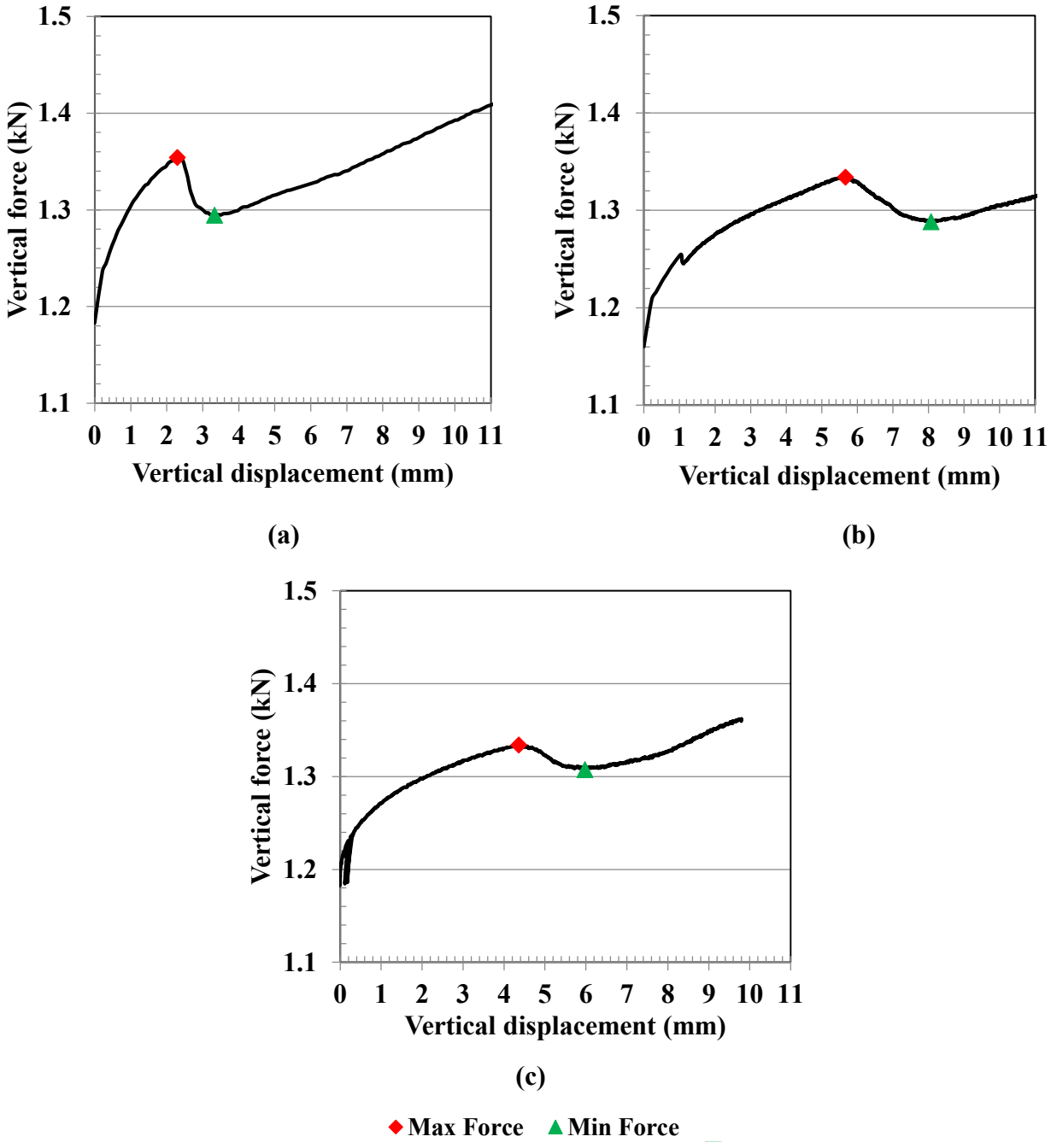

Figure C.3 Vertical force versus vertical displacement for (a) Test #1, (b) Test #3, and (c) Test #6

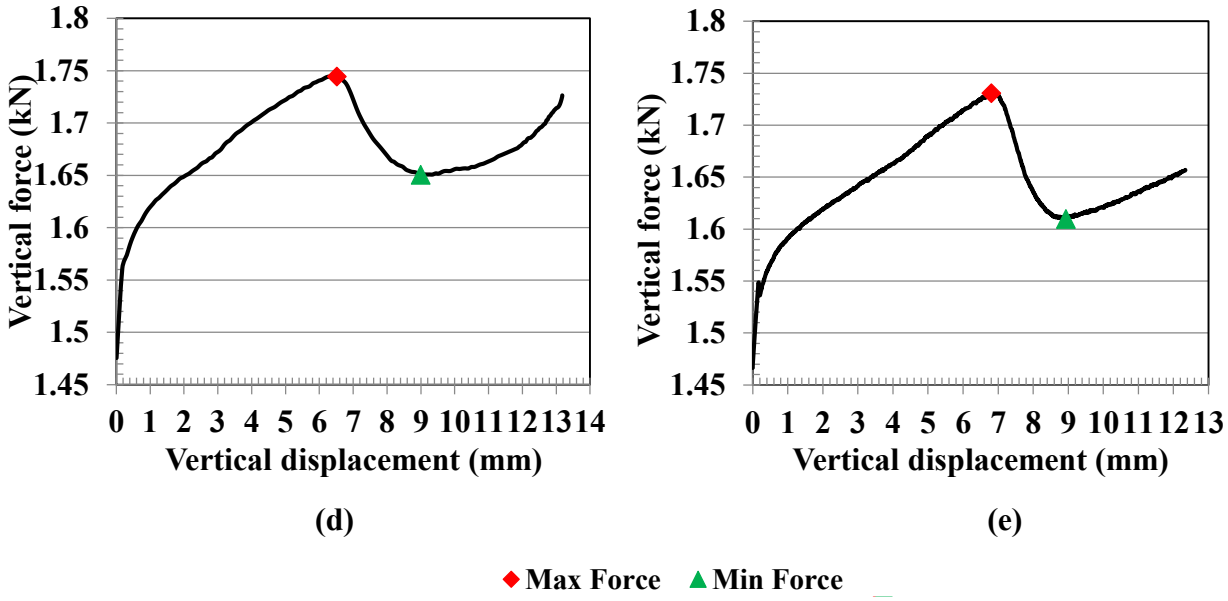

Figure C.4 Vertical force versus vertical displacement for (d) Test #4 and (e) Test #5